Joana Margarida Franco Dantas

Licenciatura em Química Aplicada

Follow the red road of triheme cytochromes in *Geobacter sulfurreducens*

Dissertação para obtenção do Grau de Mestre em
Bioquímica Estrutural e Funcional

Orientador: Prof. Doutor Carlos A. Salgueiro, Professor Auxiliar,
Faculdade de Ciências e Tecnologia, Universidade Nova de Lisboa

Júri
Presidente: Prof. Doutor José Ricardo Ramos Franco Tavares
Arguente: Prof. Doutor Vítor Manuel Bordona de Sousa Paixão

FACULDADE DE
CIÊNCIAS E TECNOLOGIA
UNIVERSIDADE NOVA DE LISBOA

Setembro 2012

Universidade Nova de Lisboa

Joana Margarida Franco Dantas

Licenciatura em Química Aplicada

Follow the red road of triheme cytochromes in *Geobacter sulfurreducens*

Dissertação para obtenção do Grau de
Mestre em Bioquímica Estrutural e Funcional

Orientador: Prof. Doutor Carlos A. Salgueiro, Professor Auxiliar,
Faculdade de Ciências e Tecnologia, Universidade Nova de Lisboa

FACULDADE DE CIÊNCIAS E TECNOLOGIA
UNIVERSIDADE NOVA DE LISBOA

Setembro 2012

Follow the red road of triheme cytochromes in *Geobacter sulfurreducens*

AGRADECIMENTOS

Um trabalho desta natureza envolve a participação directa ou indirecta de várias pessoas a quem desejo expressar os meus agradecimentos. Em especial:

Ao Prof. Doutor Carlos Alberto Gomes Salgueiro, meu orientador, por exigir sempre o melhor dos seus alunos, por todo o conhecimento transmitido e abertura de novas perspectivas, pelo empenho, pelo exemplo de dedicação à investigação científica e ao trabalho de equipa, pela disponibilidade que sempre manifestou, assim como pela confiança e estímulo para prosseguir e nunca desistir, mesmo em situações complicadas.

À Doutora Leonor Morgado, pela disponibilidade para partilhar o conhecimento e as técnicas laboratoriais, bem como pela boa disposição, companheirismo e pelos momentos de descontracção e conversas diárias.

Às minhas colegas Ana Fernandes e Marta Silva, bem como a todos os outros colegas que passaram pelo Lab. 611, pelo trabalho, dinamismo e alegria que colocam no que fazem. Em particular gostaria de agradecer à Leonor Morgado e Ana Fernandes por terem realizado a expressão e purificação das proteinas PpcB-E, procedimento essencial para a obtenção dos resultados presentes nesta tese, no Capítulo 3.

À Doutora Isabel Couto, pela análise criteriosa deste trabalho e pelas preciosas sugestões transmitidas.

Ao Doutor Ricardo Louro e Ivo Saraiva por terem cooperado no trabalho apresentado no Capítulo 3, tendo determinado a geometria dos ligandos axiais das proteínas PpcA-E.

À Prof. Doutora Maria Manuel Marques e ao Doutor Ângelo Figueiredo, pela clarificação das minhas dúvidas relativas ao trabalho realizado no Capítulo 5.

Ao Doutor Filipe Folgosa pela "má/boa disposição", pelos conselhos acertados e por dispensar um espaço na arca a -80ºC, essencial para o armazenamento de células competentes.

Aos meus colegas do Mestrado em Bioquímica Estrutural e Funcional, nomeadamente ao Daniel Duarte, à Diana Ribeiro, à Cláudia Couto, à Sofia Garcia, agradeço o companheirismo e capacidade de trabalho em equipa demonstrados durante os momentos mais difíceis deste mestrado, bem como a boa disposição sempre presente.

Ao Laboratório de RMN da FCT-UNL, integrado na Rede Nacional de RMN e financiado pela Fundação para a Ciência e Tecnologia através Projecto de Re-Equipamento Científico (REDE/1517/RMN/2005), pelo acesso aos espectrómetros de RMN. Agradeço a disponibilidade do Doutor Aldino Viegas, Prof. Doutor Eurico Cabrita e Doutor Ângelo Figueiredo, durante a utilização dos espectrómetros. Ao Doutor Ângelo Figueiredo agradeço em especial a ajuda na

instalação dos programas de cálculo das estruturas de proteínas, essencial para a conclusão da estrutura do PpcAF15L.

À minha grande amiga Sofia Lopes, com a qual, desde os três anos, pude partilhar os bons e os maus momentos.

Aos meus amigos de longa data, nomeadamente "Pessoal fixe de Algés, Miraflores, Linda-a-Velha, Queijas e Dafundo!", bem como aos meus amigos da FCT-UNL pelo apoio, preocupação e por compreenderem o facto, de por vezes, não estar presente quando o trabalho se sobrepunha ao lazer.

Ao Daniel, por estar sempre presente tanto nos períodos conturbados como também nos bons momentos.

Por fim, gostaria de agradecer à minha família, que sempre me apoiou nesta minha teimosia da dita "investigação". Gostaria de agradecer à minha mãe pela paciência demonstrada mesmo nos dias em que o trabalho se prolongou até depois da hora de jantar "sagrada", bem como pelos conselhos e pelas conversas relativas a este mestrado essenciais nos dias mais complicados. Ao "pai Dantas" pela ajuda na construção da caixa de luzes que tem dado muito jeito no Lab 611, assim como pelas poucas, mas acertadas, palavras ditas durante este período. Ao meu irmão Tiago Dantas, deixo aqui também o meu obrigado e fico à espera de ler a sua tese.

ABSTRACT

The bacterium *Geobacter sulfurreducens* (*Gs*) is capable of oxidizing a large variety of compounds relaying electrons out of the cytoplasm and across the membrane in a process designated as extracellular electron transfer. The *Gs* genome was fully sequenced and a family composed by five periplasmic triheme cytochromes c_7 (designated PpcA-E) was identified. These cytochromes play an important role in the reduction of extracellular acceptors. They contain approximately 70 amino acids, three heme groups with bis-histidinyl axial coordination, and share between 57 and 77% sequence identity.

The triheme cytochrome PpcA is highly abundant in *Gs* and is most likely the reservoir of electrons destined for outer surface. In addition to its role in electron transfer pathways this protein can perform e^-/H^+ energy transduction, a process that is disrupted when the strictly conserved aromatic residue phenylalanine 15 is replaced by a leucine (PpcAF15L).

This Thesis focuses on the expression, purification and characterization of these proteins using Nuclear Magnetic Resonance and ultraviolet-visible spectroscopy.

The orientations of the heme axial histidine ring planes and the orientation of the heme magnetic axis were determined for each *Gs* triheme cytochrome. The comparison of the orientations obtained in solution with the crystal structures available showed significant differences. The results obtained provide the paramagnetic constraints to include in the future refinement of the solution structure in the oxidized state.

In this work was also determined the solution structure and the pH-dependent conformational changes of the PpcAF15L allowing infer the structural origin for e^-/H^+ energy transduction mechanism as shown by PpcA.

Finally, the backbone and side chain NH signals of PpcA were used to map interactions between this protein and the putative redox partner 9,10-anthraquinone-2,6-disulfonate (AQDS). In this work a molecular interaction was identified for the first time between PpcA and AQDS, constituting the first step toward the rationalization of the *Gs* respiratory chain.

Keywords: *Geobacter*; electron transfer; multiheme cytochrome; NMR; protein interactions; protein structure

RESUMO

A bactéria *Geobacter sulfurreducens* (*Gs*) tem a capacidade de oxidar uma grande variedade de compostos transferindo electrões para o exterior da célula, num processo designado por tranferência extracelular de electrões. A sequência do genoma da bactéria *Gs* permitiu identificar uma família de cinco citocromos c_7 tri-hémicos, denominados de PpcA-E. Estes citocromos encontram-se localizados no periplasma, onde desempenham um papel importante nas vias metabólicas envolvidas na redução de aceitadores extracelulares. Estas proteínas são constituídas por aproximadamente 70 aminoácidos e três grupos hemo axialmente coordenados por duas histidinas, partilhando 57 a 77% de homologia. Destas proteínas, o citocromo PpcA é o mais abundante, sendo considerado um reservatório de electrões que se destinam à superficie externa desta bactéria. Para além desta função, esta proteína tem ainda a capacidade de acoplar a transferência de electrões e protões. Este mecanismo é interrompido quando o aminoácido fenilalanina 15, um resíduo aromático conservado na família de citocromos c_7, é substituído por uma leucina (PpcAF15L).

Nesta Tese efectuou-se a caracterização destas proteínas supracitadas, utilizando espectroscopia de Ressonância Magnética Nuclear (RMN) e de utravioleta-visível. A orientação dos anéis das histidinas ligadas axialmente aos grupos hemo, bem como a orientação dos eixos magnéticos destes grupos, foram determinadas para cada citocromo tri-hémico de *Gs*. A comparação das orientações em solução com as obtidas por cristalografia de raios-X demonstrou que as mesmas não são conservadas. Os resultados obtidos poderão ser utilizados no futuro como restrições adicionais no cálculo de estruturas em solução no estado oxidado.

Neste trabalho foi também determinada a estrutura em solução do mutante PpcAF15L, bem como as alterações conformacionais associadas à variação do pH. Este estudo permitiu compreender as bases estruturais do mecanismo de transdução de energia e^-/H^+ observado no PpcA.

Por último, os sinais NH da cadeia polipeptídica e das cadeias laterais dos resíduos de PpcA foram utilizados no mapeamento de interacções entre esta proteína e o possível parceiro redox *9,10-anthraquinone-2,6-disulfonate* (AQDS). Foi identificada pela primeira vez uma interacção molecular entre o PpcA e o AQDS, facto que constitui um passo fundamental na compreensão da cadeia respiratória de *Gs*.

Termos chave: *Geobacter*; transferência de electrões; citocromos multi-hémicos; RMN; interacções de proteínas; estrutura de proteínas.

TABLE OF CONTENTS

LIST OF FIGURES

LIST OF TABLES

LIST OF ABBREVIATIONS AND SYMBOLS

1D	One dimensional
2D	Two dimensional
2xYT	2x yeast extract–tryptone medium
AH_2QDS	9,10-Anthrahydroquinone-2,6-disulfonate
ATP	Adenosine triphosphate
AMP	Ampicillin
AQDS	9,10-Anthraquinone-2,6-disulfonate
BLAST	Basic local alignment search tool
BMRB	Biological magnetic resonance data bank
CLO	Chloramphenicol
COSY	Correlation spectroscopy
Dac_7	*Desulfuromonas acetoxidans* c_7 cytochrome
DNA	Deoxyribonucleic acid
EDTA	Ethylenediamine tetra-acetic acid
FID	Free induction decay
Gs	*Geobacter sulfurreducens*
HSQC	Heteronuclear single-quantum coherence
IPTG	Isopropyl β-D-1-thiogalactopyranoside
IUPAC-IUB	International Union of Pure and Applied Chemistry and International Union of Biochemistry
K_D	Equilibrium dissociation constant
lov	Lower limit volume
MacA	Metal reduction associated cytochrome A
MFC	Microbial fuel cells
NCBI	National center for biotechnology information
MW	Molecular weight
NMR	Nuclear magnetic resonance spectroscopy
NOE	Nuclear Overhauser effect
NOESY	Nuclear Overhauser effect spectroscopy
OD_{600}	Optical density at 600 nm
OmcB	Outer membrane associated cytochrome B
OmcE	Outer membrane associated cytochrome E
OmcS	Outer membrane associated cytochrome S
PDB	Protein data bank
PgcA	Periplasmic GEMM-regulated cytochrome A
pI	Isoelectric point
PpcA	*Gs* c_7 cytochrome (GSU0612)
PpcB	*Gs* c_7 cytochrome (GSU0364)
PpcC	*Gs* c_7 cytochrome (GSU0365)
PpcD	*Gs* c_7 cytochrome (GSU1024)
PpcE	*Gs* c_7 cytochrome (GSU1760)
ppm	Parts per million
rmsd	Root mean square deviation

rpm	Rotations per minute
S	Spin angular momentum
SDS-PAGE	Sodium dodecyl sulfate polyacrylamide gel electrophoresis
TCI	Triple-resonance cryoprobe
Tris	Tris(hydroxymethyl)aminomethane
TOCSY	Total correlation spectroscopy
upv	Upper limit volume
UV-visible	Ultraviolet-visible
δ	Chemical shift
ε_{552}	Extinction absorption coefficient at 552 nm

Amino acid abbreviations

Alanine	Ala	A
Arginine	Arg	R
Asparagine	Asn	N
Aspartate	Asp	D
Cysteine	Cys	C
Glutamate	Glu	E
Glutamine	Gln	Q
Glycine	Gly	G
Histidine	His	H
Isoleucine	Ile	I
Leucine	Leu	L
Lysine	Lys	K
Methionine	Met	M
Phenylalanine	Phe	F
Proline	Pro	P
Serine	Ser	S
Threonine	Thr	T
Tryptophan	Trp	W
Tyrosine	Tyr	Y
Valine	Val	V

1. Introduction

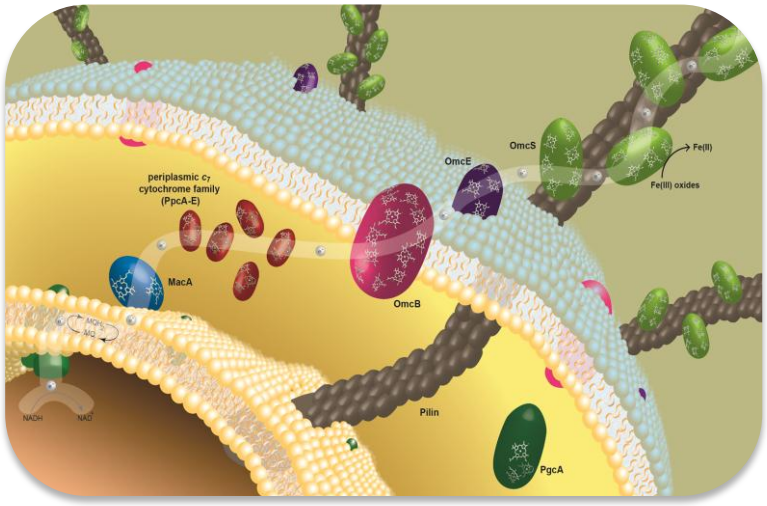

1. INTRODUCTION

The electron transfer process is fundamental in biological systems. Indeed, every cell must solve the problem of energy production in order to survive. The mechanistic studies of electron transfer processes are of great importance to understand the cellular metabolism of living organisms.

An impressive respiratory versatility was identified in some bacteria from the class of δ-proteobacteria, which includes the well characterized *Geobactereacea* family. Members of the *Geobactereacea* are generally the predominant Fe(III)-reducing microorganisms in soils and sediments in which Fe(III) reduction is an important process. However, their respiratory skills are not confined to iron reduction since they can utilize a large diversity of electron donors and acceptors (Table 1) making them important agents in several biogeochemical cycles in natural environments [1].

Table 1 – Respiratory versatility of representative *Geobacter* species. Adapted from [1].

Name	Source	Electron donors oxidized with Fe(III) [a]	Fe forms reduced [b]	Other electron acceptors [a, c]
Geobacter metallireducens	Aquatic sediments	Ac, Bz, Bze, BtOH, Buty, Bzo, BzOH, p-Cr, EtOH, p-HBz, p-HBzOH, IsoB, IsoV, Ph, Prop, PrOH, Pyr, Tol, Val	PCIO, Fe(III)-Cit	Mn(IV), Tc(VII), U(VI), AQDS, humics, nitrate
Geobacter sulfurreducens	Contaminated ditch	Ac, H_2	PCIO, Fe(III)-Cit, Fe(III)-P	Tc(VII), Co(III), U(VI), AQDS, S°, Fum, Mal, O_2
Geobacter bemidjiensis	Fe(III)-reducing subsurface sediment	Ac, Bzo, BtOH, Buty, EtOH, Fum, H_2, IsoB, Lac, Mal, Prop, Pyr, Succ, Val	Fe(III)-Cit,Fe(III)-NTA, Fe(III)-P, PCIO	AQDS, Fum, Mal, Mn(IV)
Geobacter lovleyi	Freshwater sediment	Ac, Bze, Bzo, Buty, Cit, EtOH, For, Glu, Lac, MeOH, Prop, Succ, Tol, YE	Fe(III)-Cit, PCIO	PCE, TCE, nitrate, Fum, Mal, S°, U(VI), Mn(IV)
Geobacter uraniireducens	Uranium-contaminated subsurface sediment	Ac, EtOH, Lac, Pyr	Fe(III)-NTA, Fe(III)-P, PCIO, smectite	AQDS, Fum, Mal, Mn(IV), U(VI)

[a] Abbreviations for electron donors and acceptors: acetate (Ac), 9,10-anthraquinone-2,6-disulfonate (AQDS), benzaldehyde (Bz), benzene (Bze), benzoate(Bzo), benzylalcohol (BzOH), butanol (BtOH), butyrate(Buty), citrate (Cit), p-cresol (p-Cr), elemental sulfur (S^o), ethanol (EtOH), formate (For), fumarate (Fum), glucose (Glu), p-hydroxybenzaldehyde (p-HBz), p-hydroxybenzylalcohol (p-HBzOH), hydrogen (H_2), isobutyrate (IsoB), isovalerate (IsoV), lactate(Lac), malate (Mal), methanol (MeOH), manganese oxide (Mn(IV)), phenol (Ph), propanol (PrOH), propionate (Prop), pyruvate (Pyr), succinate (Succ), tetrachloroethylene (PCE), trichloroethylene (TCE), toluene (Tol), trichloroacetic acid (TCA), valerate (Val), xylose (Xyl), yeast extract (YE).
[b] Fe(III) forms: Poorly crystalline iron oxide (PCIO), ferric citrate (Fe(III)-cit), ferric nitrilotriacetic acid (Fe(III)-NTA), ferric pyrophosphate (Fe(III)-P)
[c] Organism has the ability to reduce the metal but not determined whether energy to support growth is conserved from reduction of this metal.

These bacteria are highly effective in completely oxidizing organic compounds to carbon dioxide under anaerobic conditions with electron transfer to metals [2] or onto graphite electrodes, from which electricity can be harvested [3]. The extracellular electron transfer capability presented by *Geobacter* bacteria has several practical applications in the bioremediation of radioactive and toxic metals in contaminated subsurface environments and also in bioenergy generation, converting organic compounds to electricity in microbial fuel cells (MFC) [4]. However, at present, the power output of MFC is too low for most envisioned applications. The understanding of the respiratory chain is expected to provide valuable information to improve the current-production by these bacteria [5].

1.1 Model for extracellular electron transfer in the bacterium *G. sulfurreducens*

The Gram-negative bacterium *Geobacter sulfurreducens (Gs)* is a well-studied member of the *Geobacter* genus, currently used as a model, because is easily cultured, its whole genome is sequenced and can be genetically manipulated for physiological studies [6, 7]. The genome of *Gs* encodes for 111 *c*-type cytochromes [8], most of them holding more than one *c*-type heme group and mostly located in the periplasm or in the outer membrane. The abundance of multiheme cytochromes suggests that the electron transport pathways in these bacteria are extremely versatile, allowing a precise and adequate physiological response to the diverse metal ions it can find in the natural environments. Gene knockout and proteomic studies on *Gs* cells had contributed to elucidate the participation of some proteins in its electron transport chain. These studies indicated that several *c*-type cytochromes were produced to a much greater extent when Fe(III) served as the electron acceptor, which allowed the evaluation of the role of these cytochromes in electron transport to extracellular Fe(III). These include different proteins; namely MacA, which is thought to be associated with the periplasmic surface of the inner membrane [9], PpcA [10] and related periplasmic low molecular-weight cytochromes, and outer membrane *c*-type cytochromes (OmcB, OmcS, OmcE) [11, 12].

Since *Gs* requires direct contact for reduction of insoluble Fe(III) oxides [13], it is not surprising that some of the most important proteins are located on the outer surface of the *Gs* cells. OmcB (outer membrane associated cytochrome B) is a 89kDa protein holding 12 hemes [14]. This protein is capable of reducing Fe(III) oxide and chelated Fe(III). Deleting the gene for OmcB inhibited reduction of Fe(III) citrate and Fe(III) oxide [12]. OmcE is another *c*-type cytochrome found on the outer cell surface, but its specific location has yet to be pinpointed. This protein has not been purified yet, but is predicted to have a molecular weight of 32kDa and four heme groups [11].

OmcS is a six-heme *c*-type cytochrome with a molecular weight of 47kDa [15], specifically associated with the *pili* of *Gs* [16] and is required for growth on Fe(III) oxide, but not Fe(III) citrate [11]. Other cytochromes of interest are MacA (metal reduction associated cytochrome A) and PgcA (periplasmic GEMM-regulated cytochrome A). MacA is a 35kDa diheme *c*-type cytochrome, which is known to be critical for Fe(III) reduction [9]. The structure of this

cytochrome has been studied by X-ray in three relevant redox states (reduced, semi-reduced and oxidized) [17]. PgcA is a triheme cytochrome located in the periplasm, but still less studied. This protein is more abundant in cells grown on insoluble Fe(III) oxide than soluble Fe(III) citrate [18]. Combining all this information, a model for the electron transfer to the extracellular acceptor Fe(III) in *G. sulfurreducens* was proposed (Figure 1).

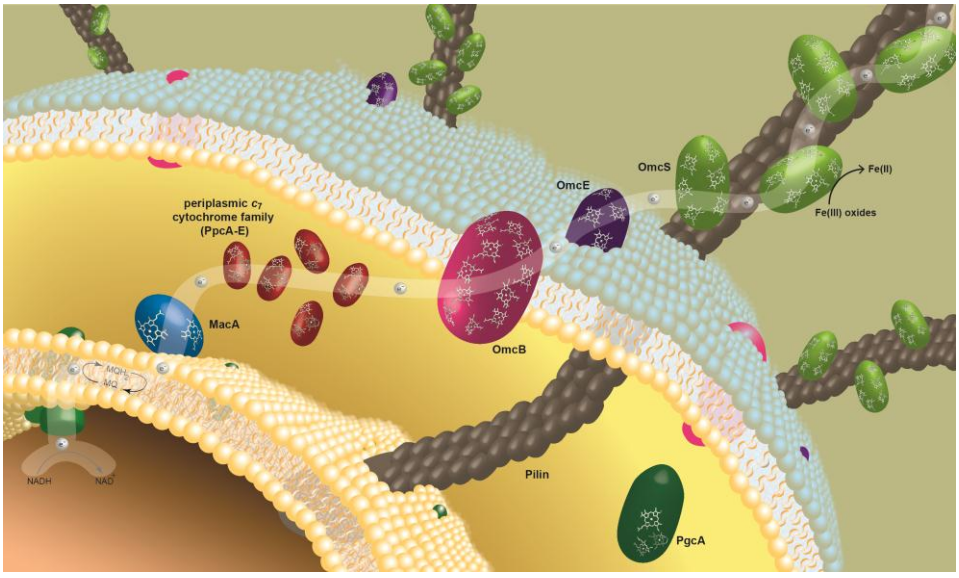

Figure 1 - Proposed model depicting the extracellular electron transfer pathway to Fe(III) oxides in *Geobacter sulfurreducens*. The white path represents the proposed electron transfer pathway. The membrane associated cytochrome MacA receives electrons from the menaquinol (MQH_2)/menaquinone (MQ) pool at the inner membrane and reduces the periplasmic triheme cytochromes (PpcA-E). These cytochromes mediate the electron transfer from the periplasm to the outer membrane associated cytochromes (OmcB, OmcE and OmcS) that are likely to be directly involved in the reduction of insoluble Fe(III) oxides. OmcS was shown to be localized along the *pili* when *Gs* grows in Fe(III) oxides.

1.2 Structural features of periplasmic triheme cytochromes of *G. sulfurreducens*

A family composed by five low molecular weight (~10kDa) cytochromes c_7, designated by PpcA, PpcB, PpcC, PpcD, and PpcE was identified in the periplasm of *G. sulfurreducens*. It is believed that these five periplasmic proteins play an important role in the reduction of extracellular acceptors by bridging the electron transfer between the cytoplasm and cell exterior. These five small periplasmic proteins, containing approximately 70 residues, show a high structural homology, and share 77% (PpcB), 62% (PpcC), 57% (PpcD) and 65% (PpcE) amino acid sequence identity with PpcA [19] (Figure 2).

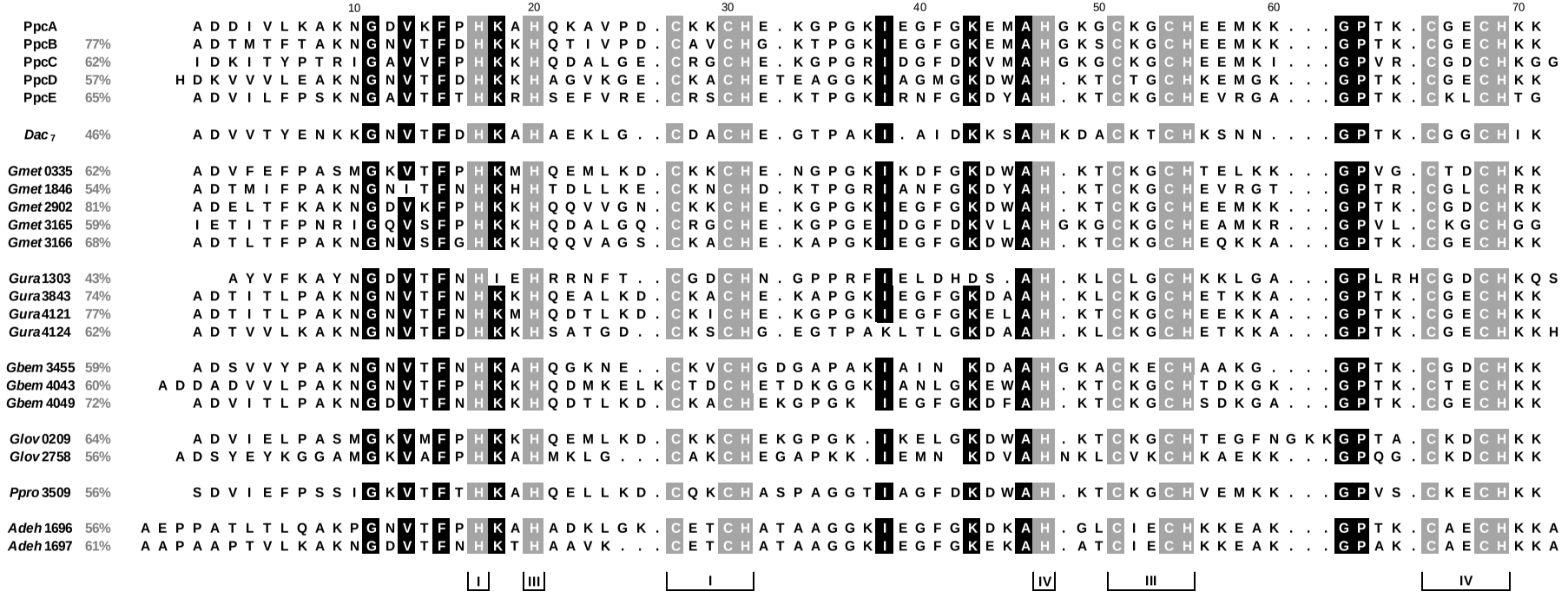

Figure 2 - Alignment of cytochromes c_7 amino acid sequences. PpcA-E, *Geobacter sulfurreducens*; *Dac*$_7$, *Desulfuromonas acetoxidans*; *Gmet*, *Geobacter metallireducens*; *Gura*, *Geobacter uraniireducens*; *Gbem*, *Geobacter bemidjiensis*; *Glov*, *Geobacter lovleyi*; *Ppro*, *Pelobacter propionicus*; *Adeh*, *Aneromyxobacter dehalogenans*. The numbers refer to the gene that encodes for each cytochrome. The conserved residues in the proteins are boxed: heme attached (gray) and non-heme attached residues (black). The specific heme and the respective attached residues are indicated on the bottom of the last cytochrome c_7 amino acid sequence. The sequence identity for each cytochrome in relation to PpcA is also indicated.

Using the PpcA amino acid sequence, we searched the non-redundant amino acid database of NCBI using the Basic Local Alignment Search Tool (BLAST) [20] and in addition to these five cytochromes c_7 mentioned above, 18 additional cytochromes c_7 were found: five from *Geobacter metallireducens*, four from *Geobacter uraniireducens*, three from *Geobacter bemidjiensis*, two from *Anaeromyxobacter dehalogenans* and *Geobacter lovleyi*, and one from *Desulfuromonas acetoxidans* strain 5071 and *Pelobacter propionicus*. All of these bacteria from the δ-proteobacteria class have the ability to use Fe(III) as a terminal electron acceptor [21, 22]. All of these proteins contain three *c*-type heme groups covalently linked to the polypeptide chain by two cysteine residues of the conserved CXXCH binding motif (where X corresponds to any amino acid). A sequence alignment of these proteins is depicted in Figure 2 and shows that of the 21 highly conserved residues, only nine are not cysteine or histidine residues directly involved in heme binding.

Amongst these 23 cytochromes c_7, the best studied one are the family of five periplasmic proteins from *G. sulfurreducens* (PpcA-E) and the triheme cytochrome from *D. acetoxidans* (Dac_7) [23]. The crystal structures of these cytochromes have been determined and are indicated in Figure 3.

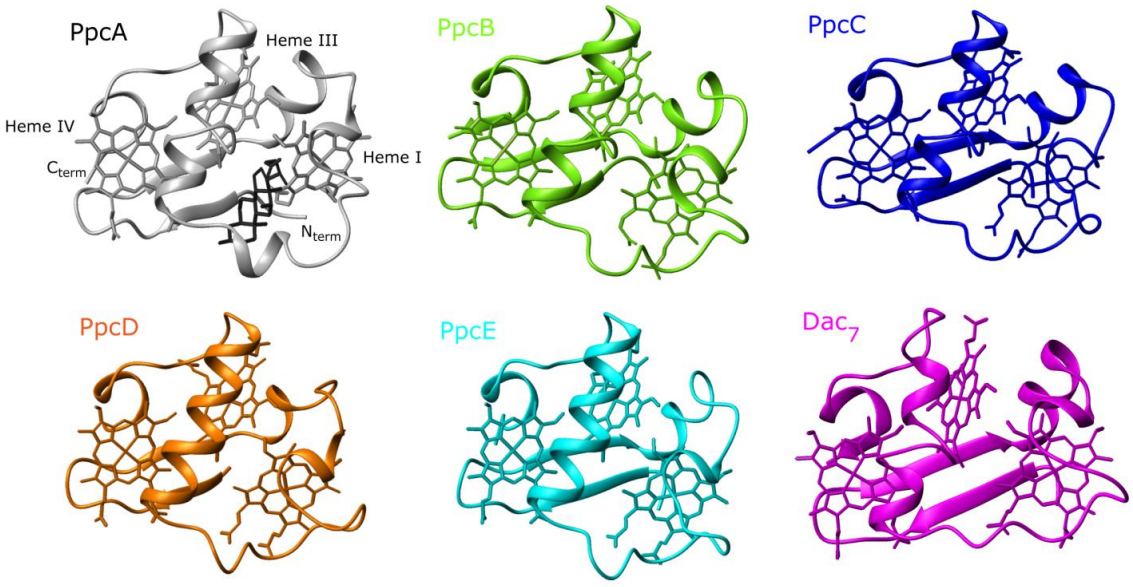

Figure 3 - Crystal structures of the five c_7 cytochromes from *G. sulfurreducens* and *D. acetoxidans*. PpcA is represented in gray with the deoxycholate acid molecule used for crystallization in black (PDB 1OS6 [19]), PpcB in green (PDB 3BXU [24]), PpcC in blue (PDB 3H33), PpcD in orange (PDB 3H4N), PpcE in cyan (PDB 3H34) [25] and Dac_7 in magenta (PDB 1HH5) [23]. PpcB and PpcD displayed two molecules in the crystal asymmetric unit (monomers A and B) and monomer A is represented. The molecules are all in the same orientation.

The tertiary structure of all of the proteins is similar, although local variations were observed in their structures. As depicted in Figure 3, a two-strand β-sheet at the N-terminal is conserved in all the structures, and is followed by different helical regions in the different proteins [19, 24, 25]. The most conserved region is the positively charged surface around heme IV and the

lowest similarity is found near heme I [25]. The heme core structures of the cytochromes c_7 are similar, with hemes I and III roughly parallel to each other and both nearly perpendicular to heme IV [19, 24, 25]. The spatial arrangement of the hemes in cytochromes c_7 is superimposable with those of the structurally homologous tetraheme cytochromes c_3, with the sole difference being the absence of heme II and the corresponding polypeptide segment. For this reason, the three heme groups in cytochromes c_7 have been numbered as I, III and IV. In these cytochromes all hemes are axially coordinated by two histidine residues and are low-spin, both in the diamagnetic reduced (Fe(II), S=0) and in the paramagnetic oxidized (Fe(III), S=½) forms. Typical spectral signatures are observed in this case, where *c*-type cytochromes hold all hemes in the low spin state. To illustrate these features, the UV-visible spectrum obtained for PpcA is indicated in Figure 4.

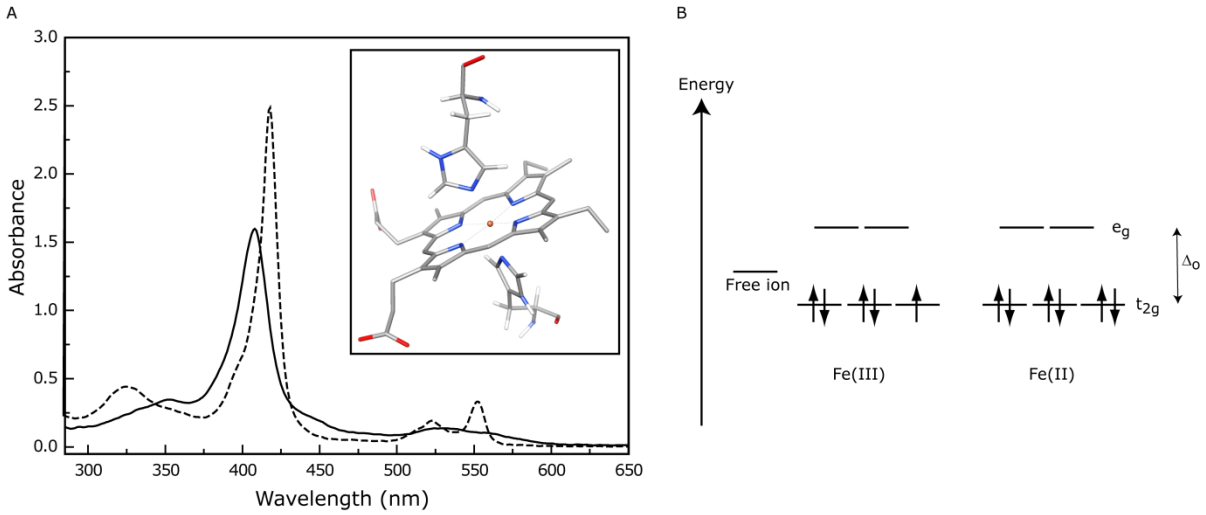

Figure 4 – Spectroscopic properties of *c*-type heme proteins and electronic properties of iron present in these proteins. A) Typical UV-visible absorption spectra for a *c*-type heme protein. The oxidized form (solid line) is dominated by a band with a maximum at 406nm (Soret band), whereas for the reduced form (dashed line), three bands are observed at 417nm (Soret band), 522nm (β band) and 552nm (α band) [26]. The inset displays a *c*-type heme axially coordinated by two histidine residues. B) Spin-states of octahedral Fe(III) and Fe(II) at low spin state, where the crystal field, Δ_o, is higher than the energy required to pair electrons in the same orbital, P (Δ_o>P).

Recently the solution structure of the periplasmic PpcA (with an average rmsd of 0.25Å for the backbone atoms and 0.99Å for all heavy atoms) was determined by Nuclear Magnetic Resonance spectroscopy (NMR) [27] and allowed to fingerprint the residues involved in the redox-Bohr effect, a crucial property for the functioning of PpcA at a physiological pH. The comparison of the solution and crystal structures of PpcA revealed that the general fold and the relative positions of the three hemes are similar, with a good agreement between the consensus secondary elements in both structures. However, Fe-Fe distances and angles between the heme planes in the PpcA crystal structure are different due to the binding of the additive deoxycholate [25]. The differences between the solution and crystal structures of PpcA are not limited to the heme core but extend beyond. In particular, significant differences are observed in the polypeptide region between His^{17} and Glu^{39} that surrounds heme I (Figure 5).

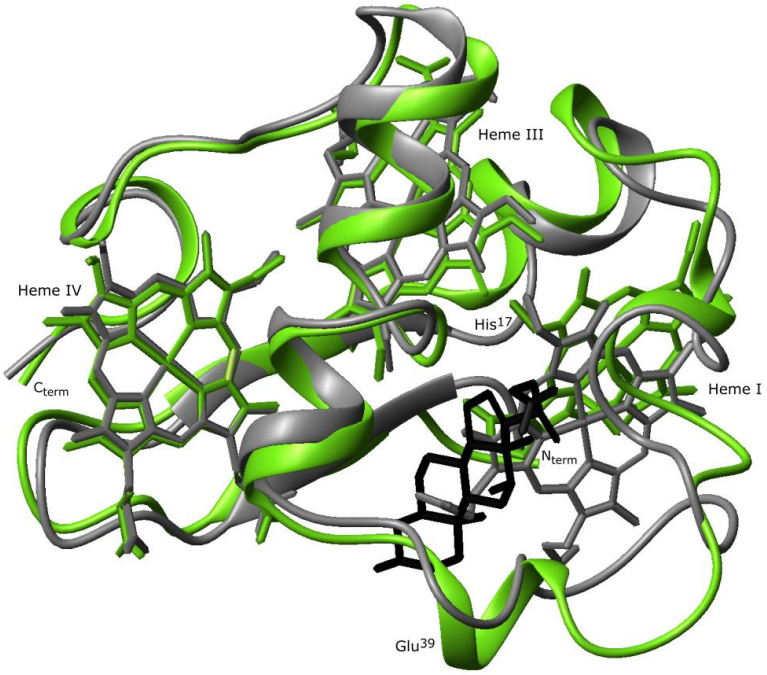

Figure 5 - Comparison of PpcA lowest energy solution structure (PDB 2LDO) [27] with PpcA crystal structure (PDB 1OS6) [19]. Structures were superimposed in MOLMOL using backbone atoms. PpcA solution structure is colored light gray, and PpcA crystal structure is green. The deoxycholate molecule used in the crystallization is represented in black.

1.3 Functional features of periplasmic triheme cytochromes from *Gs*

Despite the structural similarity presented by this family of cytochromes c_7, gene knockout studies of *Gs* cells suggested that these proteins may have functional specificities, since the Fe(III) reduction was differently affected [28]. The characterization of the redox properties of multiheme cytochromes is complex due to the co-existence of several heme groups. Indeed, in monoheme cytochromes only the fully reduced and oxidized states may coexist in solution, whereas in multiheme cytochromes several one-electron reversible transfer steps convert the fully reduced state in the fully oxidized state (Figure 6A). Consequently, different redox stages are defined, each grouping microstates with the same number of oxidized hemes.

The general theoretical framework that allows to study in detail the thermodynamic properties of the redox centers in multiheme proteins to be studied in detail was previously described [29]. Briefly, for a triheme cytochrome, three consecutive reversible steps of one-electron transfer convert the fully reduced state (stage 0, S_0) in the fully oxidized state (stage 3, S_3), and therefore four different redox stages can be defined. At each stage, microstates are grouped with the same number of oxidized hemes (Figure 6A). Additionally, within each microstate, the group responsible for the redox-Bohr effect can be protonated or deprotonated, leading to a total of 16 microstates (Figure 6A). In multiheme cytochromes containing neighbouring heme groups, the reduction potential of each heme is most often modulated by redox interactions with other hemes and by the solution pH (redox-Bohr interactions). Thus, to completely characterize the redox centers of a multiheme cytochrome it is necessary to determine the heme reduction potentials, the redox interactions and the properties of the redox-Bohr center(s). To calculate

these thermodynamic parameters, it is necessary to monitor the stepwise oxidation of each heme oxidation at several pH values. To date, NMR is the only technique that allows probing the individual heme oxidation profiles due to the spectral signatures of the NMR spectra of low-spin multiheme in the reduced and oxidized states (Figure 6B).

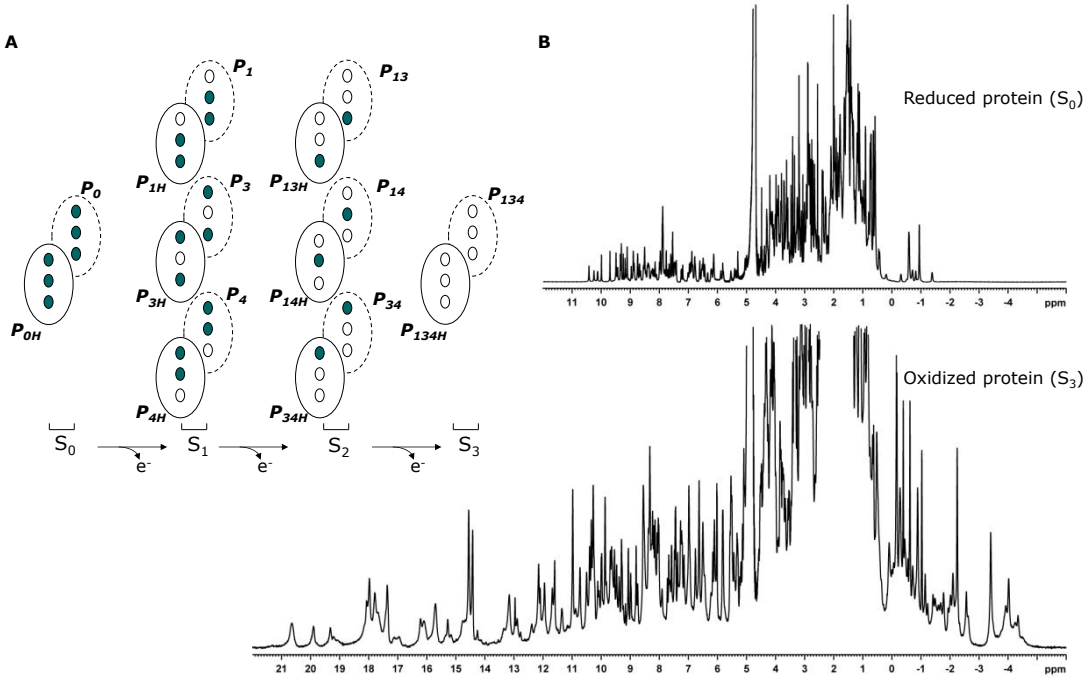

Figure 6 – Electronic distribution scheme and 1D-^{1}H NMR spectra of reduced and oxidized triheme cytochrome. A) Electronic distribution scheme for a triheme cytochrome with a proton-linked equilibrium, showing the 16 possible microstates. The three inner circles represent the hemes, which can be reduced (dark blue) or oxidized (white). The outer circles with solid and dashed lines represent the protonated and deprotonated microstates, respectively. The microstates are grouped according to the number of oxidized hemes in four oxidation stages (S_{0-3}) connected by one electron step. P_{0H} and P_0 represent the reduced protonated and deprotonated microstates, respectively. P_{ijkH} and P_{ijk} indicate the protonated and deprotonated microstates, respectively, where i, j and k represent the heme(s) that are oxidized in that particular microstate. B) 1D-^{1}H NMR spectra of reduced and oxidized triheme cytochrome PpcA obtained at 25 ºC.

In conditions of fast intramolecular electron exchange (between the different microstates within the same oxidation stage) and slow intermolecular electron exchange (between different oxidation stages) on the NMR time scale [24], the heme oxidation fraction can be determined from the chemical shifts of the heme substituents in the different oxidation stages. Heme methyl resonances are the easiest identifiable NMR signals of all heme substituents and their largest paramagnetic shifts make them ideal candidates for following the setpwise oxidation of the heme throughout a redox titration. The paramagnetic shifts of the heme methyls are proportional to the oxidation fraction of a particular heme and as a result, contain information about the redox properties of each heme group [30]. However, the NMR data *per se* are insufficient to determine the absolute thermodynamic parameters and need to be complemented with data from redox titrations monitored by visible spectroscopy [29]. Once determined the thermodynamic parameters it is possible to evaluate the contribution of each microstate and their relevance to the electron transfer mechanism. The thermodynamic

parameters of PpcA, PpcB, PpcD, and PpcE were determined [30] and are summarized in Table 2.

Table 2 - Heme reduction potentials and pairwise interactions (mV) of the fully reduced and protonated forms of PpcA, PpcB, PpcD and PpcE [30].

	Heme redox potentials			Redox interactions			Redox-Bohr interactions		
	I	III	IV	I-III	I-IV	III-IV	I-H	III-H	IV-H
PpcA	-154	-138	-125	27	16	41	-32	-31	-58
PpcB	-150	-166	-125	17	8	32	-16	-9	-38
PpcD	-156	-139	-149	46	3	14	-28	-23	-53
PpcE	-167	-175	-116	27	5	22	-12	2	-13

The heme reduction potentials of PpcA, PpcB, PpcD and PpcE are negative, differ from each other, and cover different functional ranges. These reduction potentials are strongly modulated by heme-heme interactions and by interactions with protonated groups (the redox-Bohr effect), yielding different cooperative networks for each protein. In particular, PpcA displays the necessary properties to couple e^-/H^+ transfer (Figure 7).

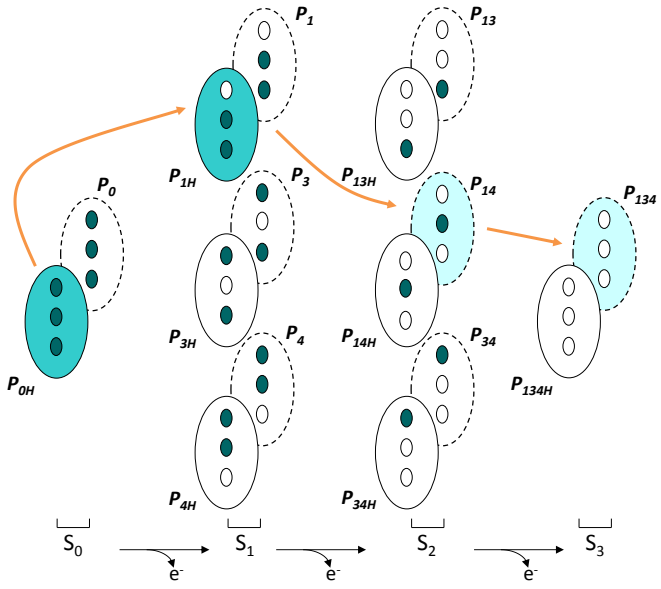

Figure 7 - Preferential pathway for electron transfer in PpcA at pH 7.5. The dominant microstates are highlighted in blue and the preferential electron transfer pathway is indicated by the orange arrows. An e^-/H^+ coupling is observed between oxidation stages 1 and 2.

In the case of PpcA the thermodynamic studies showed that the protein not only transfers electrons but can also couple the transference of proton(s), in a process designated by redox-Bohr effect [30, 31]. As depicted in Figure 7, stage 0 is dominated by the protonated form P_{0H} and stage 1 is dominated by the oxidation of heme I (P_{1H}) while keeping the acid-base center protonated. Stage 2 is dominated by the oxidation of heme IV and deprotonation of the acid-base center (P_{14}), which remains deprotonated in stage 3 (P_{134}). Therefore, a route is defined for the electrons: $P_{0H} \rightarrow P_{1H} \rightarrow P_{14} \rightarrow P_{134}$ [30]. Considering the thermodynamic properties and the periplasmic location of this protein in *Gs*, it was proposed that PpcA might contribute to the transmembrane pH gradient that drives ATP synthesis [32, 33]. Under such hypothesis, PpcA can receive weakly acidic protons (pK_a > 8.0) and electrons from donor(s), which will then be released in the more-acidic periplasmic space with a lower pK_a (<7.5) upon electron transfer to the acceptor according to the scheme represented in Figure 8 [30].

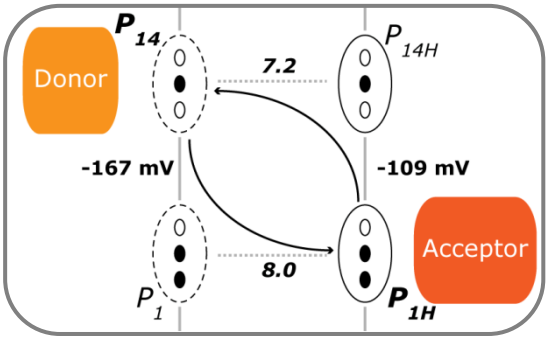

Figure 8 - Thermodynamic and mechanistic bases for energy transduction by PpcA (adapted from [30]). The functional pathway involving the significantly populated microscopic redox states is indicated by arrows. The microstates are labeled as in Figure 7. The redox potential for the equilibrium involving the protonated microstates P_{1H} and P_{14H} (-109 mV) is obtained by the sum of the heme IV redox potential in the fully reduced and protonated protein (-125 mV) and I-IV redox interaction (16 mV).

Given the importance of periplasmic triheme cytochromes in *Gs*, and in particular PpcA, this Thesis focused on the elucidation of structural and functional characteristics of these proteins. The main technique used in this work was NMR spectroscopy, whose basic principles are revisited in chapter two, together with the description of expression, purification and preparation of the protein samples and also, with a brief description of NMR solution structure calculation methods. Chapter three describes the determination of the orientations of the heme axial histidines ring planes and the orientation of the heme magnetic axis for each *Gs* triheme cytochrome. Chapter four reports the determination of the solution structure and the pH-dependent conformational changes of a PpcA mutant. Finally, Chapter five describes the use of ^{1}H and ^{15}N backbone and side chain signals of PpcA to map interactions between this protein and a putative redox partner.

2. Experimental procedures

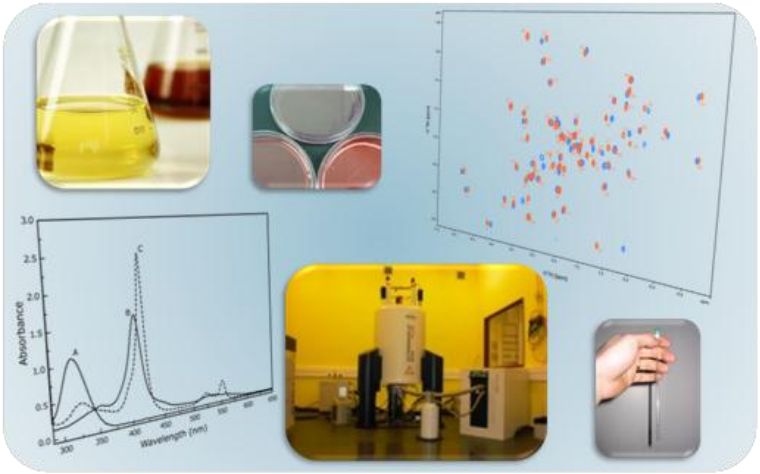

2. EXPERIMENTAL PROCEDURES

2.1 BASIC PRINCIPLES OF NMR

Nuclear magnetic resonance spectroscopy (NMR) studies the properties of molecules containing magnetic nuclei by applying a magnetic field and observing the frequencies of the resonant electromagnetic field. Indeed, in the presence of a magnetic field, a sample can absorb electromagnetic radiation in the radio frequency region at frequencies governed by the characteristics of the sample.

Nuclei are characterized by a quantum spin number (I), which can be determined from the atomic mass and the atomic number. When I=0, there is no nuclear spin and it is NMR silent. Spectra of several nuclei can be readily obtained (*e.g.,* ^{1}H, ^{3}H, ^{13}C, ^{15}N, ^{19}F) since they have spin numbers I of ½ and a uniform spherical charge distribution. Of these by far, the most widely observed in NMR spectroscopy are ^{1}H and ^{13}C. Nuclei with a spin number I =1 or higher have a non-spherical charge distribution. This asymmetry is described by an electrical quadrupole moment, which affects the relaxation time and, consequently, the linewidth of the signals and coupling with neighbouring nuclei. The value of the quantum spin number determines the number of orientations that a nucleus may assume in presence of an external uniform magnetic field in accordance with the formula 2I+1.

For a nuclei with I=½, the energy difference (ΔE) between the energy states α (m_I=+½) and β (m_I=-½) gives rise to the frequency of the spectra, whereas intensities of the signals are proportional to the population difference of the two α and β states. The ratio of the populations in the states is quantitatively described by the Boltzmann equation (Equation 1):

$$\frac{N_\alpha}{N_\beta} = e^{\Delta E/k_B T} \quad (1)$$

where $N_{\alpha,\beta}$ represents the number of nuclei in each possible spin orientation, k_B the Boltzmann constant and T the temperature. It follows that decreasing the temperature, increases the intensity by increasing the population differences. NMR transitions can be enhanced significantly by increasing the strength of the applied magnetic field, since it is proportional to the signals intensity.

In presence of an external magnetic field, nuclei have an intrinsic frequency, which is known as the Larmor frequency. For instance, in a molecule, all protons have the same Larmor frequency. However, the signals of interest are those precessing at frequencies slightly different from the Larmor frequency, an effect caused by the electron density surrounding each individual proton.

The resonance frequencies are expressed in terms of an empirical quantity called chemical shift (δ), which is related to the difference between the resonance frequency (ν) of a nucleus in

question and that of a reference standard (ν_{ref}) (Equation 2). By convention, NMR spectra are plotted with δ increasing from right to left and is expressed in ppm (parts per million).

$$\delta = \frac{\nu - \nu_{ref}}{\nu_{ref}} 10^6 \quad (2)$$

The approach to any structural or mechanistic problem will invariably start with the acquisition of one dimensional (1D) spectra, since these provide the foundations for further work. In a 1D experiment, the FID (free induction decay) is acquired after a radio frequency pulse or pulses (called the preparation period). A plot of the frequencies of the absorption peaks *versus* peak intensities constitutes the 1D-NMR spectrum. For small molecules, a 1D spectrum contains valuable information and can be acquired in a few seconds. On contrary, for a macromolecule the 1D spectrum becomes more complex. For example, for a 1D ^{1}H spectrum of a protein the side-chain region is very crowded with severe spectral overlap due to the large number of backbone and side-chain protons and, concomitantly the spectral assignment is extremely complex. To improve the resolution for spectral assignment, a second frequency dimension is introduced to disperse the signals over two frequency dimensions, forming a two-dimensional (2D) NMR spectrum.

In a 2D experiment, one additional period called the evolution time, which contains a variable time delay t_1, is introduced into the experiment between the preparation and acquisition periods. The evolution delay increases systematically by the same amount of time for each increment during a 2D experiment from zero to the final value determined by the number of increments.

After the experiment is done, all the FIDs are transformed with the same phase parameters. Fourier transformation of the second FID obtained by the t_1 evolution time generates another frequency domain as the transformation of the acquired FIDs. The result of the two Fourier transformations is a two-dimensional NMR spectrum with two frequency axes and an intensity axis on the third dimension that is usually plotted as contours.

The second dimension can be frequency for ^{1}H, which gives a square spectrum with diagonal peaks, or a heteronucleus, which gives an asymmetric spectrum. 2D experiments may also contain other periods in addition to the evolution time, such as a mixing period, τ_m. The 2D techniques used in this work are summarized in Table 3.

Table 3 – 2D NMR standard experiments used in this work. The H and X represent a proton and an heteroatom, respectively. Adapted from [34, 35].

NMR technique	Comment	Correlation	Pulse sequence[a]
^{1}H-^{1}H-COSY	Proton J-coupling typically over two or three bonds		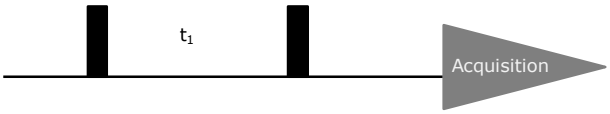
^{1}H-^{1}H-TOCSY	Relayed proton J-couplings within a coupled spin system	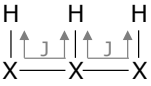	
^{1}H-^{1}H-NOESY	Through-space correlations	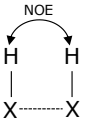	
^{1}H-X-HSQC	One-bond heteronuclear coupling with proton observation		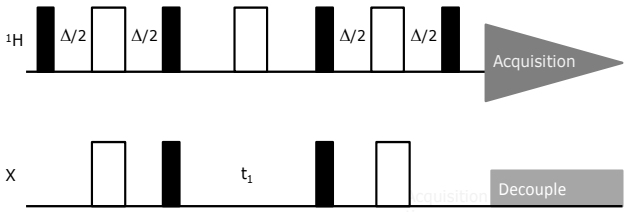

[a] Black and white rectangles represent 90º and 180º radio frequency pulses, respectively. The gray triangle represent the data acquisition period. t_1 and τ_m represent a time delay period and a mixing time period, respectively. A DIPSI-2 pulse train is applied with low power during the spin lock period.

^{1}H-^{1}H COSY (correlation spectroscopy) and ^{1}H-^{1}H TOCSY (total correlation spectroscopy) experiments use scalar coupling (through bond nuclear interactions) to correlate the spins within a spin system. These types of experiments provide geometric information about the molecules via three-bond J coupling in addition to the correlation used in resonance assignment. In the case of the ^{1}H-^{1}H COSY experiment is typically used to correlate protons coupled over two or three bonds. Further information can be achieved using the ^{1}H-^{1}H TOCSY experiment since it correlates the coupled homonuclear spins and those that reside within the same spin system but which may not share mutual couplings. Thus, employs the propagation of magnetization along a continuous chain of spins.

In the ^{1}H-^{1}H-NOESY (nuclear Overhauser effect spectroscopy) experiment the magnetization is exchanged between all protons using the NOE (nuclear Overhauser effect), establishing spatial proximity between protons. The NOE is defined as the change in intensity of one NMR resonance that occurs when another is saturated. It results from dipole–dipole cross-relaxation between nuclei, and its usefulness arises because the strength of a given NOE enhancement is approximately correlated with inter-nuclear separation (actually r^{-6}, where r is the inter-nuclear distance). For small molecules in solution, the NOE is positive (affected resonances increase in

intensity) whereas for larger molecules, the NOE is negative (affected resonances decrease in intensity). The NOESY spectrum can be used both to help assignment (especially of aromatic residues) and to get structural restraints for solution structure determination.

Finally, the HSQC (heteronuclear single-quantum coherence) experiment correlates coupled heteronuclear spins across a single bond and identify directly connected nuclei. The pulse sequence of HSQC (heteronuclear single-quantum coherence) uses the INEPT (insensitive nuclei enhancement by polarization transfer) sequence to transfer proton magnetization into heteronuclear single-quantum coherence. The magnetization is transferred from hydrogen to attached nuclei (*e.g.,* ^{15}N, ^{13}C, ^{19}F) via the J-coupling. In the case of macromolecules, such as proteins, the ^{1}H-^{15}N HSQC experiment is the most standard experiment and shows all H-N correlations. Mainly these are the backbone amide groups are visible, but the NH signals of the side chain of some amino acids are also visible. In this experiment the chemical shift is evolved on the nitrogen and the magnetization is then transferred back to the hydrogen for detection.

2.2 Bacterial growth and protein purification

The triheme cytochromes PpcB, PpcC, PpcD and PpcE were previously purified and were available in the laboratory. The triheme cytochromes PpcA and PpcA with phenylalanine 15 replaced by a leucine (PpcAF15L) were expressed and purified in this work according with the protocol described below. In each case the expression and purification protocols used were identical.

Escherichia coli strain BL21(DE3) harbouring the plasmid pEC86 [36], containing the cytochrome *c* maturation gene cluster, *ccmABCDEFGH* [36], was transformed with the plasmid pCK32, the expression vector containing the gene sequence encoding for each triheme cytochrome following standard protocols. Transformed *E. coli* cells were grown in 2x yeast extract–tryptone medium (2xYT) supplemented with 34μg/mL chloramphenicol (CLO) and 100 μg/mL ampicillin (AMP), both from NZYTech. Cultures were grown aerobically to mid-exponential phase (OD_{600}>1.5) at 30°C and 200rpm after cultures. Production of unlabeled and labelled proteins were carried out through two different processes, respectively: (i) unlabeled protein expression was induced with 10μM isopropyl-β-D-thiogalactopyranoside (IPTG) from NZYTech; (ii) after cultures reaching an OD_{600}>1.5, 1L of 2xYT growth media were harvested by centrifugation at 6400*g* during 30min. The cell pellet was then washed twice with 500mL of a salt solution containing 110mM KH_2PO_4, 240mM Na_2HPO_4, and 43mM NaCl (Panreac). Then, cells were resuspended in 250mL of minimal media containing 22mM KH_2PO_4, 48mM Na_2HPO_4, 8.6mM NaCl, 20mg/L biotin (Sigma), 2mM $MgSO_4.7H_2O$ (Panreac), 0.1mM $CaCl_2$ (Sigma-Aldrich), 5μM $MnCl_2{\cdot}4H_2O$ (Baker's), 10μM $FeSO_4.7H_2O$ (Merck), 20mg/L vitamin B1 (Merck), 4g/L glucose (Sigma) as carbon source, 5g/L $^{15}NH_4Cl$ (CIL isotopes) as nitrogen source and 1mM of the heme percursor δ–aminolevulinic acid (Sigma). The minimal media was supplemented with 34μg/mL CLO and 100μg/mL AMP and then the cultures where incubated at 30ºC and 200rpm, during 1h. The labeled protein expression was induced with 10μM IPTG. After

overnight incubation at 30°C and 180rpm, cells were harvested and the periplasmic fraction was isolated by centrifugation at 6400*g* for 20min at 4°C. The cell *pellet* was gently resuspended in 30ml of lysis buffer (20% sucrose (Fisher scientific), 100mM Tris-HCl (Nzytech) pH 8.0 and 0.5mM EDTA (Sigma) containing 0.5mg/mL of lysozyme (Fluka)), per liter of initial cell culture. Then, lysis buffer was added (30mL of initial cell culture) and the suspension was incubated on ice during 15min and then centrifuged at 15000*g* for 20min at 4°C. The supernatant constituted the periplasmic fraction, which was ultracentrifuged at 150000*g* for 1h 30min at 4°C and then dialysed against 10mM Tris-HCl pH 8.5.

The purification of the proteins was performed using two chromatographic methods: cation exchange and molecular exclusion. For cation exchange chromatography 2x5mL Econo-Pac High S cartridges (Bio-Rad) equilibrated with 10mM Tris HCl pH 8.5 were used and proteins were eluted with a 0-300mM NaCl gradient in 10mM Tris HCl pH 8.5, at a flow rate of 1mL/min. For molecular exclusion chromatography, red coloured fractions were concentrated to 1mL and then injected in a Superdex 75 molecular exclusion column (GE Healthcare) equilibrated with 100mM sodium phosphate buffer, pH 8.0. Protein was eluted at a flow rate of 1mL/min and the protein purity was evaluated by SDS-PAGE (15%), stained with Coomassie brilliant blue (Sigma).

2.3 NMR STUDIES

All of the NMR experiments were acquired in a Bruker Avance III 600 spectrometer equipped with a triple-resonance cryoprobe (TCI). ^{1}H chemical shifts were calibrated using the water signal as internal reference and the ^{15}N and ^{13}C chemical shifts calibrated through indirect referencing [37]. Spectra were processed using TopSpin (Bruker BioSpin, Karlsruhe, Germany) and analysed with the program Sparky.

2.3.1 PREPARATION OF NMR SAMPLES

For NMR studies, ^{15}N-labelled samples were prepared in 92%H_2O/8%$^{2}H_2O$ and unlabelled samples prepared in 92% H_2O/8% $^{2}H_2O$ or in pure $^{2}H_2O$ (CIL isotopes). Protein samples with ~1mM concentration were prepared in 45mM or 80mM phosphate buffer pH 7.1 or 8.0 with NaCl (100mM or 250mM final ionic strength, respectively).

For the experiments in the fully reduced form, the NMR tubes were sealed with a gas-tight serum cap and the air was flushed out from the sample, to avoid oxidation of the samples. Then, NMR samples were reduced directly in the NMR tube with gaseous hydrogen in the presence of catalytic amounts of hydrogenase from *Desulfovibrio vulgaris* (Hildenborough), as previously described [24]. For the reduced samples, the pH was adjusted inside an anaerobic glove chamber (MBraun LABstar) with argon circulation to avoid sample reoxidation.

2.3.2 NMR EXPERIMENTS IN THE REDUCED FORM

For the assignment of protein heme substituents in the reduced form, 2D-NMR experiments including ^{1}H-^{1}H-NOESY with 80ms mixing-time and ^{1}H-^{1}H-TOCSY with 45ms mixing-time, were acquired. 2D-NMR spectra were recorded with 256 scans, and spectral width of 14kHz, using a pulse sequence with water pre-saturation. 2D experiments were acquired with a sweep width of 512Hz in F_2 and 4096Hz in F_1. The experiments were acquired at 16ºC or 25ºC.

For the determination of solution structure of PpcAF15L, the following set of experiments were acquired for (i) ^{15}N labelled in 92% H_2O/8% $^{2}H_2O$: 2D-^{1}H-^{15}N-HSQC; (ii) for unlabelled sample in 92% H_2O/8% $^{2}H_2O$: 2D-^{1}H-COSY, 2D-^{1}H TOCSY with 60ms mixing time and 2D-^{1}H-NOESY with 50ms mixing time. 2D-^{1}H-TOCSY (45ms mixing-time) and 2D-^{1}H-NOESY (100ms mixing-time). NMR spectra were also acquired for the unlabeled sample prepared in pure $^{2}H_2O$ to assist in the assignment of the heme proton signals. Before and after all two dimensional experiments, 1D-^{1}H NMR spectra were recorded in order to verify the protein integrity and fully reduction.

2.3.3 NMR EXPERIMENTS IN THE OXIDIZED FORM

Two-dimensional NMR ^{1}H-^{1}H-NOESY, ^{1}H-^{1}H-TOCSY and ^{1}H-^{13}C HSQC experiments were performed at 16ºC and 25ºC [38]. 2D-^{1}H-NOESY NMR spectra were collected with a mixing time of 80ms and a sweep width of 24kHz in both dimensions. 2D-^{1}H-TOCSY NMR experiments were performed with 45ms mixing-time and a sweep width of 24kHz. The ^{1}H-^{13}C HSQC NMR spectra, obtained from natural abundance samples, were acquired with a sweep width of 24kHz in F_2 and 45kHz in F_1.

2.3.4 pH TITRATION OF THE PPCA MUTANT

The pH titration of PpcAF15L was carried out by ^{1}H-^{15}N-HSQC NMR in the pH range 5.4-9.5 and all ^{1}H and ^{15}N chemical shifts of the polypeptide backbone (except for residues 1 and 2) and side chains were measured. To adjust the pH of the samples minimal amounts of either $NaO^{2}H$ or ^{2}HCl were added inside an anaerobic glove chamber at <1 ppm oxygen, in order to avoid sample oxidation. The weighted average chemical shift ($\Delta\delta_{avg}$) of each backbone and side chain amide was calculated as described in Equation 3:

$$\Delta\delta_{avg} = \sqrt{\frac{\Delta\delta^2{}_H + \frac{\Delta\delta^2{}_N}{25}}{2}} \quad (3)$$

where $\Delta\delta_H$ and $\Delta\delta_N$ are the differences in the ^{1}H and ^{15}N chemical shifts, respectively [39]. This procedure used to estimate the effects of pH changes on the PpcAF15L solution structure was exactly the same used for the wild type [27].

2.3.5 ^{1}H-^{15}N HSQC NMR Titrations of PpcA in the presence of AQDS

A series of ^{1}H-^{15}N-HSQC spectra were acquired on ^{15}N-labeled PpcA in the absence or in the presence of increasing amounts of 9,10-anthraquinone-2,6-disulfonate (AQDS) from Sigma. In each step of the titration, small volumes (3μL) of 0.26M AQDS were added to the NMR tube containing initially 180μL of protein sample, yielding molar ratios [AQDS]/[PpcA] of 0, 1, 3, 4, 5, 7, 10, 15, 20, 30, 35, 40 and 50. The pH of the sample was measured before and after of each experiment. The observed chemical shift changes per residue ($\Delta\delta$) in ^{1}H-^{15}N HSQC spectra of PpcA was calculated according to the Equation 4,

$$\Delta\delta_{comb,j} = \sqrt{(\Delta\delta_H)^2 + (w_i\Delta\delta_N)^2} \quad (4)$$

where $\Delta\delta_H$ is the chemical shift change in ppm in ^{1}H dimension, $\Delta\delta_N$ is the chemical shift change in ppm in ^{15}N dimension and the term $w_i = |\gamma^{15}N|/|\gamma^{1}H|$ compensates the scaling differences between ^{15}N and ^{1}H chemical shifts [40].

By superimposing all ^{1}H-^{15}N-HSQC spectra, the shifted HSQC peaks could be identified and further assigned to the corresponding residues. The differences in ^{1}H and ^{15}N chemical shifts between the NH amide signals of the PpcA in the absence and in presence of AQDS at varying concentrations were calculated. The equilibrium dissociation constant (K_D) was estimated for the amide signals corresponding to the residues with significant chemical shift changes determined for the reduced and oxidized experiments. For the determination of the cut-off value, an iterative procedure was used to calculate a standard deviation to zero, σ_0^{corr} described in Equation 5 [40],

$$\sigma_0^{corr} = \sqrt{\frac{1}{N}\sum(\Delta\delta_{comb,j} - 0)^2} \quad (5)$$

where *N* corresponds to the number of $\Delta\delta_{comb}$ values determined. First the σ_0 for all $\Delta\delta_{comb}$ values is calculated, all values outside three times σ_0 (0.5 % of the residues do not belong to the distribution) are removed and a first corrected standard deviation σ_0^{corr} is obtained for the remaining $\Delta\delta_{comb}$ values. If there are $\Delta\delta_{comb}$ values would be larger than three times that of the new σ_0^{corr} value, they would be excluded again and another σ_0^{corr} would be calculated. This procedure was repeated until no $\Delta\delta_{comb}$ value larger than three times that of the actual σ_0^{corr} remained. That final σ_0^{corr} value was taken as cut-off criterion.

The equilibrium dissociation constant was determined under fast exchange conditions and assuming a single site binding with 1:1 stoichiometry, according to the following equilibrium: P + L ↔ PL, where P and L correspond to PpcA and AQDS, respectively. Knowing the $\Delta\delta_{comb}$ values of each NH signal, the total concentration of protein (c_P^{total}) and ligand (c_L^{total}) and using the Equation 6, the K_D values for each NH signal were estimated adjusting the calculated values to the experimental data, using Excel Solver tool. The changing cells were the K_D value and $\Delta\delta_{P-L,j}$ which is described by Equation 7.

$$\Delta\delta_{comb,j} = (\Delta\delta_{P-L,j})\frac{(c_P^{total}+c_L^{total}+K_D) - \sqrt{(c_P^{total}+c_L^{total}+K_D)^2 - 4.c_P^{total}+c_L^{total}}}{2.c_P^{total}} \quad (6)$$

$$\Delta\delta_{P-L,j} = \sqrt{\sum(w_i(\delta_{PL} - \delta_P))^2} \quad (7)$$

δ_{PL} and δ_P correspond to the chemical shift in the fully complexed state and in the ligand free state, respectively.

2.4 Methodology used in the Assignment of the NMR signals

2.4.1 Assignment of the heme substituents in *Gs* triheme cytochromes

Due to the small size of PpcA (71 residues) the polypeptide chain is essentially confined to the heme core of the protein formed by the three heme groups. Therefore, the heme core of the protein is an excellent probe to detect important changes in the overall fold of the protein polypeptide chain. In addition, in the diamagnetic reduced form, the proton chemical shifts of the heme substituents are essentially affected by the heme ring-current effects. Thus, for fully reduced proteins typical regions for the signals of the heme substituents can be easily identified in 2D-^{1}H-NOESY NMR spectra: 8 to 10ppm, meso protons (H5, H10, H15 and H20); 6 to 8ppm, thioether methines (3^1H and 8^1H); 3 to 5ppm methyl groups (2^1CH_3, 7^1CH_3, 12^1CH_3, 18^1CH_3) and 3 to -1ppm, thioether methyls (3^2CH_3 and 8^2CH_3).

In the reduced state, the first step of assignment was the analysis of 2D-^{1}H-TOCSY NMR spectra in which we identified connectivities between a thioether methine (3^1H or 8^1H) and a thioether methyl group (3^2CH_3 or 8^2CH_3), as shown in Figure 9. Indeed, these are the only protons that are in the same spin system and can be easily detected in 2D-^{1}H-TOCSY experiments.

2D-^{1}H-NOESY experiments allow detecting spatial correlation between nuclei that are typically closer than 5 Å. Thus, as depicted in Figure 9 meso protons present a characteristic pattern of short-range intraheme connectivities observed in 2D-^{1}H-NOESY spectra: protons H15 are not connected to either methyl groups or thioether substituents; protons H20 are connected to two heme methyls (2^1CH_3 and 18^1CH_3); and the only ambiguity arises from H5 and H10 protons, which both present connectivities with a thioether methine, a thioether methyl and one heme methyl group. This ambiguity was solved by observing the connectivities between one of the heme methyls near the H20 protons (2^1CH_3 and 18^1CH_3) with the closest tioether methyl (3^2CH_3) which were inequivocally assign in the 2D-^{1}H-TOCSY. This allowed connecting H20 and H5 faces of each heme. The heme methyls 7^1CH_3 are part of H5 faces and also show connectivities with thioether groups (8^1H and 8^2CH_3), which are in H10 faces. After the identification of these three heme faces, H15 protons were identified by observing the connectivities between cross-peaks that connect H15 and 12^1CH_3 or 18^1CH_3 protons (Figure 9).

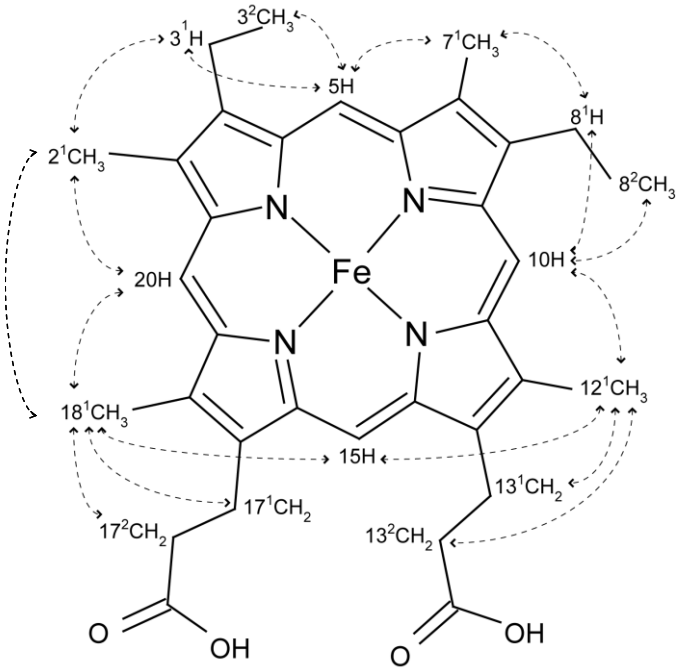

Figure 9 - Diagram of heme *c* numbered according to the IUPAC-IUB nomenclature [41]. The arrows indicate the typical NOE connectivities used to assign the heme substituents.

On the other hand, in the paramagnetic oxidized state in addition to the ring-current, the intrinsic (from own heme) and the extrinsic (from neighbour hemes) paramagnetic contribution due to the presence of unpaired electrons strongly contributes to the final observed chemical shift of the heme substituents, making their assignment more complex. Indeed, in the oxidized form the same type of signals are differently affected by the paramagnetic centers, show different levels of broadness and are spread all over the entire NMR spectral width. Therefore, the chemical shifts of the heme substituents in the oxidized form are completely different in comparison with those observed in the fully reduced proteins. Consequently, a different NMR assignment strategy was used to assign the heme signals in the oxidized form. In this case, ^{1}H-^{13}C-HSQC NMR experiment is very useful to map the heme substituent signals because typical ^{1}H-^{13}C regions can be identified for some of the heme substituents. The propionates αCH_2 protons ($17^{1}CH_2$ and $13^{1}CH_2$) are identified in ^{1}H-^{13}C HSQC NMR spectrum, whereas the intraheme conectivities with the propionates βCH_2 ($17^{2}CH_2$ and $13^{2}CH_2$) are obtained from the analysis of 2D-^{1}H-TOCSY spectrum and then confirmed in ^{1}H-^{13}C-HSQC NMR spectra at the typical region of propionates βCH_2. Afterwards, in 2D-^{1}H-NOESY spectra we identified the cross-peaks of each propionate proton with those of the closest heme methyl ($18^{1}CH_3$ and $12^{1}CH_3$).

Since the structures of *Gs* triheme cytochromes have been previously determined [19, 24, 25], the assignment of the heme substituents in the reduced and oxidized form were further confirmed by examining the expected interheme NOE connectivities measured from the 2D-^{1}H-NOESY NMR spectra acquired at different mixing times.

2.4.2 Assignment of the protein backbone and side chain signals in PpcA mutant F15L

Spectra for the PpcAF15L protein were compared with the corresponding spectra previously obtained for the wild-type protein [42]. For many spin-systems, the chemical shifts differed by less than 0.1ppm and thus it was possible to obtain their assignment by simple comparison. The assignment procedure for the remaining signals was the same as described for the wild-type protein [27]. Briefly, examination of the 2D-^{1}H-TOCSY and 2D-^{1}H-COSY spectra allowed the identification of the spin-systems according to their type. Analysis of the NOESY spectra and identification of HN–HN, HN–Hα and HN–Hβ connectivities between different spin-systems allowed the sequential assignment. Stereospecific assignments were obtained in the process of structure calculation using the program GLOMSA.

2.5 Determination of the axial ligand geometry

The ^{13}C chemical shifts of the four members of the cytochrome c_7 family (PpcB-E) heme α-substituents were determined at 16ºC and 25ºC. The semi-empirical model of the heme molecular orbitals was implemented in MATLAB using a Nelder–Mead Simplex algorithm for fitting the ^{13}C paramagnetic shifts [43, 44]. The unpaired electron from the iron d orbitals is delocalized into the π orbitals of the prophyrin ring. The ^{13}C Fermi contact shifts of the heme α-substituents are proportional to the unpaired electron density on the adjacent carbon atom belonging to the porphyrin conjugated system. The shape of the heme frontier molecular orbitals can thus be determined from the Fermi contact shifts of the heme α substituents and is defined by the orientation of the rhombic perturbation (θ), which mixes the orbitals and their energy splitting (ΔE). Since the paramagnetic shifts for the heme nuclei are dominated by the Fermi contact shift, no correction for the pseudocontact shift was made [45]. It was shown before that the orientation of the rhombic perturbation agrees with the bisector of the acute angle defined by the normals to the heme axial histidine planes, which is defined relative to the Fe–N_C axis being positive towards N_B (Figure 10) [46].

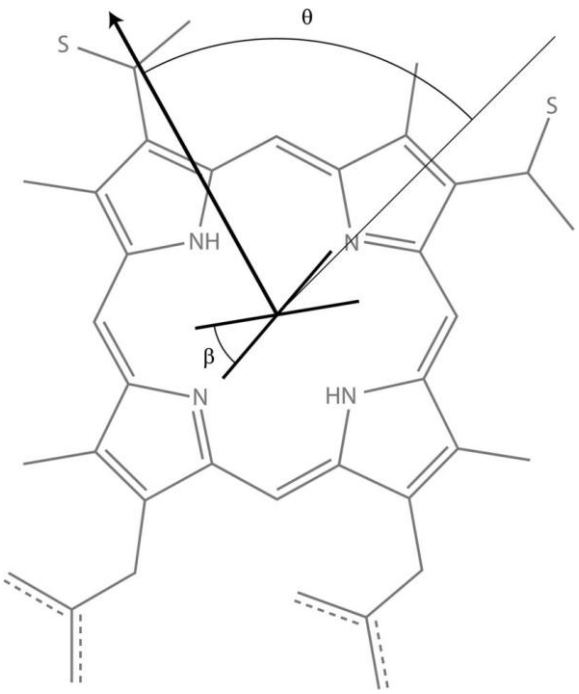

Figure 10 - Diagram of heme *c* showing the geometric parameters β and θ. The thin line represents the N_A–N_C direction, the arrow represents the orientation of the rhombic perturbation, whereas the two short and thick lines represent the projection of the axial histidine planes on the heme.

The energy splitting has similar values to the rhombic splitting of the Kramers doublets that arise from the iron d_{xz} and d_{yz} orbitals mixing when in a cubic crystal field with axial and rhombic distortions [46]. The ΔE value relates to the acute angle formed by the heme axial histidine planes (β) *via* the empirical equation $\Delta E = (5 + \cos 4\theta)\cos\beta$. Therefore the magnetic axes can be placed relative to the heme considering that the *zz* axis is perpendicular to the macrocycle plane and the *yy* axis is related to the orientation of the rhombic perturbation by counter-rotation [47, 48].

2.6 Structure calculation and analysis

As for the wild-type protein, the solution structure of PpcAF15L was calculated with the program PARADYANA. In each calculation, 200 conformers were determined and the 20 structures with lowest target function value were selected for further visual analysis using the program CHIMERA (version 1.5.1) [49]. In the final calculation, the 20 structures with lowest target function value were selected. Finally, the program MOLMOL [50] was used to superimpose, identify elements of secondary structure in the final set of conformers and also to compare the structures obtained for mutant and wild-type proteins. The quality of the structures was analyzed with PROCHECK-NMR [51].

2.7 UV-VISIBLE STUDIES

All sample manipulations were performed under strict anaerobic conditions in an argon filled glove-box (atmospheric O_2 < 1ppm). UV-visible absorbance spectra were acquired between 290nm and 650nm, in an Evolution 300 UV-Vis Spectrophotometer (Thermo Fisher Scientific) equipped with a Fiber Optic Coupler and fiber optics, which allows measuring the samples inside the anaerobic chamber, even if the spectrometer is outside. All samples were prepared inside the anaerobic chamber. The quantification of protein and sodium dithionite solutions was performed inside the anaerobic chamber using the same spectrometer.

2.7.1 ASSAYS OF AH_2QDS OXIDATION COUPLED TO PPCA REDUCTION

For the assays of AH_2QDS (9,10-anthrahydroquinone-2,6-disulfonate) oxidation coupled to PpcA reduction, 12.3μL of 2.5mM AQDS were added to 975μL of 45mM phosphate buffer pH 7.1 (100mM final ionic strength) and anaerobically reduced with equivalent amounts of 2.75mM sodium dithionite (11.6μL). Before and after the reduction of AQDS to AH_2QDS with sodium dithionite, an absorption spectrum was acquired. Then, increasing amounts of 0.31mM PpcA in the oxidized form at molar ratios [AQDS]/[PpcA] (added volume) of 0.25 (11μL), 0.5 (11μL) and 1 (22μL) were added to the sample containing AH_2QDS. After each addition an absorption spectrum was acquired.

2.7.2 ASSAYS OF AQDS REDUCTION COUPLED TO PPCA OXIDATION

The purified PpcA was dissolved in 990μL (0.31mM) of 45mM phosphate buffer pH 7.1 (100mM final ionic strength) and anaerobically reduced with 4μL of 2.75mM sodium dithionite. Before and after the reduction of the protein with sodium dithionite an absorption spectrum was acquired. Then, increasing amounts of 2.5mM AQDS at molar ratios [AQDS]/[PpcA] (added volume) of 0.25 (0.5μL), 0.5 (0.5μL), 1 (1μL) and 40 (40μL) were added to the protein sample. After each addition an absorption spectrum was acquired.

3. Orientation of the axial ligands and magnetic properties of the hemes in the cytochrome c_7 family[1]

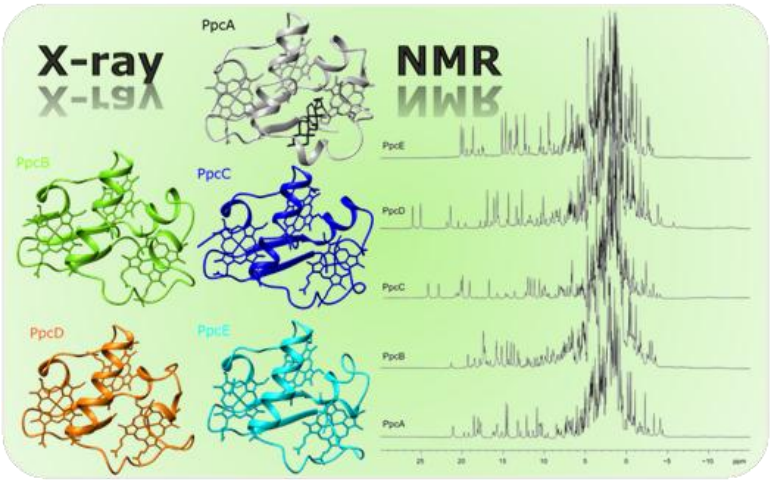

[1] Partially reproduced from JM Dantas, IH Saraiva, L Morgado, MA Silva, M Schiffer, CA Salgueiro, RO Louro (2011) Orientation of the axial ligands and magnetic properties of the hemes in the cytochrome c_7 family from *Geobacter sulfurreducens* determined by paramagnetic NMR, Dalton Trans 40, 12713-12718 (http://dx.doi.org/10.1039/c1dt10975h), according to the Editors' Copyright Policy.

I would like to express my acknowledgement to L Morgado and AP Fernandes for producing and purifying the four c_7 triheme periplasmic cytochromes from Geobacter sulfurreducens (PpcB-E), essential to perform this work. I would also like to acknowledge to I Saraiva and RO Louro, who determined the axial ligand geometries of these cytochromes.

3. ORIENTATION OF THE AXIAL LIGANDS AND MAGNETIC PROPERTIES OF THE HEMES IN THE CYTOCHROME C_7 FAMILY FROM *GS*

Identification of the structural bases that support the different functional properties of the family of five c_7 triheme periplasmic cytochromes from *G. sulfurreducens* requires comparison of high-quality structures obtained in different redox and protonation states that allow the mapping of redox and pH-linked differences. Solution structure determination by NMR provides the necessary degree of detail, while allowing for a precise control of the experimental conditions. However, structure determination of low-spin cytochromes in solution requires the use of paramagnetic constraints to achieve good precision and accuracy [52, 53]. The quality of these constraints depends on the correct placement of the magnetic axes that define the magnetic susceptibility tensor of the unpaired electrons. These axes can be defined from the structure, provided that the orientation of the axial ligands is well defined [54, 55]. Alternatively, they can be defined from paramagnetic NMR chemical shifts of the substituents at the heme periphery (hereafter α-substituents). Empirical equations using ^{1}H paramagnetic shifts of the heme methyls at a single temperature were proposed to define the geometry of the axial ligands and therefore of the magnetic axes [48, 56, 57].

With modern NMR equipment it is possible to obtain ^{13}C data using natural abundance samples. This allows for the use of the ^{13}C-paramagnetic shifts of all eight substituents at the periphery of the heme in the framework of a semi-empirical model of the heme molecular orbitals [43]. Application of this strategy provided the relative orientation of the PpcA–E heme axial histidines ring planes, as well as the orientation of the heme magnetic axes [47]. For some hemes significant differences exist between the orientation of the axial ligands and the magnetic axes obtained from the NMR data and the orientation taken for the X-ray coordinates.

The family of five triheme periplasmic cytochromes from *G. sulfurreducens* shows structural diversity of the heme core. Structural characterization of the relative orientation of the axial ligands of these proteins by ^{13}C-paramagnetic NMR was carried out. The structures in solution were compared with those obtained by X-ray crystallography. For some hemes significant differences exist between the two methods such that orientation of the magnetic axes obtained from NMR data and the orientation taken from the X-ray coordinates differ. The results allowed the orientation of the magnetic axes to be defined confidently with respect to the heme frame in solution, a necessary step for the use of paramagnetic constraints to improve the complete solution structure of these proteins.

3.1 RESULTS

With the exception of the protein PpcA, which was studied by L Morgado [38], in this work it was performed the resonance assignment of the heme substituents for the other members of *Gs* triheme cytochrome family (PpcB-E) in the oxidized state. All of these proteins were previously produced and purified. The diversity among the heme axial ligand geometry within the *Gs* triheme cytochromes is evident from the observation of the low field region in the 1D-^{1}H NMR spectra (Figure 11), which is dominated by the signals of heme methyls and propionate groups, as well as those of aliphatic side chain of the heme axial histidines.

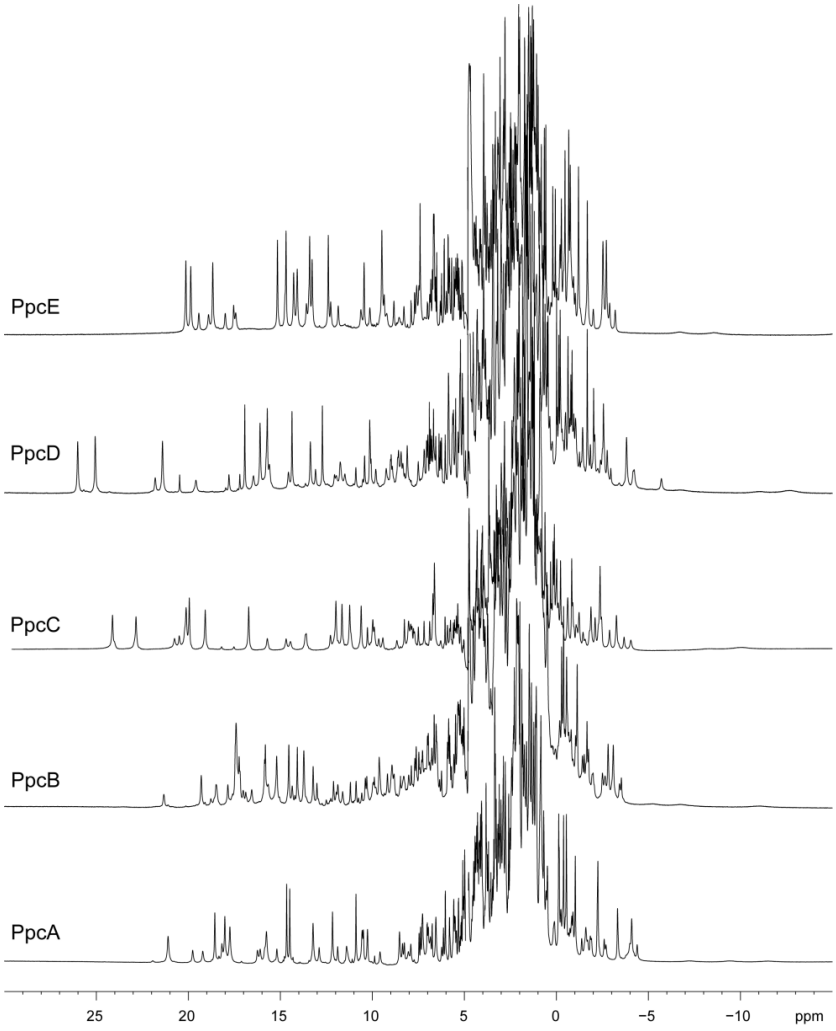

Figure 11 - 1D-^{1}H NMR spectra obtained for PpcA–E in the oxidized state (25ºC and pH 7.1) [58].

The comparison of these spectral regions, among the entire *Gs* triheme cytochrome family, shows that the pattern of the more paramagnetic shifted signals, typically belonging to heme methyls, is quite distinct. Since the methyl chemical shifts depend on the relative orientation of the heme axial histidine ring planes, this observation reveals that the cytochromes have considerable differences in their axial ligand geometry in solution. In order to determine such geometries, as well as the orientation of the magnetic axes relative to each heme, the ^{13}C

chemical shifts of the heme α-substituents were specifically assigned for each protein in the oxidized state.

3.1.1 RESONANCE ASSIGNMENT

The unambiguous assignment of the 16 heme methyl proton signals in the fully reduced protein was obtained for all triheme cytochromes with the exception of PpcC [24, 30]. In general, the assignment of these resonances could assist the assignment of ^{1}H NMR resonances of the heme α-substituents in the oxidized state [45, 46].

As described in section 1.3, for a triheme cytochrome, three consecutive reversible steps of one-electron transfer convert the fully reduced state to the fully oxidized state, and therefore four different redox stages can be defined (Figure 6). Thus, on the NMR timescale, under conditions of fast intramolecular electron exchange (between the different microstates within the same oxidation stage) and slow intermolecular electron exchange (between different oxidation stages), the individual heme signals can be discriminated in the different oxidation stages. In such conditions the heme methyl signals can, in principle, be followed to their final position in the fully oxidized protein using 2D-EXSY NMR experiments. Under such experimental conditions and in absence of severe signal overlapping, heme methyl signals can be traced to their final position in the oxidized spectra providing solid starting points that facilitates the assignment of the heme α-substituents. The strategy to assign the ^{13}C and ^{1}H resonances of these substituents is summarized in section 2.4.1 and was used in the present work to assign the heme α-substituents of PpcB, PpcC, PpcD, PpcE in the oxidized state (Appendix B - Table B3).

The assignment of these signals in PpcA was reported [38] and is not addressed here. In the case of PpcB, several exchange connectivities between heme methyl signals for the fully reduced and for the one-electron oxidized protein were observed. However, due to the severe overlap of these signals for one-electron oxidized protein a confident assignment to their final position could not be obtained. For PpcC multiple conformations were observed at intermediate oxidation stages but not in the fully reduced or oxidized states [59]. Thus, for these cytochromes the assignment was carried out independently of any specific assignment of the heme methyl groups followed by 2D-EXSY NMR experiments. On the contrary, for PpcD and PpcE it was possible to follow some heme methyl signals with confidence from the reduced to their final position in the oxidized protein: $2^{1}CH_3^{I}$, $12^{1}CH_3^{I}$, $18^{1}CH_3^{I}$, $18^{1}CH_3^{IV}$ (PpcD) and $12^{1}CH_3^{III}$, $18^{1}CH_3^{I}$ (PpcE). Nonetheless, these assignments were also confirmed independently from the combined analysis of 2D-^{1}H-NOESY, 2D-^{1}H-TOCSY and 2D-^{1}H-^{13}C-HSQC NMR spectra. The ^{1}H and ^{13}C chemical shifts of the heme α-substituents of PpcA homologues are listed in Table B3 (Appendix B).

3.1.2 AXIAL LIGAND GEOMETRY

The molecular orbital parameters derived from the ^{13}C chemical shifts are reported in Table 4. A schematic representation of heme geometries is indicated in Figure 12 together with the comparison between the experimental and calculated shifts. The quality of the fittings obtained clearly shows that the experimental data are well described by the model (Table 4).

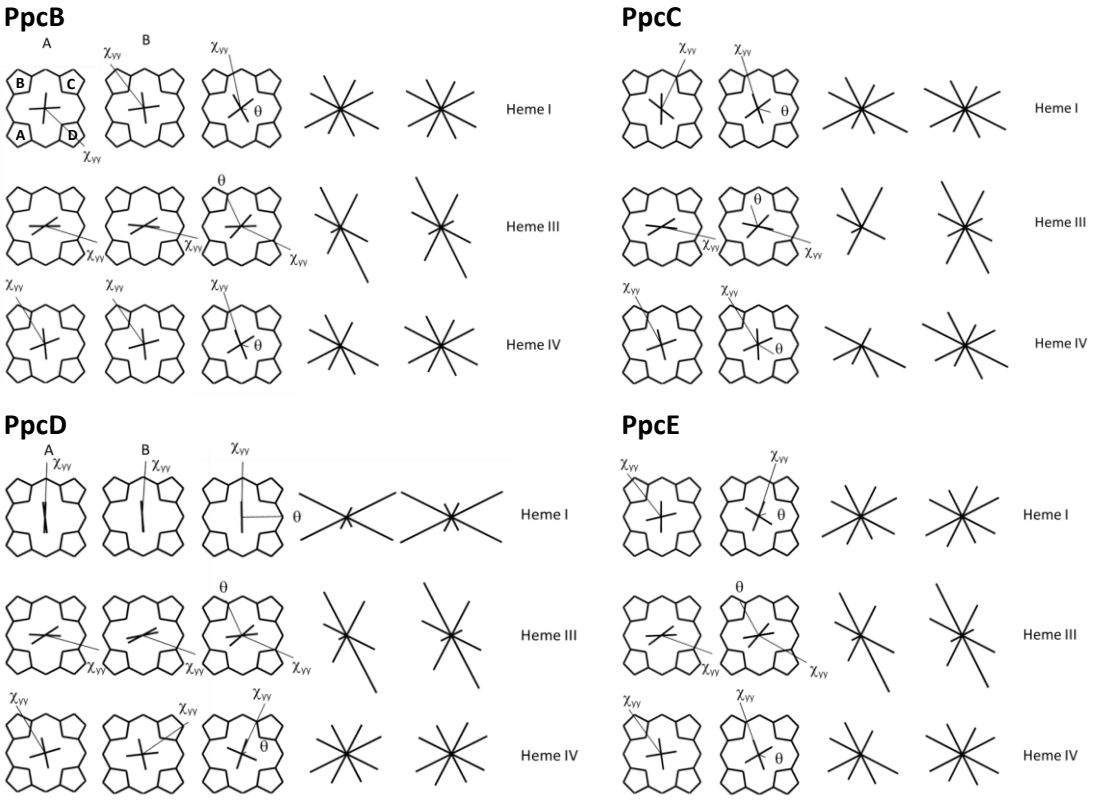

Figure 12 - Orientation of the heme axial ligands, and experimental and calculated shifts of PpcB–E heme α-substituents [58]. The orientations of the heme axial histidine planes reported in the X-ray structure are shown in the first column, (a second column for PpcB and PcpD where there are two molecules in the asymmetric unit is given). The orientation of the χ_{yy} magnetic axis deduced from the coordinates is also shown. The orientation of the axial histidine planes determined from NMR data in this work are represented in the next column together with the orientation of the rhombic perturbation and of the χ_{yy} magnetic axis for each heme. The last two columns represent the experimental and calculated ^{13}C NMR paramagnetic shifts of the heme α-substituents, respectively. Each line is oriented from the center of the heme to the respective carbon with length proportional to the paramagnetic shift. The heme pyrrole rings are identified according to the Fisher nomenclature and the heme α-substituents are identified according to the IUPAC nomenclature on the top left panel. The axes are defined relative to the N_A to N_C vector, with a positive angle for a rotation in the counter clockwise direction.

Table 4 - Comparison between the molecular orbital parameters obtained by fitting the ^{13}C signals of the heme α-substituents and the geometry of the axial ligands reported in the X-ray structure [24, 25, 59]. The values in parenthesis indicate the standard error associated with the molecular orbitals parameters fit to the experimental data assuming that the chemical shifts have an experimental uncertainty of 1ppm. The parameter β was calculated from the energy splitting of the molecular orbitals using an empirical equation [43]. PpcB and PpcD crystals have two molecules in the asymmetric unit [25].

Protein	Parameter	Heme I		Heme III		Heme IV	
		NMR	X-ray	NMR	X-ray	NMR	X-ray
PpcA	θ (°)	-70(1)	[a]	67(1)	[a]	-63(2)	[a]
	ΔE (kJ/mol)	1.35(0.05)	-	3.54(0.08)	-	0.67(0.05)	-
	β (°)	75	[a]	44	[a]	82	[a]
PpcB	θ (°)	-57(3)	87/-82	70(1)	62/58	-63(2)	-77/-79
	ΔE (kJ/mol)	0.64(0.05)	-	3.54(0.09)	-	0.89(0.06)	-
	β (°)	81	79/82	47	35/36	79	75/81
PpcC	θ (°)	-62(1)	-20	62(1)	58	-78(1)	-73
	ΔE (kJ/mol)	1.43(0.06)	-	2.43(0.07)	-	2.09(0.07)	-
	β (°)	72	52	59	38	69	86
PpcD	θ (°)	-44(1)	-43/-42	69(1)	60/65	-21 (3)	-76/10
	ΔE (kJ/mol)	4.24(0.09)	-	4.17(0.11)	-	0.52(0.06)	-
	β (°)	0	12/3	35	38/22	84	85/84
PpcE	θ (°)	-27(2)	-84	74(1)	64	-65(2)	-81
	ΔE (kJ/mol)	0.84(0.06)	-	4.18(0.12)	-	0.81(0.06)	-
	β (°)	80	77	40	34	80	89

[a]The values for the crystal structure of PpcA were not included because is structure is altered by the additive deoxycholate used in the crystallization.

The heme electronic structure and the geometry of the PpcA heme axial ligands in solution were reported previously [60] and will not be discussed. In that previous work, three temperatures (16, 25 and 30ºC) were used to calculate the heme geometries. Although a third temperature provides further precision in the determination of the ΔE values, the results are essentially unaffected when two temperatures (16 and 25ºC) are used. For comparison, the parameters obtained for PpcA in these experimental conditions were included in Table 4 together with those of the other four *Gs* triheme cytochromes.

3.2 DISCUSSION

More than 90% of the paramagnetic heme α-substituent signals were obtained for each triheme cytochrome Table B3 (Appendix B). The small fraction of unassigned signals is located in crowded spectral regions. The results reported in Table 4 show that the geometries of the heme axial histidine planes are different for the three hemes in each cytochrome. This is observed for the projection on the heme plane of the acute angle between the heme axial histidine planes (β), as well as for the orientation of those planes relative to the N_C–N_A axis of the porphyrin (θ). Figure 12 shows the geometry of the heme axial ligands of the four triheme cytochromes as determined by X-ray crystallography and by NMR. The orientation of the rhombic perturbation determined from NMR data is also represented and the length of the line is proportional to the magnitude of the orbital energy splitting between the frontier molecular orbitals with the heme becoming more axial the shorter the length. Figure 12 shows that there is good agreement for the geometries of the heme III axial ligands between the crystal and solution structures of the PpcA-E proteins. This heme shows a narrow distribution in the acute angle between the histidine planes and a θ angle close to 70º for all triheme cytochromes from *Gs* (PpcA-E). For heme IV the geometries of the axial ligands are similar in five of the six crystal structures, the exception being the monomer B of PpcD.

The histidine planes are close to perpendicular to each other and the θ angles are close to -75º. In monomer B of PpcD the acute angle between the projection of the histidine planes is different from the other structures and theta is at 10º. Incidentally, it is this structure that is more similar to that deduced from the NMR analysis. Therefore, with respect to heme IV, there is reasonable agreement between the structure deduced by NMR and X-ray data for all cases except monomer A of PpcD. With respect to heme I, good agreement between the NMR data and the crystal structures is only observed for PpcD, where both monomers of the crystal have nearly parallel axial ligands with the same orientation as deduced from the NMR data. Heme I of PpcA, B and C display a similar geometry in solution, with a β angle of ~75º between the axial histidine planes and rhombic perturbations oriented around -60º. PpcD has a more rhombic heme I with a small β angle and a θ of -44º. In PpcE, heme I is again more axial but the rhombic perturbation in solution is oriented towards -27º. In order to predict pseudocontact shifts to help in refining the solution structures of paramagnetic centers, accurate information about the paramagnetic system in solution is required. The heme axial ligand geometries allow the determination of the magnetic axis orientation, which is essential for this prediction. The fact that PpcB and PpcD present two different monomers in the crystal suggests that the c_7 cytochromes can accommodate a diversity of structures. However, the fact that a single set of resonances is observed for the oxidized state of these proteins shows that in solution all triheme cytochromes assume a single conformation. Furthermore, none of the studied proteins revealed extra broadening of the resonances which would reveal the presence of fast exchange between different conformations. The results reported here show several differences between crystal and solution structures. The largest differences are seen in heme I with poor agreement between

the geometries determined by X-ray and those determined in solution. This observation correlates with increased intrinsic flexibility of the protein around heme I as determined by backbone dynamics studies for PpcA [27]. Indeed, the polypeptide segment between His^{17} and Cys^{27} that surrounds heme I has a dynamic behavior on the μs–ms time scale.

Dynamics in this time scale have been postulated to be essential for the recognition and interaction between protein molecules. Thus, given the structural homology among the *Gs* cytochrome c_7 family, the high flexibility of the polypeptide chain around heme I together with the larger solvent exposure might explain the observation made here. Heme III has a conserved geometry for all the periplasmic triheme cytochromes from *G. sulfurreducens*, similar in solution and in the crystal, having little variation in the heme magnetic axes. This may be a consequence of the fact that this is the least exposed heme and therefore less susceptible to influence from crystal contacts [25]. For heme IV good agreement is observed with at least one of the monomers found in the crystal.

The observed differences showed that the axial ligands geometries determined in solution are crucial to define reliable pseudocontact constraints for the detailed structural characterization of *Gs* triheme cytochrome family in solution. Indeed, accurate information on the geometry of heme axial ligands is critical in the solution determination of the structure of paramagnetic heme proteins [38, 46]. This is particularly important for the heme ligands since paramagnetic relaxation makes NOE connectivities to the imidazole protons unreliable for defining the geometry of the heme pocket.

3.3 CONCLUSIONS

Analysis of the 1D-^{1}H NMR spectra obtained for the family of five c_7 triheme periplasmic cytochromes from *G. sulfurreducens* in the oxidized state, shows structural differences, mostly among the heme axial ligand geometry. Structural characterization of the relative orientation of the axial ligands of these proteins by ^{13}C-paramagnetic NMR was carried out. The comparison of the NMR data obtained in this work and the crystal structures, showed that for some hemes significant differences exist between the two methods. Indeed, the orientation of the magnetic axes obtained from NMR data and the orientation taken from the X-ray coordinates differ indicating that the available crystal structure should be carefully used in detailed functional-structural correlation studies. The determination of the structures of these proteins in solution should also be equated.

The present results will be used to generate paramagnetic constraints to include in the future refinement of the *Gs* triheme cytochrome family solution structures in the oxidized state. This will allow the confident comparison with structures obtained both in the oxidized state but at different conditions of solution pH, and also with structures obtained for the reduced state. Such a comparison will be the first to establish the molecular bases for the functional differences among the members of a cytochrome family that coexist in the same organism.

The results allowed the orientation of the magnetic axes to be defined confidently with respect to the heme frame in solution, a necessary step for the use of paramagnetic constraints to improve the complete solution structure of these proteins.

4. Study of the conserved residue Phe[15] in the cytochrome c_7 family[2]

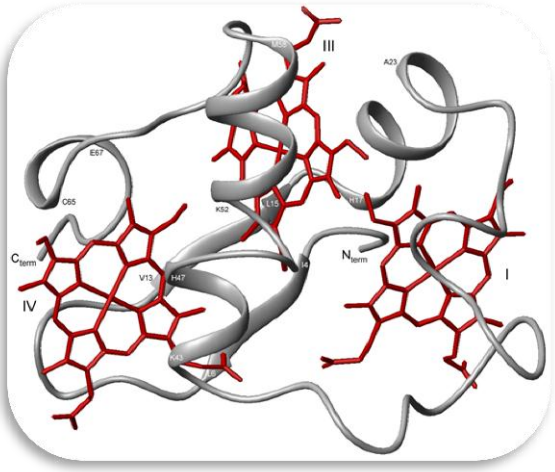

[2] Partially reproduced from JM Dantas, L Morgado, YY Londer, AP Fernandes, RO Louro, PR Pokkuluri, M Schiffer, CA Salgueiro (2012) Pivotal role of the strictly conserved aromatic residue F15 in the cytochrome c_7 family, J Biol Inorg Chem 17, 11-24 (http://dx.doi.org/10.1007/s00775-011-0821-8), according to the Editors' Copyright Policy.

4. Study of the conserved residue Phe[15] in the cytochrome c_7 family

The selective replacement of specific amino acids by site-directed mutagenesis together with the functional and structural characterization of mutated proteins is expected to provide insights into their functional role. Protein residues that are critical for structure and function of the proteins are expected to be conserved throughout evolution. In the c_7 cytochrome family, the residues of the CXXCH binding motif are strictly conserved, due to its importance in the correct heme binding to the protein (see Figure 2). Examining the nature of amino acid side chain of the nine conserved residues remaining, only one is an aromatic residue (phenylalanine 15). Indeed, the amino acid phenylalanine 15 (Phe^{15}) located in the hydrophobic core between heme I and III, displays a particular structural arrangement, which is also observed in tetraheme cytochromes c_3 [61] as well as in cytochrome c_7-type domains [62]. Therefore, the nature of this amino acid side chain and its particular spatial location might have an important structural/functional role within these proteins. In PpcA, the aromatic ring of the residue Phe^{15} is almost parallel to the ring plane of heme I and perpendicular to the one of heme III. The imidazole ring of the heme III axial histidine (His^{20}) is parallel to the Phe^{15} ring. This rearrangement immobilizes the Phe^{15} ring, preventing its free rotation, keeping a conserved orientation within this structural motif. In a previous work, the Phe^{15} residue was replaced by the aromatic tryptophan and tyrosine residues using site-directed mutagenesis and their effect on the global (macroscopic) redox properties of PpcA was evaluated [61]. However, the severe broadness of the NMR signals in tyrosine and tryptophan mutants prevented the study of the individual heme redox properties [63].

To probe the structural and functional roles of Phe^{15}, this residue was further replaced by the aliphatic hydrophobic amino acid leucine (PpcAF15L). The redox properties of this mutated protein were determined in the same experimental conditions using visible and NMR techniques and compared with those obtained for the wild-type. These studies revealed that the reduction potentials and redox-Bohr interactions of PpcAF15L are smaller than the ones observed for the wild-type protein. The changes in redox parameters promote the elimination of the concerted e^-/H^+ transfer step that was observed for PpcA. In this Thesis, we aimed to structurally rationalize these observations, monitoring the pH-dependent conformational changes and comparing the solution structures of PpcAF15L and PpcA. The solution structure of PpcAF15L determined in this work, revealed key structural-functional features associated with residue Phe^{15} and its concomitant role in the regulation of the wild-type functional mechanism.

4.1 RESULTS

4.1.1 PURIFICATION OF ^{15}N-LABELLED AND UNLABELLED PPCAF15L MUTANT

After the expression of the ^{15}N-labelled and unlabelled PpcAF15L the proteins were purified by cation exchange chromatography and molecular exclusion chromatography. Since the elution profiles obtained for ^{15}N-labelled and unlabelled PpcAF15L were similar, the results obtained during the purification process are illustrated by the ones obtained for the ^{15}N-labelled mutant (Figure 13). All the remaining data are present in the Appendix (FiguresA1-A2).

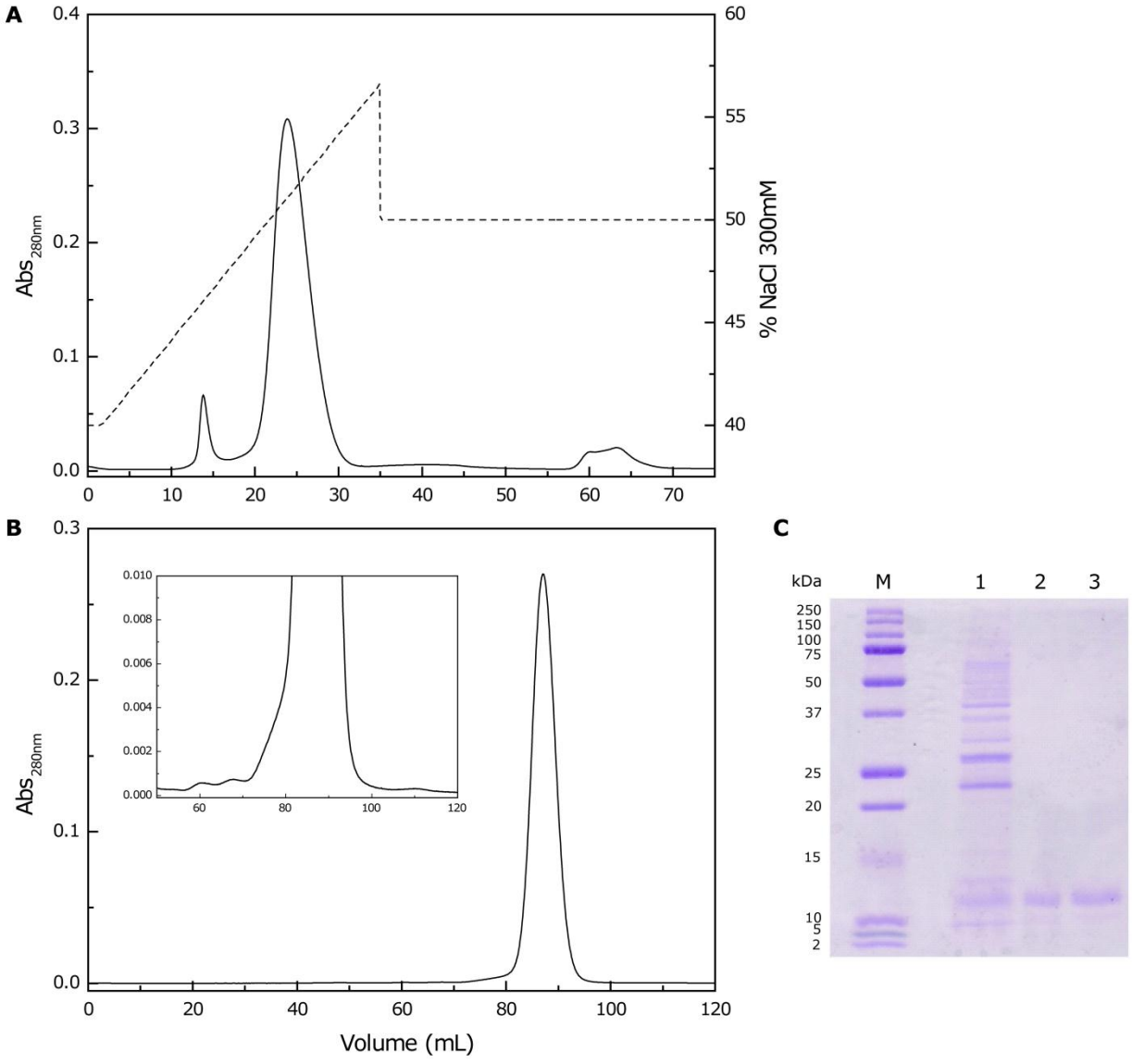

Figure 13 – **Purification of ^{15}N-labelled PpcAF15L**. (A) Elution profile for the cation exchange column chromatography equilibrated with 10mM Tris-HCl, pH 8.5 and eluted at a flow rate of 1mL/min. Primary and second *y*-axis, report the variation of absorbance at 280 nm (solid line) and the NaCl gradient profile (dashed line), respectively. (B) Elution profile for the molecular exclusion column chromatography equilibrated with 100mM sodium phosphate buffer, pH 8. The inset shows an expanded view of the chromatogram (C) Purity analysis by SDS-PAGE. Lane M: prestained protein marker; lane 1: periplasmic fraction; lane 2: after purification by cation exchange chromatography; lane 3: after purification by molecular exclusion chromatography. The MW of the protein markers are indicated on the left.

After isolation of the periplasmic fraction, a cation exchange chromatography step was performed (Figure 13A). The only difference between the wild-type and mutated protein is the substitution of residue phenylalanine by a leucine, which are both residues without ionizable side chains. For this reason, the isoelectric point is the same for both proteins. The isoelectric point determined for PpcA was 9.44 [10]. Thus, as the mutant is a very basic protein, it strongly binds to the cation exchange column equilibrated with 10mM Tris-HCl (pH 8.5). The bound protein is then eluted with a sodium chloride gradient (120-180mM). As can be observed in the Figure 13A, the protein of interest was eluted at 51% of NaCl 300mM.

With this purification step the majority of the contaminants were removed. Despite highly efficient, this chromatographic step needs to be complemented with a molecular exclusion chromatographic step. In Figure 13B is depicted the elution profile of the molecular exclusion chromatogram for the PpcA mutant. The molecular weight of PpcaF15L is 9.54kDa (theoretical value determined with *Compute pI/Mw tool* [64]) and was eluted at 87mL, with 100mM sodium phosphate buffer, pH 8 (Figure 13B). Along the purification steps the purity of the protein was evaluated by SDS-PAGE and one intense band was obtained in the expected MW region (~10kDa), after the final purification step (Figure 13C).

Protein yields were determined by UV-visible spectroscopy using the PpcA extinction absorption coefficient of the α band characteristic of the protein reduced form (ε_{552nm} = 97.5$mM^{-1}cm^{-1}$ [65]). The yields obtained for ^{15}N-labelled and unlabelled PpcAF15L were 1 and 1.6 mg per litre of cell culture, respectively.

4.1.2 SEQUENTIAL ASSIGNMENT, RESTRAINTS AND STRUCTURE CALCULATION OF PPCAF15L

The backbone, side chains and heme substituents NMR signals of PpcAF15L were assigned following the same methodology used for the wild-type protein [27]. To avoid overlap with polypeptide amide protons, the heme signals were assigned in the NMR spectra acquired for PpcAF15L samples prepared in ^2H_2O, according to the strategy described in section 2.4.1. After that, individual spin-systems were firstly identified in the NMR spectra acquired in H_2O, according to their type, and then sequence-specific assigned. A summary of the sequential connectivities between NH, Hα and Hβ protons is shown in Figure 14.

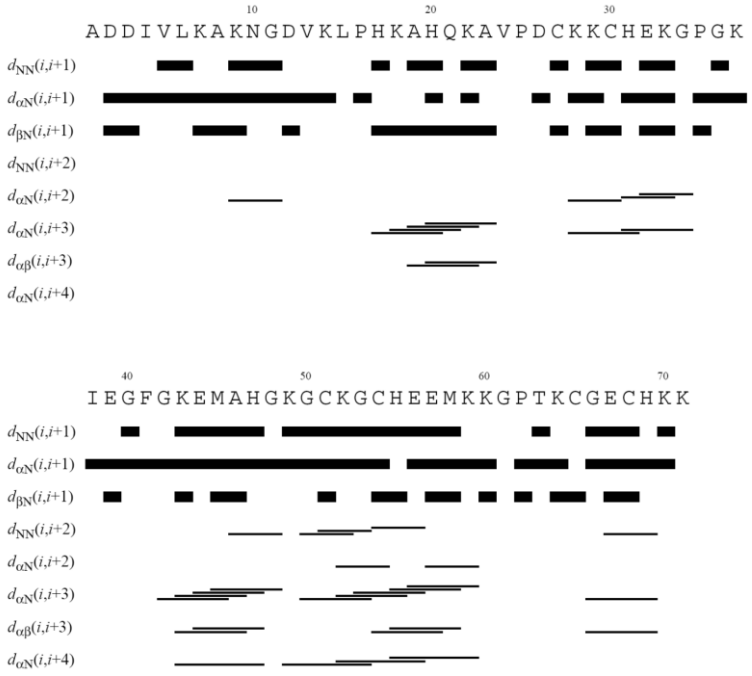

Figure 14 - Sequential NOE connectivities involving NH, Hα and Hβ observed in the 2D-^{1}H-NOESY spectrum for reduced PpcAF15L. The line thickness is indicative of the NOE intensity.

The total extent of the assignment for PpcAF15L is 88%, excluding carboxyl, amino and hydroxyl groups. The assigned cross-peaks in the 2D-^{1}H-NOESY spectrum were integrated and converted into volume restraints, resulting in 806 lov (lower limits for volumes) and 1016 upv (upper limits for volumes) (Table 5).

Table 5 - Summary of restraint violations and quality analysis for the final family of solution structures for PpcAF15L.

Parameter	
Type of distance restraint	
Intra-residue	704
Sequential	365
Medium range ($2 \leq \|i - j\| < 5$)	300
Long range ($\|i - j\| \geq 5$)	453
Total	1822
	(806 lov +1016 upv)
Upper distance limit violations	
Average maximum	0.26 ± 0.05
Number of consistent violations (>0.2Å)	0
Lower distance limit violations	
Average maximum	0.27 ± 0.04
Number of consistent violations (>0.2Å)	0
Van der Waals violations	
Average maximum	0.19 ± 0.02
Number of consistent violations (>0.2Å)	0
Ramachandran Plot (%) [a]	
Most favoured regions	62.6
Additionally allowed regions	35.2
Generously allowed regions	2.2
Disallowed regions	0.0
Stereospecific Assignments [b]	34
Precision	
Average pairwise rmsd backbone (Å)	0.36 ± 0.12
Average pairwise rmsd heavy atoms (Å)	1.14 ± 0.10

[a] Values obtained with PROCHECK-NMR
[b] Analysis with GLOMSA

These were used as input for the program PARADYANA [66] together with a set of 69 fixed upper limit distances. The preliminary structures were analyzed using the program GLOMSA [67], modified to take NOE volumes as input, and 34 stereo-specific assignments were made for diastereotopic pairs of protons or methyl groups. The effect of spin diffusion introduces an uncertainty into the conversion of experimental data into distance restraints. This effect was simulated by complete relaxation matrix calculations based on the initial protein structures and, accordingly, a parameter was set in the program PARADYANA to loosen all distance restraints by 5%. An average of 25 NOE restraints per amino acid residue (11 lovs and 14 upvs) and 122 per heme residue (54 lovs and 68 upvs) was used for the final calculation (Figure 15). The distribution of the number of restraints is not uniform along the protein sequence, as heme groups attached to positions 30, 54 and 68 show many long-distance contacts, a feature also present in the wild-type protein [27].

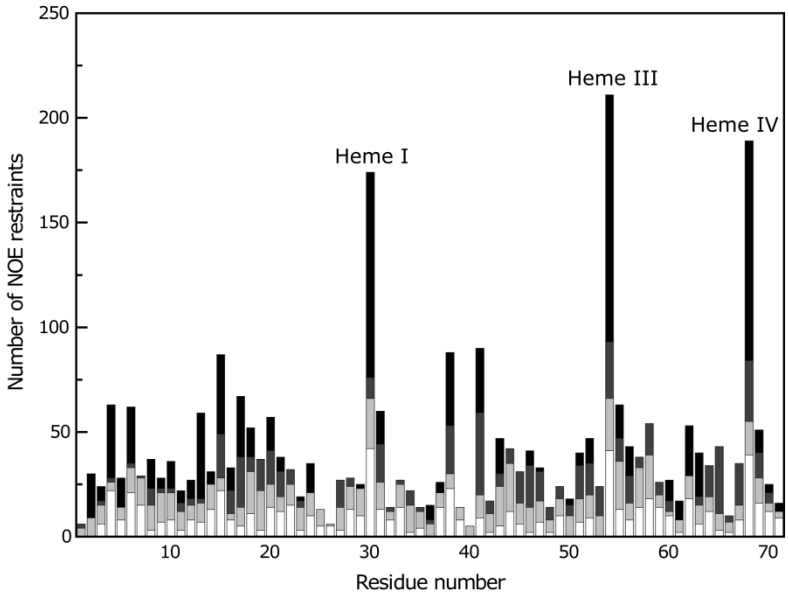

Figure 15 - Number of NOE restraints per residue used for the calculation of the structure of PpcAF15L. Bars are white, light gray, dark gray and black for intra residue, sequential, medium and long range restraints, respectively. Residues 30, 54 and 68 also include restraints to hemes I, III and IV, respectively.

4.1.3 Quality analysis of the structures

The final family consists of 20 structures (Figure 16A) with the lowest target function values (from 2.36 to 2.65 Å^2, average value 2.56 Å^2, 12% range from the lowest value).

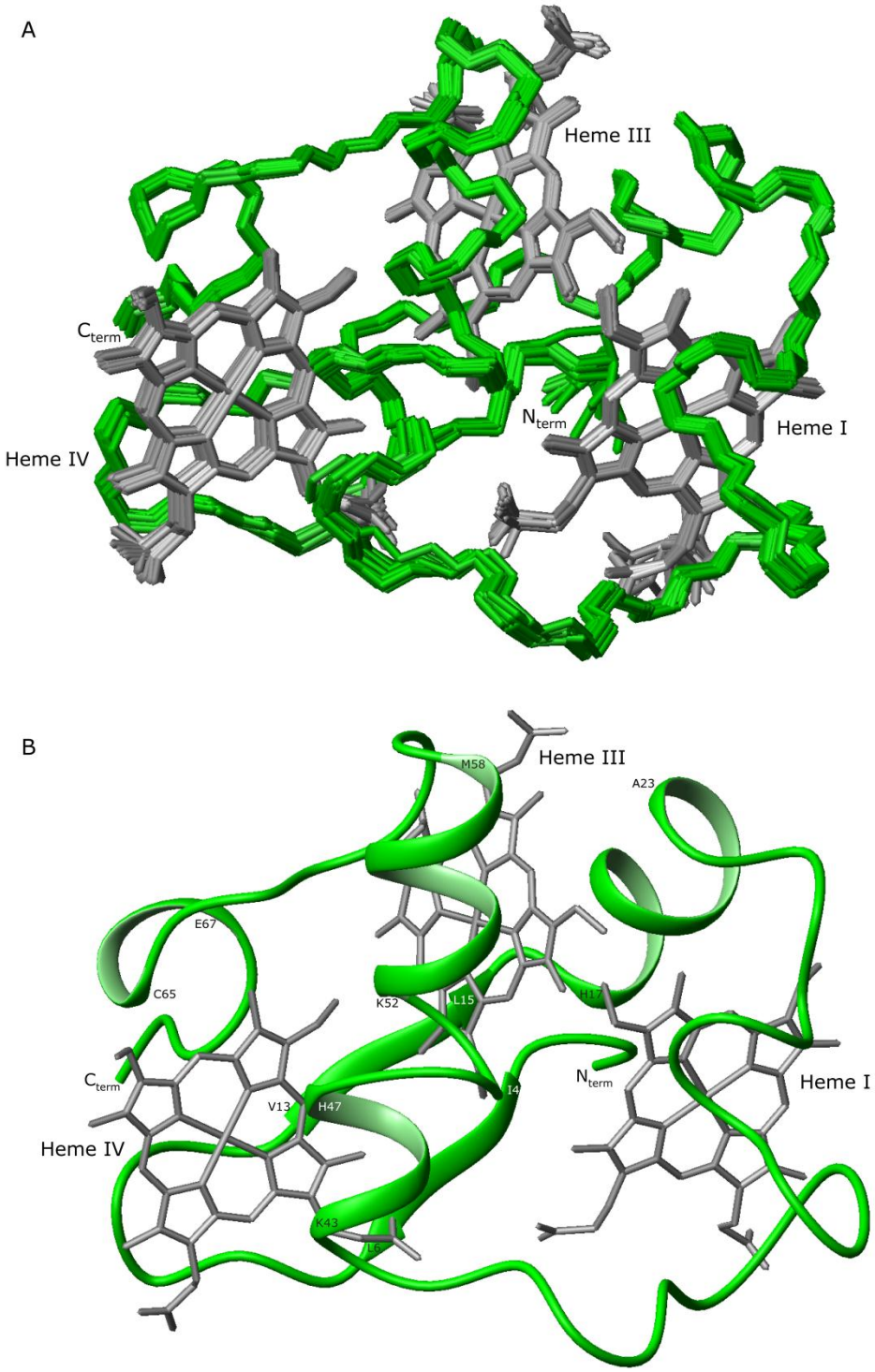

Figure 16 - PpcAF15L solution structure. (A) Overlay of the 20 lowest energy NMR solution structures of PpcAF15L at pH 7.1. Superimposition was performed using all the heavy-atoms. The peptide chain and the hemes are colored green and gray, respectively. (B) Ribbon diagram of PpcAF15L structure. Figures were produced using MOLMOL [50].

The structures superimpose with an average pairwise backbone (N-Cα-C') rmsd of 0.36 Å and a heavy atom rmsd of 1.14 Å (Figure 17).

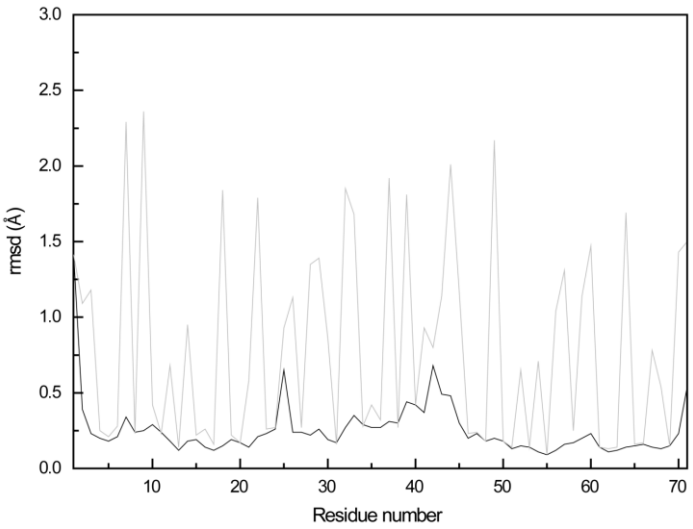

Figure 17 - Average pairwise backbone (black) and heavy atom (gray) rmsd values per residue of the family of 20 conformers obtained for PpcAF15L solution structure.

Thus, the backbone is well defined and the amino acid side chains showing larger conformational variability correspond to regions with higher solvent exposure. In particular, the N- and the C-terminals are disordered. The statistics for this family of structures are shown in Table 5. The Ramachandran plot shows 62.6% of the residues in the most favored regions, 37.4% in the allowed regions (Figure 18). A total of 35 hydrogen bonds were identified in the family of 20 structures with the program MOLMOL [50], 23 of which were present in at least 50% of the structures.

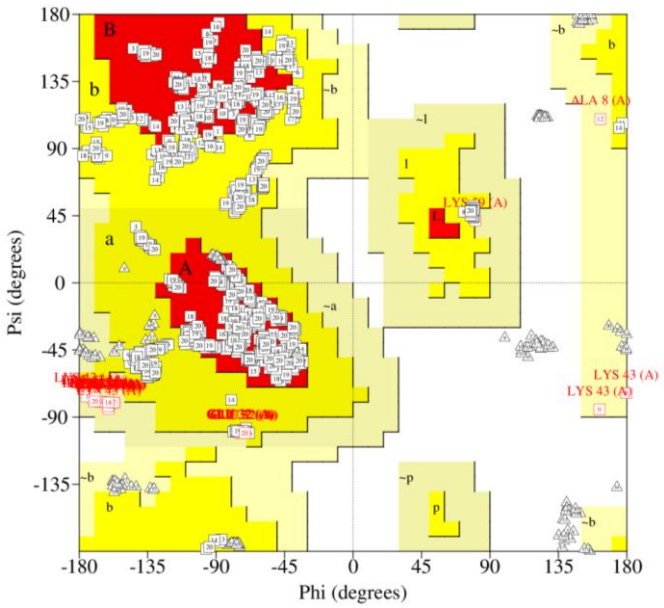

Figure 18 - Ramachandran plot for the ensemble of the best 20 conformers obtained for PpcAF15L solution structure. Residues in most favoured regions (A, B, L); additional allowed regions (a,b,l,p), generously allowed regions (~a, ~b, ~l, ~p) and disallowed regions.

4.1.4 pH TITRATION

The pH titration of PpcAF15L was carried out by ^{1}H-^{15}N HSQC NMR in the pH range 5.4-9.5 and all ^{1}H and ^{15}N chemical shifts of the polypeptide backbone (except for residues 1 and 2) and side chains were measured. To estimate the effects of pH changes on the PpcAF15L solution structure, the average chemical shift differences of each amide signal ($\Delta\delta_{avg}$) were calculated as described by Garret and co-workers [39]. The residues whose NH signals showed larger differences were from Lys[7], Ala[8], Asn[10], Ile[38] backbone and also from Asn[10] and Gln[21] side chains (Figure 19A). The pH titration of these signals for Lys[7], Ala[8], Asn[10], Gln[21] and Ile[38] are shown in Figure 19B. The NH signals of Lys[7], Ala[8], Asn[10] and Gln[21] have basic pK_a values of 7.6, 7.7, 7.6 and 8.2 respectively, whereas Ile[38] has a much more acidic pK_a (5.2).

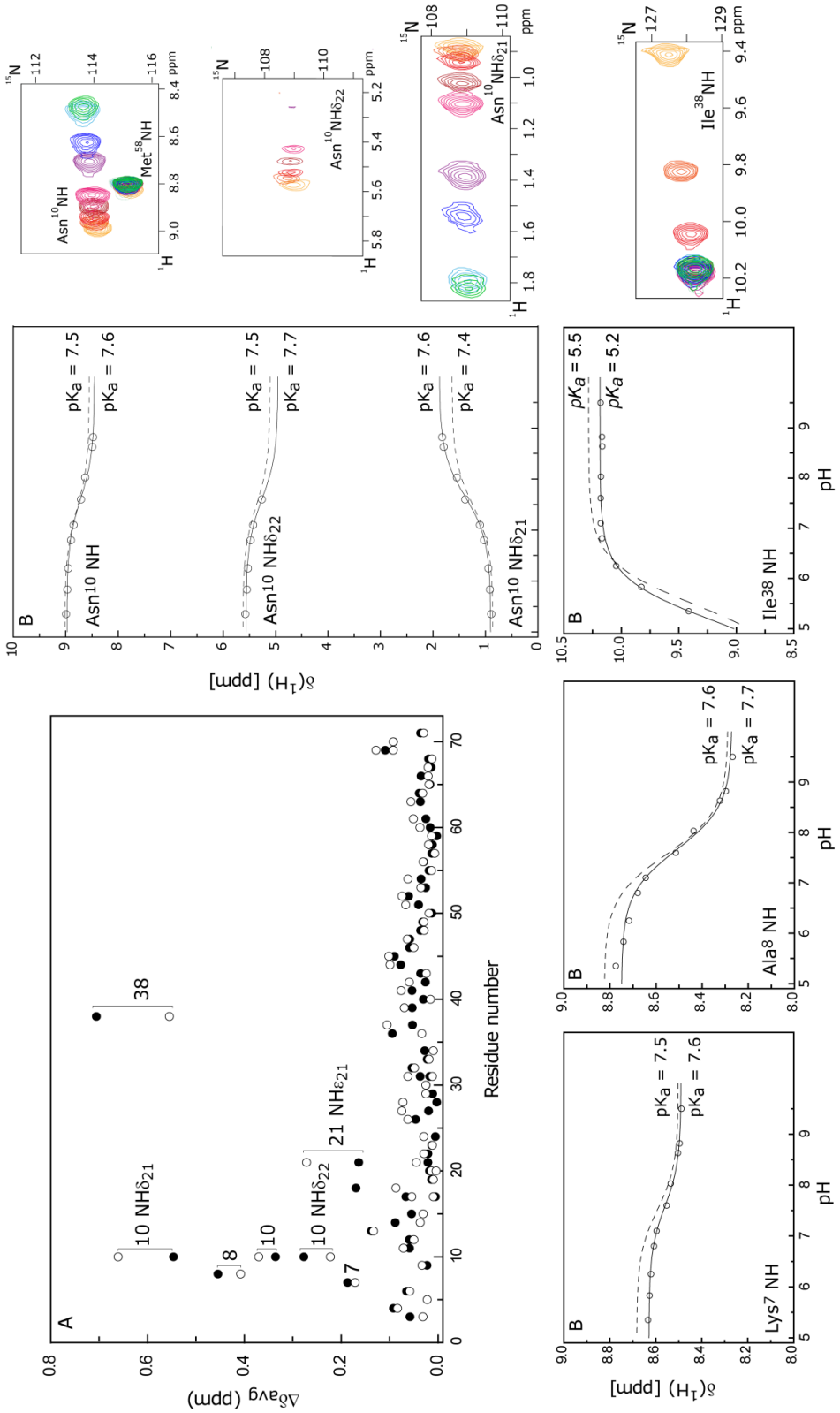

Figure 19 - Comparison of pH-linked conformational changes in PpcAF15L (open circles) and PpcA (closed circles). (A) Weighted average of ^{1}H and ^{15}N chemical shifts ($\Delta\delta_{avg}$) between pH 5.4 and 9.5. (B) pH titration data of the most affected PpcAF15L amide signals. The dashed lines in each panel represent the best fit for the wild-type protein. In the expansion of each ^{1}H-^{15}N-HSQC NMR spectrum pH increases from yellow to green. Lys^{7} and Ala^{8} backbone amide signals are not shown since they appear in a very crowded region of the spectra.

4.2 DISCUSSION

The mutant PpcAF15L showed the same set of interheme NOE connectivities between heme substituents of the closest heme groups as the ones observed in the wild-type cytochrome (Table B1 and B2 Appendix), which indicates that the mutation did not affect significantly the heme core architecture. Thus, the heme core architecture is conserved in both proteins. Comparison of the heme proton chemical shifts (Figure 20) shows that the most affected signal is the thioether proton $3^2CH_3^{III}$ due to the additional ring-current effects from Phe[15] aromatic ring, which is not present in PpcAF15L.

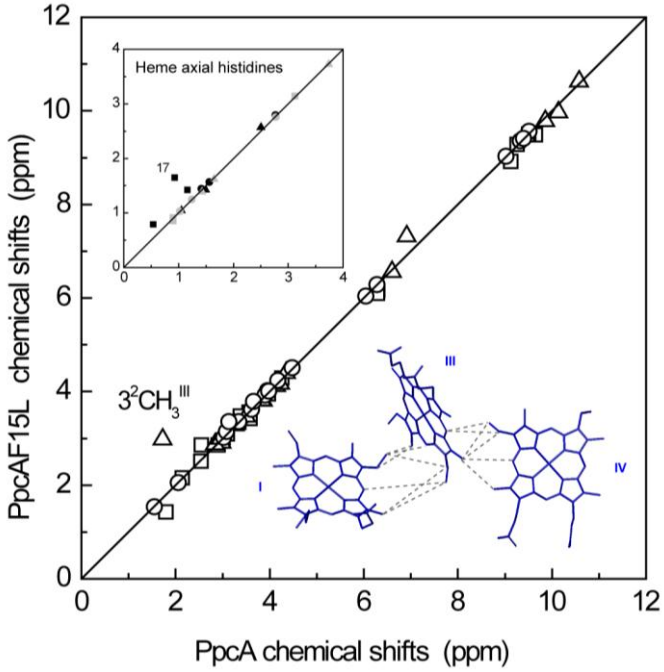

Figure 20 – Comparison of the observed heme proton chemical shifts of reduced PpcAF15L (this work) and those of PpcA [24] at pH 7.1 and 16ºC. Squares, triangles, and circles correspond to hemes I, III, and IV, respectively. Comparison of the αCH and βCH_2 proton chemical shifts of the heme axial histidines is indicated in the inset. Gray symbols and black symbols correspond to the heme proximal and distal histidines, respectively. The solid lines have a unit slope. The root mean square deviation between the chemical shifts measured for PpcAF15L and those of PpcA are 0.20 (heme I), 0.27 (heme III), and 0.06 (heme IV). The interheme nuclear Overhauser effect conectivities are indicated by dashed lines in the inset.

The comparable dispersion of signals in the ^1H-^{15}N HSQC NMR spectra obtained for PpcAF15L and wild-type proteins (Figure 21) indicates that the overall fold is maintained. However, several signals are significantly affected, namely the backbone NH signals of Ile[4], Val[5] and the segment formed by residues His[17]-Val[24] (see inset in Figure 21). The amide signal of His[17] is the most shifted followed by that of His[20]. The backbone NH signals of residues Asp[26]-Lys[28], Gly[36]-Lys[37], Ala[46] and Gly[53] are affected to smaller extent. The polypeptide sequence of both proteins contains one asparagine (Asn[10]), one glutamine (Gln[21]) and six axial histidines ($His^{17(I)}$, $His^{20(III)}$, $His^{31(I)}$, $His^{47(IV)}$, $His^{55(III)}$ and $His^{69(IV)}$), which have an additional amide or imide group in their side chains. Inspection of these signals in the ^1H-^{15}N HSQC NMR spectra showed that the signals of Gln[21] and heme III axial histidine ($His^{20(III)}$) are the most affected followed by those of $His^{47(IV)}$ and $His^{55(III)}$.

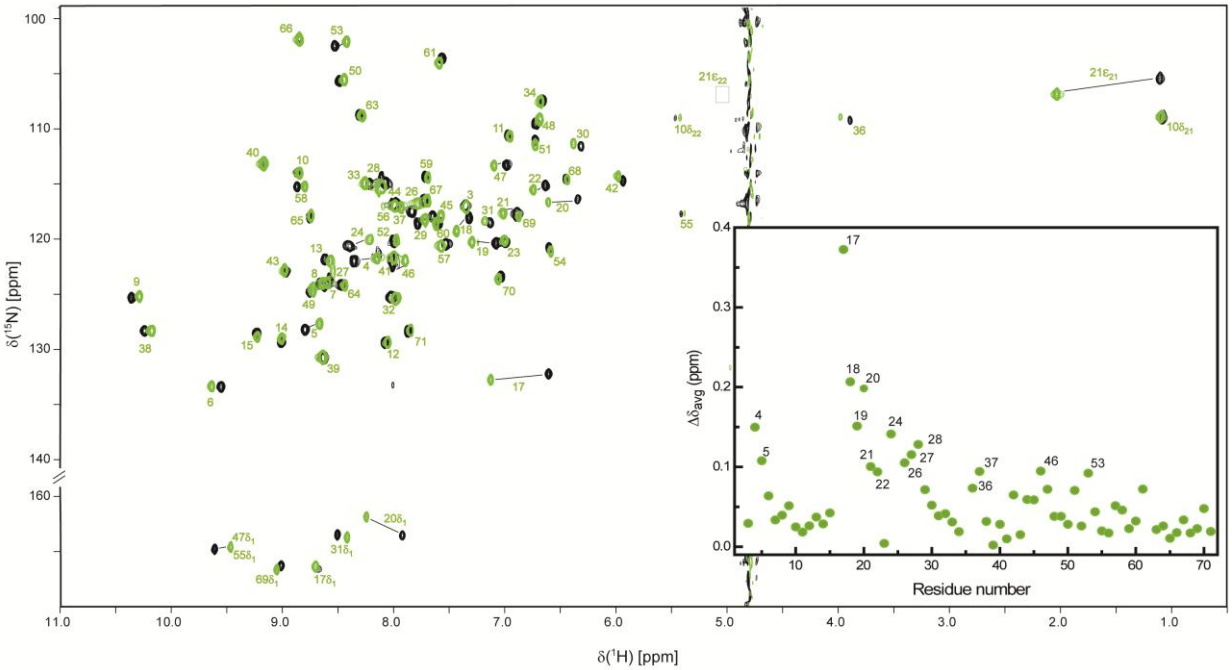

Figure 21 - 2D-^{1}H-^{15}N HSQC NMR spectra of fully reduced PpcAF15L (green contours) and PpcA (black contours). The most affected signals are connected by a straight line in the spectrum. On the inset is represented the weighted average of ^{1}H and ^{15}N chemical shifts ($\Delta\delta_{avg}$) of each backbone amide.

The number of residues per heme group in PpcAF15L is approximately 23 and, consequently, several nuclei are located in close proximity of the hemes. Since the heme groups are diamagnetic in the reduced state, the observed chemical shifts of those signals might have large contribution from the heme(s) ring-current effect. Therefore, some signals might show significant changes in their chemical shifts even in presence of marginal structural rearrangements. Thus, to proper rationalize the changes observed in the redox properties and concomitant functional mechanism of PpcAF15L, it is essential to determine the solution structure of this mutant.

4.2.1 Comparison of PpcAF15L and PpcA solution structures

In solution, the structure of the triheme cytochrome PpcAF15L folds in a two-strand antiparallel β-sheet at the N-terminus formed by Ile^{4}-Leu^{6} and Val^{13}-Leu^{15}, followed by three α-helices between residues His^{17}-Ala^{23}, Glu^{44}-His^{47} and Lys^{52}-Met^{58} and a 3_{10}-helice segment formed between residues Cys^{65}-Glu^{67}. The comparison between the lowest-energy NMR structures of PpcAF15L and PpcA (Figure 22) showed that the global rmsd values are 1.08 Å for backbone atoms.

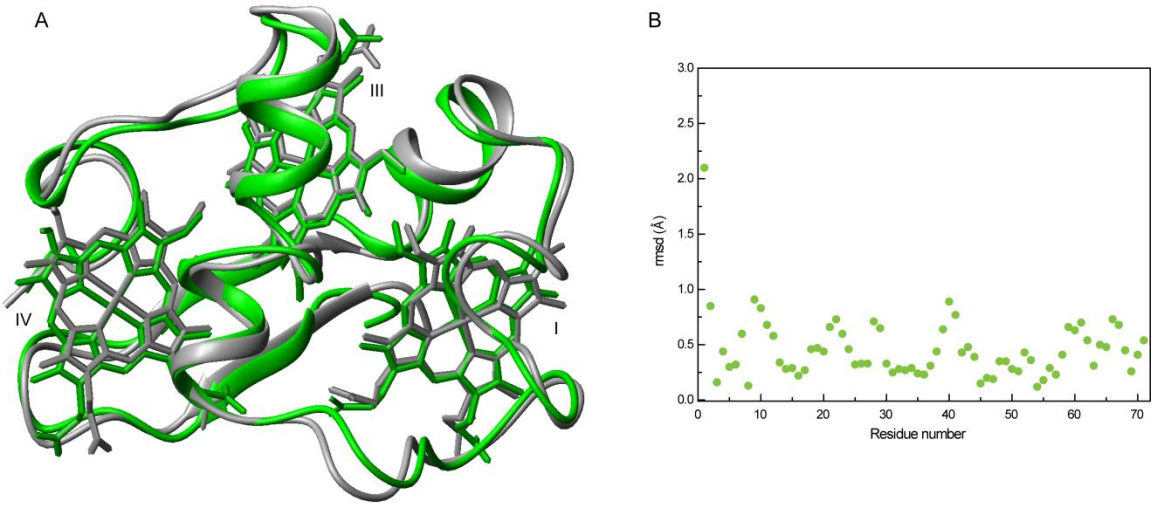

Figure 22 - Comparison of PpcAF15L and PpcA lowest energy solution structures. Structures were superimposed in MOLMOL [50] using backbone atoms. (A) PpcAF15L *versus* PpcA solution structure. PpcAF15L and PpcA structures are colored green and gray, respectively. (B) Average rmsd between each pair of structures.

Compared with the wild-type, the global fold of the mutated protein is maintained, though local rearrangements of polypeptide chain are observed. The most affected regions contain the residues showing larger variation on chemical shifts compared to the wild-type (Figure 22). The solution structure of PpcA folds in a two-strand antiparallel β-sheet at the N-terminus formed by Asp[3]-Leu[6] and Val[13]-Pro[16], followed by three α-helices between residues Ala[19]-Lys[22], Lys[43]-His[47] and Lys[52]-Met[58] [27]. Residues Ile[4] and Val[5] are opposite to residue Phe[15] in the two-stranded antiparallel β-sheets at the N-terminus. The structural rearrangements in residues Ile[4] and Val[5] caused by the replacement of Phe[15] by a leucine, perturbed the network of NOE connectivities and, probably explain why this region is affected in the mutant. Another region showing important structural rearrangements is the α-helice segment, located between hemes I and III. The α-helice is formed by residues His[17]-Ala[23], whereas in the wild-type it comprises residues Ala[19]-Lys[22]. Finally, a 3_{10}-helice segment is formed between residues Cys[65]-Glu[67] in the mutant.

The parameters describing the heme geometry of PpcAF15L in solution are presented in Table 6.

Table 6 - Heme geometry for PpcAF15L (this work) and PpcA [27] cytochromes in solution. The values for both proteins were obtained from the lowest-energy structure.

	PpcA	PpcAF15L
Heme Fe-Fe distance (Å)		
I-III	11.7	11.4
I-IV	19.0	18.9
III-IV	12.6	12.7
Angle between heme planes (°)		
I-III	82	78
I-IV	27	12
III-IV	74	71
Angle between His planes (°)		
I	50	80
III	23	50
IV	80	52

Compared to the wild-type, the geometry of the heme core in both proteins is nearly conserved in the mutant. The iron-iron distances determined among the two structures are similar, differing by less than 0.03%. In addition, hemes I and IV are parallel to each other, though slightly more in the mutant and nearly perpendicular to heme III. Finally, the heme axial ligand geometry is different for the three hemes in the mutant, highlighting one important structural role played by conserved residue Phe^{15} in preserving the axial heme geometry in the wild-type protein.

4.2.2 Heme reduction potentials and redox interactions

As mentioned, the detailed characterization of the redox properties of PpcAF15L and PpcA were previously reported and are summarized in Table 7. The solution structure determined in the presented work allowed addressing the structural basis for the differences in the redox properties of PpcAF15L and PpcA. As for the wild-type, in the mutant the heme reduction potentials are modulated by redox interactions (Table 7).

Table 7 - Heme reduction potentials and pairwise interactions (mV) of the fully reduced and protonated forms of PpcAF15L [63] and PpcA [30].

	Heme redox potentials			**Redox interactions**			**Redox-Bohr interactions**		
	I	III	IV	I-III	I-IV	III-IV	I-H	III-H	IV-H
PpcAF15L	-164	-168	-136	24	14	36	-20	-17	-49
PpcA	-154	-138	-125	27	16	41	-32	-31	-58

The positive values obtained for the redox interactions suggest that they are dominated by electrostatic effects. This is confirmed by the fact that the highest (36 mV) and the lowest (14 mV) redox interaction are observed between the closest (III-IV) and furthest (I-IV) pairs of heme groups. Thus, the similarity of the redox interactions in the two proteins correlates with the conserved heme iron-iron distances (Table 7) and with the similar distribution of charged residues in the proteins.

In contrast, the heme reduction potentials are more affected, being more negative in the mutant, particularly in heme III. As verified in the wild-type, negative heme reduction potentials are expected for relatively exposed *c*-type hemes with bis-histidine axial coordination. In the lowest energy structure, the heme exposures are 253.2 Å^2 (231.7 Å^2 for PpcA), 168.1 Å^2 (215.8 Å^2) and 207.8 Å^2 (171.3 Å^2) for hemes I, III and IV respectively. In contrast with heme III, the slightly higher solvent exposure of hemes I and IV in the mutant correlate with the smaller values of their reduction potential. The higher reduction potential of heme IV is also reinforced by its substantial positive environment due to the presence of several neighboring lysine residues that stabilize the reduced state of heme IV. Additionally, for all heme groups the angles between the axial histidine ring planes varies by approximately 30º (Table 6 and Figure 23), which are expected to contribute to the modulation of heme reduction potentials.

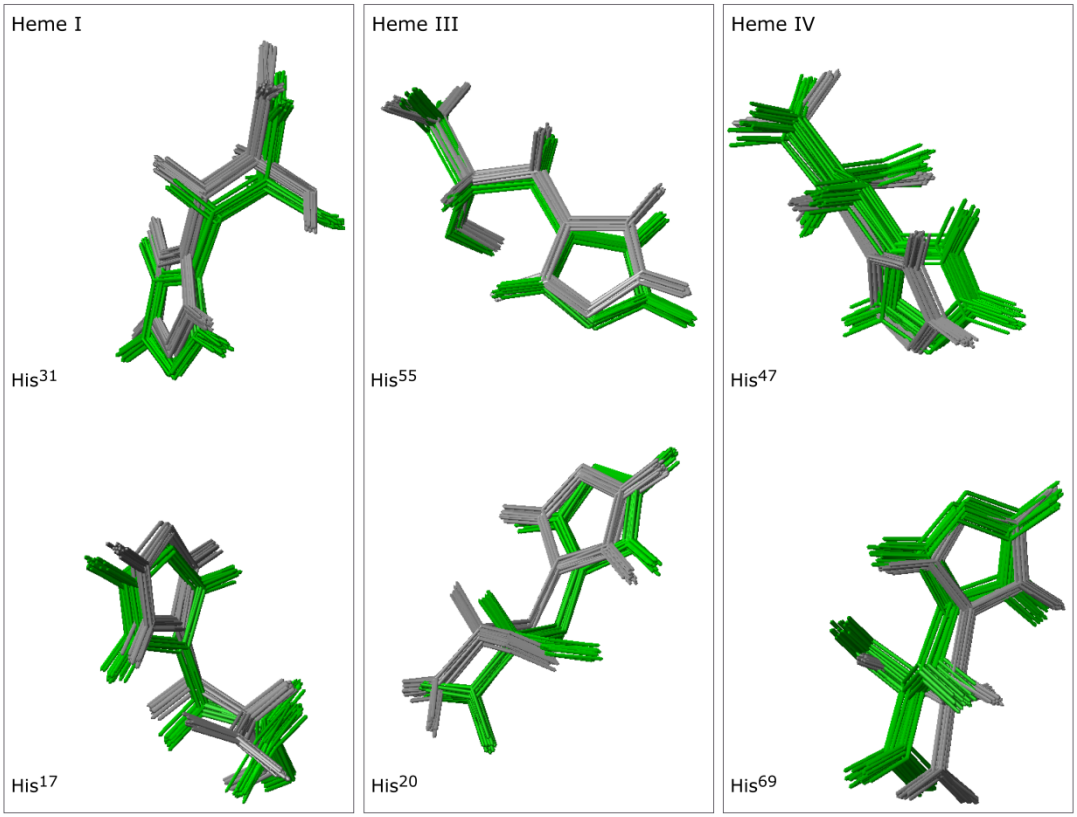

Figure 23 - Orientation of the axial histidines in each heme group for PpcAF15L (green) and PpcA (gray) solution structures. Structures were superimposed in MOLMOL [50] using backbone atoms. The axial histidines orientations taken from all the 20 structures are presented to show the geometry consensus amongst the entire family of structures.

In fact, detailed structural and electrochemical studies performed in cytochrome b_5 by Sarma and co-workers [68, 69] showed that the orientation of axial ligand ring planes slightly modulates the reduction potentials of bis-imidazole axially ligated heme proteins.

However, compared to hemes I and IV, the reduction potential of heme III is more affected and other factors different from the geometry of the axial ligands and heme solvent exposure are likely to explain this variation. One possible contribution resides in local rearrangements in the first α-helice, which is longer in the mutant (Ala^{19}-Lys^{22} in the wild-type *versus* His^{17}-Ala^{23} in the mutant). This α-helice covers one side of heme III and comprises two positive charges (Lys^{18} and Lys^{22}) whose proximity to heme III is likely to affect its reduction potential by slight reorientations toward the solvent. Unfortunately the side chains of these residues are disordered in both proteins and cannot be used to confirm this hypothesis.

In addition, the α-helice also includes the axial ligands of hemes I and III (His$^{17(I)}$ and His$^{20(III)}$, respectively) and the residue Gln^{21}, which showed considerable variations on their chemical shifts (Figure 24). The ring of axial ligands His$^{17(I)}$ and His$^{20(III)}$ together with the aromatic ring of residue Phe^{15} form one part of the hydrophobic region in the proximity of heme III (Figure 24A).

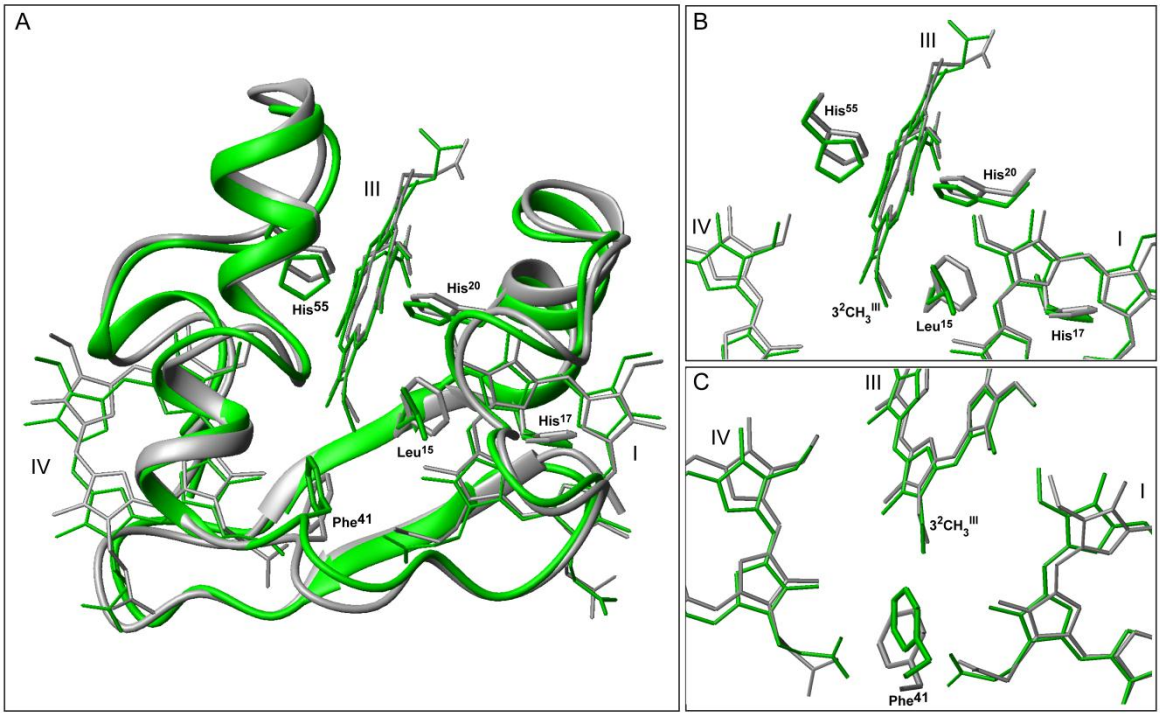

Figure 24 - Comparison of PpcAF15L (green) and PpcA (gray) lowest energy solution structures. Structures were superimposed in MOLMOL [50] using backbone atoms. (A) General overview of the heme core in which heme III is embedded, (B) Heme core region containing the side chains of residues Phe^{15}, His$^{17(I)}$ and His$^{20(III)}$, (C) Heme core region containing side chain of residue Phe^{41}.

The solution structure of the mutant shows that the side chain of residue Leu[15] is located in an equivalent position (Figure 24B). Thus, the replacement for the aromatic ring by the aliphatic side chain removes the aromatic-aromatic interaction between Phe[15] and heme III and, so influences the heme redox properties.

Finally, the aromatic ring of Phe[41], at the bottom of the cleft bellow heme III (Figure 24C), is rotated by approximately 30°. Overall, these important structural rearrangements in the hydrophobic region in the vicinity of heme III alter the nature of the aromatic interactions, thus affecting the reduction potential of the heme group.

4.2.3 Structural mapping of the redox-Bohr center

In addition to the redox interactions, the heme reduction potentials are also modulated by the solution pH (Table 7). This modulation, known as redox-Bohr effect, constitutes a crucial property for the functional mechanism of PpcA, in which coupling of electron and proton transfer is achieved at physiological pH. The detailed thermodynamic characterization of PpcA showed that such coupling involves the two microstates P_{1H} (protonated microstate with heme I oxidized) and P_{14} (deprotonated microstate with hemes I and IV oxidized) [30]. Thus, a fraction of the energy associated with electrons received from the donor by microstate P_{1H} is used by the protein to lower the pK_a value of the redox-Bohr center so that protons can be released in the periplasm at physiological pH. This mechanism would imply structural conformational changes in the neighborhood of the redox-Bohr center, which was assigned to heme IV propionate 13 (P_{13}^{IV}) in the wild-type protein [27]. The proposed mechanism involves the disruption of an hydrogen bond formed between the O7 of P_{13}^{IV} and the carbonyl oxygen of Lys[7] located in the β-turn (residues 7-12), which causes the observed pH-linked conformational changes in the β-turn [27].

Compared to the wild-type protein, the properties of the PpcAF15L redox-Bohr center, namely the redox-Bohr interactions, are different (Table 7). However, as in the wild-type, the redox-Bohr interaction for heme IV is considerable higher as compared to the other hemes, suggesting that the redox-Bohr center is also located in the vicinity of heme IV. The analysis of the chemical shift variation in the ^{1}H-^{15}N HSQC NMR spectra in the pH range 5.4-9.5 showed that in both proteins the same set of signals is most affected, although at different extents (*cf*. open and closed symbols in Figure 19A and solid and dashed lines in Figure 19B). These include backbone NH of Lys[7], Ala[8], Asn[10], Ile[38] and the side chains of Asn[10] and Gln[21].

Residues Lys[7], Ala[8] and Asn[10] are part of the β-turn segment connecting the two-strand β-sheet near heme IV; Gln[21] is located in the first α-helice between I and III, whereas Ile[38] is a fully conserved residue within the family of *G. sulfurreducens* triheme cytochromes c_7 and forms a conserved hydrogen bond between the backbone amide proton and the carboxyl oxygen of P_{13}^{I} [70]. Compared with the other pH dependent signals, the pK_a of the backbone amide signal of Ile[38] is more acidic (pK_a 5.2 versus an average value of 7.8 for the other amide signals) and the decrease of the proton chemical shift at low pH correlates with the disruption of a hydrogen bond formed between the amide proton and the carboxyl oxygen of P_{13}^{I} upon protonation of the

latter. A similar behavior for this signal was observed in the wild type proteins, but the smaller $\Delta\delta_{avg}$ value (0.56 *versus* 0.71 in the wild-type) and the lower pK_a (5.2 *versus* 5.5 in the wild-type) are clearly indicative of rearrangements in this region of the protein.

On the other hand, the chemical shift of Gln^{21} side chain amide protons (εNH_2) are strongly shifted upfield (2.04 and 5.08 ppm) compared to their average position at 7.1 ppm obtained from approximately 10^4 chemical shifts as reported in the Biological Magnetic Resonance Data Bank (http://www.bmrb.wisc.edu/ref_info/statsel.htm#4). This feature was already observed in PpcA in which the chemical shifts of the Gln^{21} side chain amide protons are 1.11 and 4.56 ppm. The signals at 5.08 and 4.56 ppm are week due to their close proximity to the water signal and at the spectra level represented in Figure 21 they are not visible. The side εNH_2 protons of Gln^{21} are located in close proximity to the heme I axial histidine ring ($His^{17(I)}$) and subjected to the local external static magnetic field originated from heme I ring-current shifts. Thus, given the nearly axial position of Gln^{21} side chain in relation to heme I (Figure 25) the signals are upfield shifted relatively to their average position.

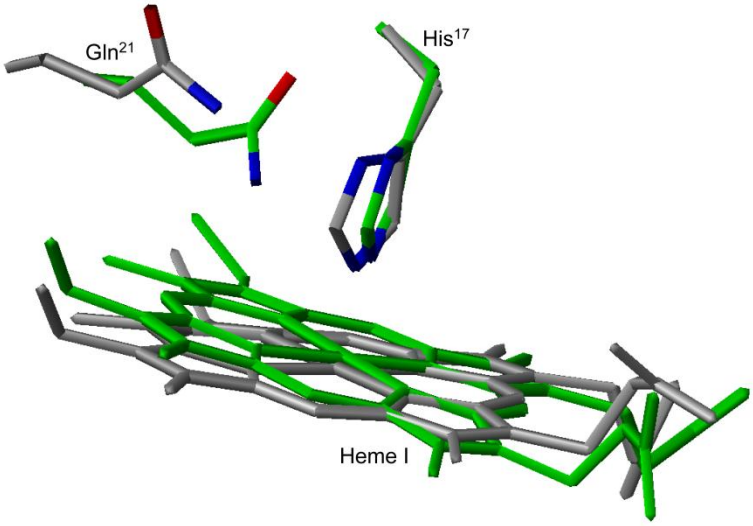

Figure 25 - Spatial disposition of residues Gln^{21} and His^{17}, which are located in the close proximity of heme I, in PpcAF15L (green) and PpcA (gray) solution structures. Structures were superimposed in MOLMOL [50] using backbone atoms.

The differences observed for the chemical shift of the Gln^{21} εNH proton in PpcAF15L and PpcA can be explained by conformational reorientations of the α-helice formed by residues His^{17}-Ala^{23}, as discussed. This polypeptide segment is located far from the redox-Bohr center (see below) and its pH dependence is probably due to protonation of groups in vicinity of Gln^{21}, among which the side chain of Lys^{18} is the best candidate since it also shows a considerable variation of $\Delta\delta_{avg}$ in the two proteins.

On the other hand, the pK_a values obtained for the NH signals of Lys^7, Ala^8 and Asn^{10} (8.5 *versus* 8.6 in the wild-type) [70], correlate with the pK_a value of the redox-Bohr center previously determined for the fully reduced and protonated protein [63], and are likely to be caused by the protonation/deprotonation of the redox-Bohr, which can also be assigned to P_{13}^{IV} in the mutant. This propionate is considerably less exposed to solvent than P_{17}^{IV} in both proteins

(the accessible surface area of the P_{13}^{IV} and P_{17}^{IV} propionate oxygens for PpcA are 16.3Å^2 and 44.1 Å^2, respectively and those for F15L mutant are 12.9 Å^2 and 40.7 Å^2) and thus it is not surprising that the pK_a of residues Lys^7, Ala^8, Asn^{10} that are located in the vicinity of P_{13}^{IV} have similar pK_a as a response to the protonation/deprotonation of the redox-Bohr center. However, these NH signals showed considerably different $\Delta\delta_{avg}$, which can be explained by the conformational changes that occurred in the vicinity of heme IV (Figure 26).

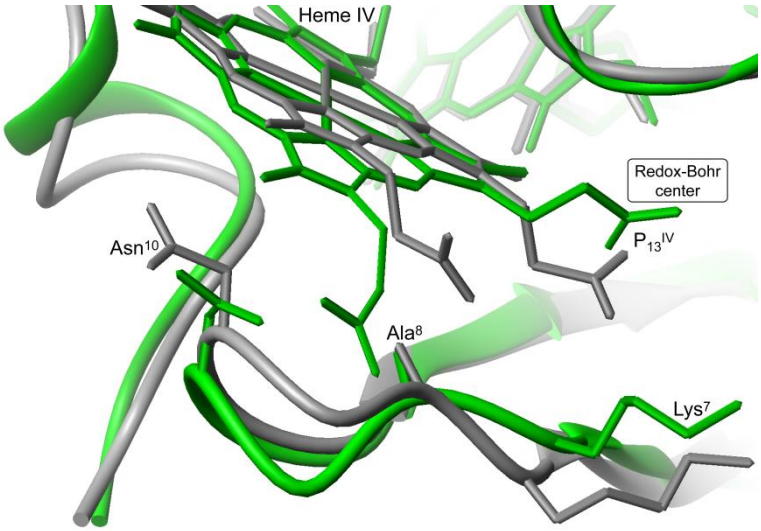

Figure 26 - Structural map of residues involved in the pH-dependent conformational changes in vicinity of redox-Bohr center P_{13}^{IV} in PpcAF15L (green) and PpcA (gray) solution structures. Structures were superimposed in MOLMOL [50] using backbone atoms.

These changes include the slight orientation of heme IV in relation to heme I (see also Table 6) and β-turn between the two-strand antiparallel β-sheet at the N-terminus comprising residues Lys^7, Ala^8 and Asn^{10} (Figure 26). By keeping propionate P_{13}^{IV} buried in the hydrophobic heme core of the mutated protein, these structural rearrangements are likely to explain the different redox-Bohr interactions in the two proteins.

4.3 CONCLUSIONS

The structure of PpcA mutant PpcAF15L, determined in the present work, shed light on the structural-functional role of the strictly conserved amino acid Phe^{15} in fine-tuning the heme reduction potentials and the network of redox and redox-Bohr cooperativities that are crucial for functional mechanism of PpcA. Though the overall folding of the protein was not affected, important local structural rearrangements caused by the replacement of Phe^{15} by a leucine residue were observed at the level of heme axial ligand geometries and secondary elements, which altered the structural features of the hydrophobic core and at the region of the redox-Bohr center. Overall, these structural rearrangements resulted in lowering the reduction potentials of the hemes and altered the properties of the redox-Bohr center. The analysis of the chemical shift variation of the backbone and side chain amide signals with pH allowed mapping the pH-linked conformational changes caused by protonation/deprotonation of the redox-Bohr center, which was assigned to heme propionate P_{13}^{IV}. These changes unbalance the redox and redox-Bohr cooperativities and alter the distribution of the protein microstates during its redox cycle. As a consequence, while in the wild-type protein a concerted e^-/H^+ transfer gives the protein the necessary thermodynamic properties to convert electronic energy into proton motive force, a fundamental step that might contribute to the proton electrochemical gradient across the bacterial cytoplasmic membrane, in the mutant this feature is no longer observed, highlighting the key role played by Phe^{15} in PpcA overall functional capabilities.

5. Mapping the interaction sites of PpcA

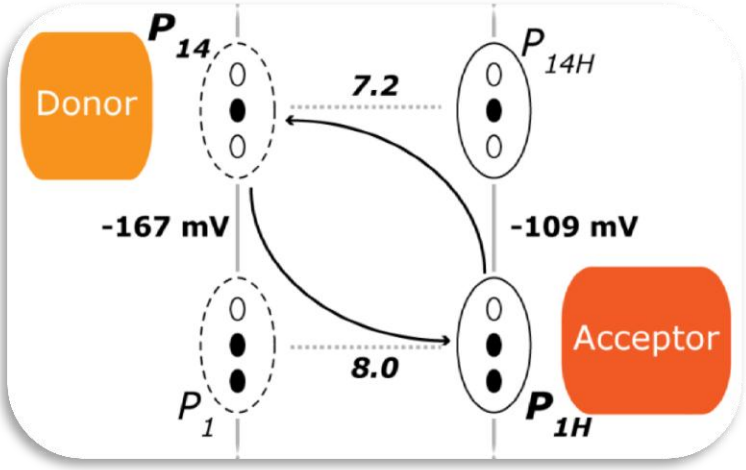

5. MAPPING THE INTERACTION SITES OF PPCA

Microbial respiration using redox-active organic small molecules to shuttle electrons between reduced and oxidized compounds, can be performed through various strategies. These strategies include microorganisms that require direct contact (*e.g., Geobacter* species) [13] and those that do not (*e.g., Shewanella* species) [71]. The latter pathway is driven by extracellular electron transfer, where these species produce electron shuttles to promote the indirect transfer of electrons from the cell surface to extracellular acceptors. Alternatively, *Geobacter* species need to directly contact insoluble acceptors (*e.g.,* Fe(III) oxides) in order to reduce them, since these species do not produce electron shuttles.

In the case of *G. sulfurreducens* bacterium, it can also grow in presence of humic substances as the humics analogue 9,10-anthraquinone-2,6-disulfonate (AQDS), as electron acceptor or electron donor [72, 73]. Humics are natural organic matter formed from the decomposition of plant, animal, and microbial tissues which can be readily isolated from nearly all soils, waters, and sediments. AQDS is commonly used to investigate the mechanisms that occur in the humics respiration [74]. Preferred use of AQDS in experiments arise from its stability towards irreversible side reactions, low standard reduction potential, high water solubility, and the convenience of analysis using UV–visible spectrophotometer (reduced form is bright orange, while oxidized form is clear). All known humics-reducing microorganisms are capable of transferring two electrons to AQDS, reducing it to 9,10-anthrahydroquinone-2,6-disulfonate (AH_2QDS) [72, 75]. This hydroquinone participates in the electron transfer processes coupled to H^+ transfer.

Several studies revealed that the reduction of Fe(III) oxides is increased in the presence of humics and/or AQDS [72] and, when the reduced humics interact with the Fe(III) oxides, they are reoxidized and can thus be recycled [76]. Alternatively, *Gs* can grow in presence of reduced humics and/or AQDS as electron donors for fumarate reduction [73]. In this instance, the organisms obtain carbon from readily degradable limited sources and simply use the reduced AQDS as an energy source [76]. Such metabolism gives these organisms a potential competitive advantage over other heterotrophs in the environment that may need a limited organic compound as both carbon and energy source, thus requiring significantly greater concentrations for growth [76]. Gene knockout experiments carried out in *Gs* cells suggested that the humics (or AQDS) respiration display multiple routes for the electron transfer [77] though the respiration underlying the use of these compounds is presently unknown.

Since AQDS has the ability to enter into the periplasm of the cells and couples e^-/H^+ transfer [77, 78], it was investigated as a putative redox partner of the periplasmic cytochrome PpcA in this work by UV-visible and NMR spectroscopy.

5.1 RESULTS

5.1.1 PURIFICATION OF ^{15}N-LABELLED AND UNLABELLED PPCA

As described in the Experimental procedures section, ^{15}N-labelled and unlabelled PpcA were purified using an identical methodology. After the expression, the proteins were purified by cation exchange and molecular exclusion chromatography. The chromatograms obtained from ionic exchange and molecular exclusion chromatographic steps, as well as the purification progress monitored by SDS-PAGE electrophoresis for ^{15}N-labelled and unlabelled PpcA are indicated in Figure 27 and Figure A2 (Appendix).

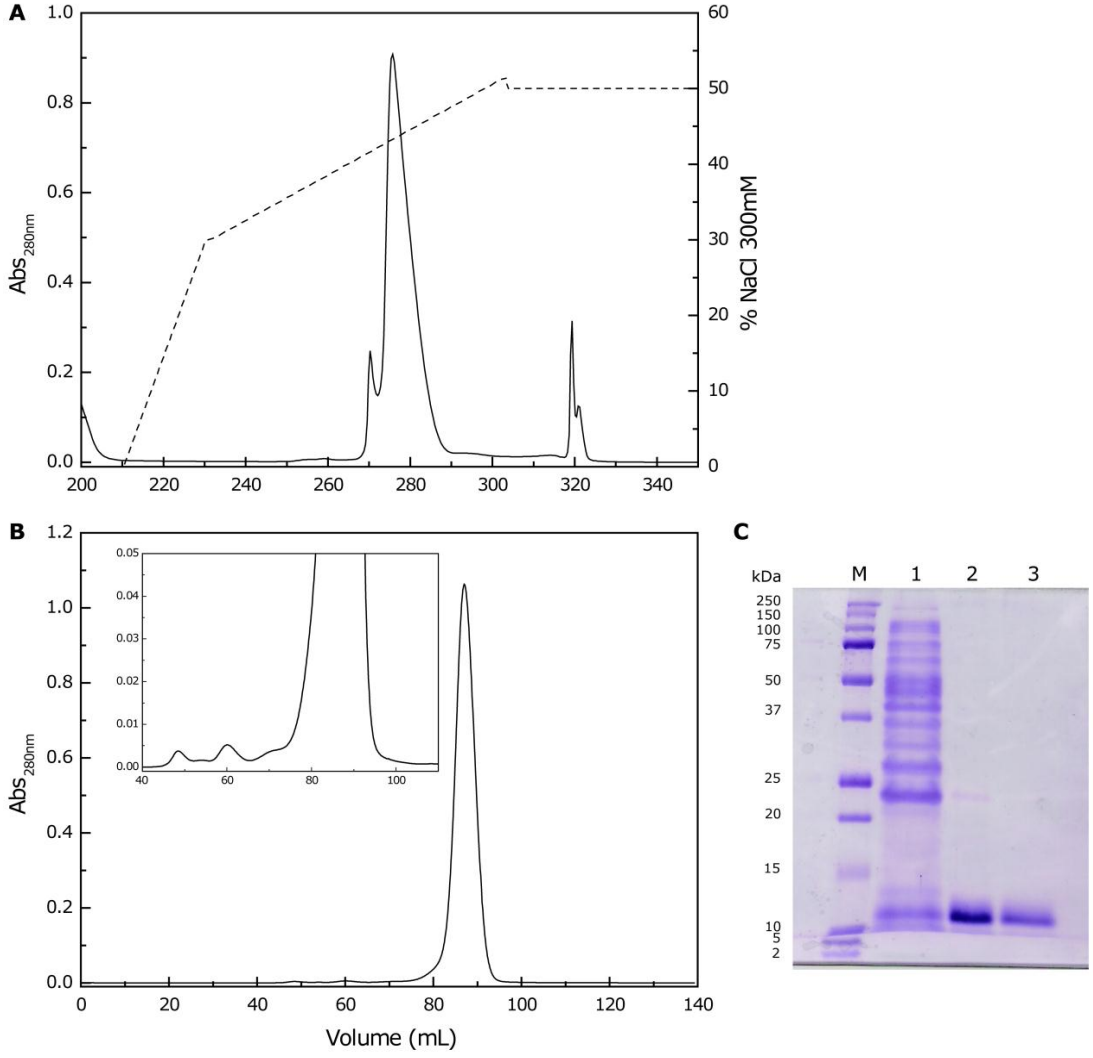

Figure 27 – **Purification of ^{15}N-labelled PpcA**. (A) Elution profile for the cation exchange column chromatography equilibrated with 10mM Tris-HCl, pH 8.5 and eluted at a flow rate of 1mL/min. Primary and second *y*-axis, report the variation of absorbance at 280 nm (solid line) and the NaCl gradient profile (dashed line), respectively. (B) Elution profile for the molecular exclusion column chromatography equilibrated with 100mM sodium phosphate buffer, pH 8. The inset shows an expanded view of the chromatogram. (C) Purity analysis by SDS-PAGE electrophoresis. Lane M: prestained protein marker; lane 1: periplasmic fraction; lane 2: after purification by cation exchange chromatography; lane 3: after purification by molecular exclusion chromatography. The MW of the protein markers are indicated on the left.

Due to the high isoelectric point of PpcA (9.44) it strongly binds to the cation exchange column equilibrated with 10mM Tris-HCl (pH 8.5). The bound protein was then eluted with a sodium chloride gradient ranging from 0 to 300mM. The protein of interest was eluted at 43% of the gradient (Figure 27A). This fraction was further purified by molecular exclusion chromatography and the protein of interest was eluted at 87mL with 100mM sodium phosphate buffer, pH 8 (Figure 27B). After this purification step, only one band was observed in the SDS-PAGE electrophoresis (see lane 3 in Figure 27C). This band corresponds to a MW of approximately 10kDa in agreement with the 9.57kDa calculated for PpcA [10]. Protein yields were quantified by UV-visible spectroscopy using the PpcA extinction absorption coefficient of the α band characteristic of the reduced protein (ε_{552nm} = 97.5mM^{-1}cm^{-1} [65]). The yields obtained for ^{15}N-labelled and unlabelled PpcA were 2.7 and 2mg per litre of cell culture, respectively.

5.1.2 UV-VISIBLE STUDIES

UV-visible spectroscopy was used to investigate the extent to which PpcA was reduced (or oxidized) by AH_2QDS (or AQDS). This was possible since the spectral signatures of the protein and the putative redox partner are slightly different (Figure 28).

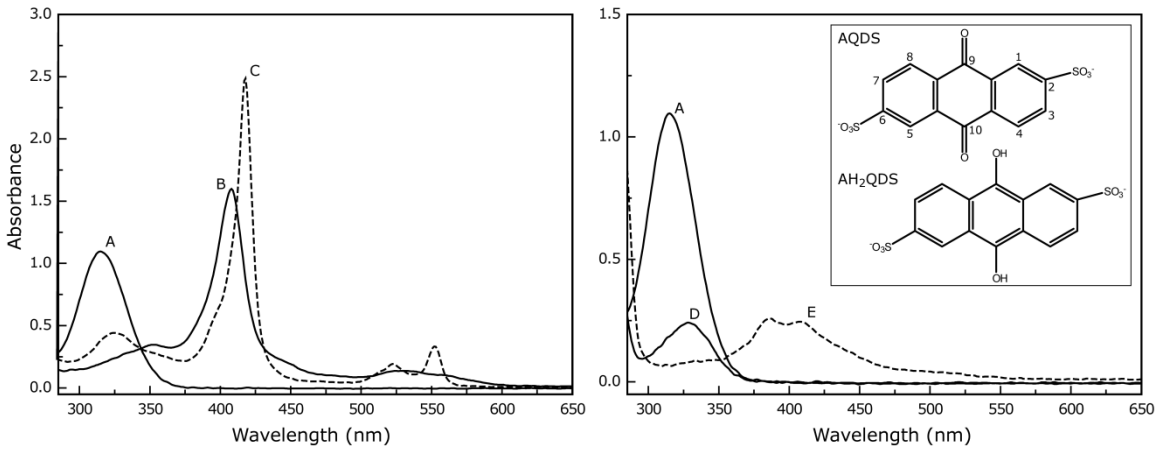

Figure 28 - UV-visible absorption spectra of 0.14mM sodium dithionite (A), 0.31mM PpcA (B and C) and 2.5mM AQDS (D and E) at pH 7.1. The solid (B and D) and dashed lines (C and E) represent fully oxidized and fully reduced species, respectively. Sodium dithionite was used to reduce both samples. Structures for 9,10-anthraquinone-2,6-disulfonate in the inset fully oxidized/deprotonated (AQDS) and fully reduced/protonated (AH_2QDS) forms are represented. These structures were drawn with program ChemBio Draw Ultra 12.0.

The left panel of Figure 28 displays the typical absorption spectra of *c*-type cytochromes containing hemes in the low spin state. The spectrum in the oxidized form (Figure 28 - spectrum B) is dominated by a band with a maximum at 406nm (Soret band). After reduction with sodium

dithionite, three bands are observed at 417nm (Soret band), 522nm (β band) and 552nm (α band) (Figure 28 - spectrum C). On the right panel, the UV-visible absorption spectra of AQDS in the fully oxidized/deprotonated form displays an absorption band with a maximum at 325nm (Figure 28 - spectrum D), whereas the spectrum of the reduced/protonated state shows two bands almost overlapped with maximums at 385nm and 410nm (Figure 28 - spectrum E). These spectral signatures were used to evaluate the extent to which PpcA was reduced (or oxidized) by AH_2QDS (or AQDS). For the reduction of PpcA and AQDS, equivalent amounts of sodium dithionite were used, which displays an absorption band with a maximum at 314nm (Figure 28 - spectrum A).

In Figure 29 is indicated the UV-visible spectra obtained for the assays of AH_2QDS oxidation coupled to PpcA reduction. The reduction of the AQDS solution (Figure 29 - spectrum A) was carried out by the addition of equimolar amounts of sodium dithionite (Figure 29 – spectrum B). After the addition of the oxidized PpcA sample, the protein was rapidly reduced (less than 1 min) and the UV-visible spectrum is dominated by the α and β bands typical of low-spin (S=½) ferrous *c* type hemes (Figure 29 - spectra C-E). The typical band of sodium dithionite with an absorption maximum at 314nm is not observed confirming that there is no excess of this compound in solution.

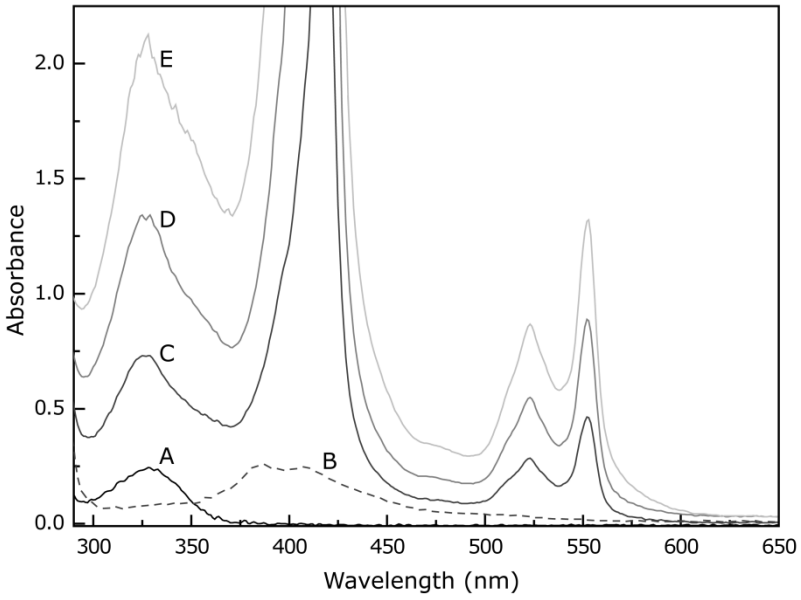

Figure 29 - Assays of AH_2QDS oxidation coupled to PpcA reduction at pH 7.1. UV-visible absorption spectrum of (A) oxidized AQDS (2.5mM), (B) AH_2QDS equimolar amount of sodium dithionite and reduced PpcA after addition of increasing amounts of PpcA (0.31mM) in the oxidized form at molar ratios AQDS/PpcA (added volume) of (C) 0.25 (11μL), (D) 0.5 (11μL) and (E) 1 (22μL).

The reverse experiment was also carried out by adding oxidized AQDS to a reduced sample of PpcA (prepared with an equimolar amount of sodium dithionite). The results obtained are indicated in Figure 30. In this case, after the addition of AQDS, even up to a molar ration of

40:1 (AQDS/PpcA), the electronic absorbance spectrum still kept the typical α and β bands of reduced PpcA (Figure 30 - spectra C-F).

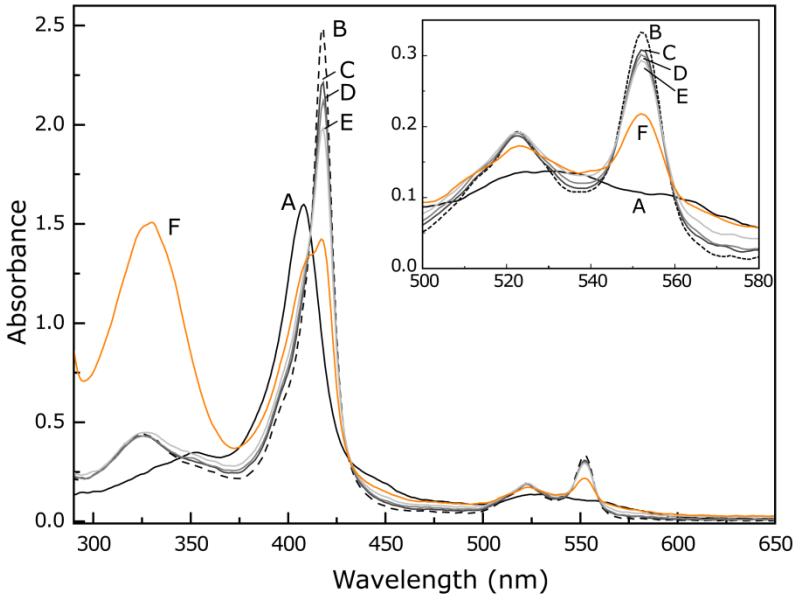

Figure 30 - Assays of AQDS reduction coupled to PpcA oxidation at pH 7.1. UV-visible absorption spectrum of (A) oxidized PpcA (0.31mM), (B) reduced PpcA with equimolar amount of sodium dithionite and PpcA after addition of increasing amounts of AQDS (2.5mM) in the oxidized form at molar ratios AQDS/PpcA (added volume) of (C) 0.25 (0.5μL), (D) 0.5 (0.5μL), (E) 1 (1μL) and (F) 40 (40μL).

5.1.3 PpcA-AQDS interaction probed by NMR

The molecular interaction between PpcA and AQDS was evaluated by probing the chemical shift perturbation of the backbone and side chain NH signals of PpcA, as well as of the heme substituents, in presence of the ligand. In order to achieve this, the heme substituent signals were assigned in both reduced and oxidized forms for the unlabeled PpcA sample in pure $^{2}H_2O$ (Tables B4 and B5 in Appendix), following the methodology presented in the Experimental procedures section. The polypeptide and side chain NH signals were previously assigned by Morgado L (personal communication).

The NH backbone and side chain chemical shift perturbations of PpcA in presence of increased concentrations of AQDS were monitored by recording a series of 2D-^{1}H-^{15}N HSQC NMR spectra (Figure 31 and 32). After addition of AQDS to oxidized PpcA, the residues that showed the highest chemical shift perturbations are Asn^{10}-Val^{13}, Lys^{43}, Glu^{44}, Ala^{46}, Lys^{52}, Cys^{65} and Lys^{70}, located near heme IV; and Cys^{27}, located near heme I (Figure 31).

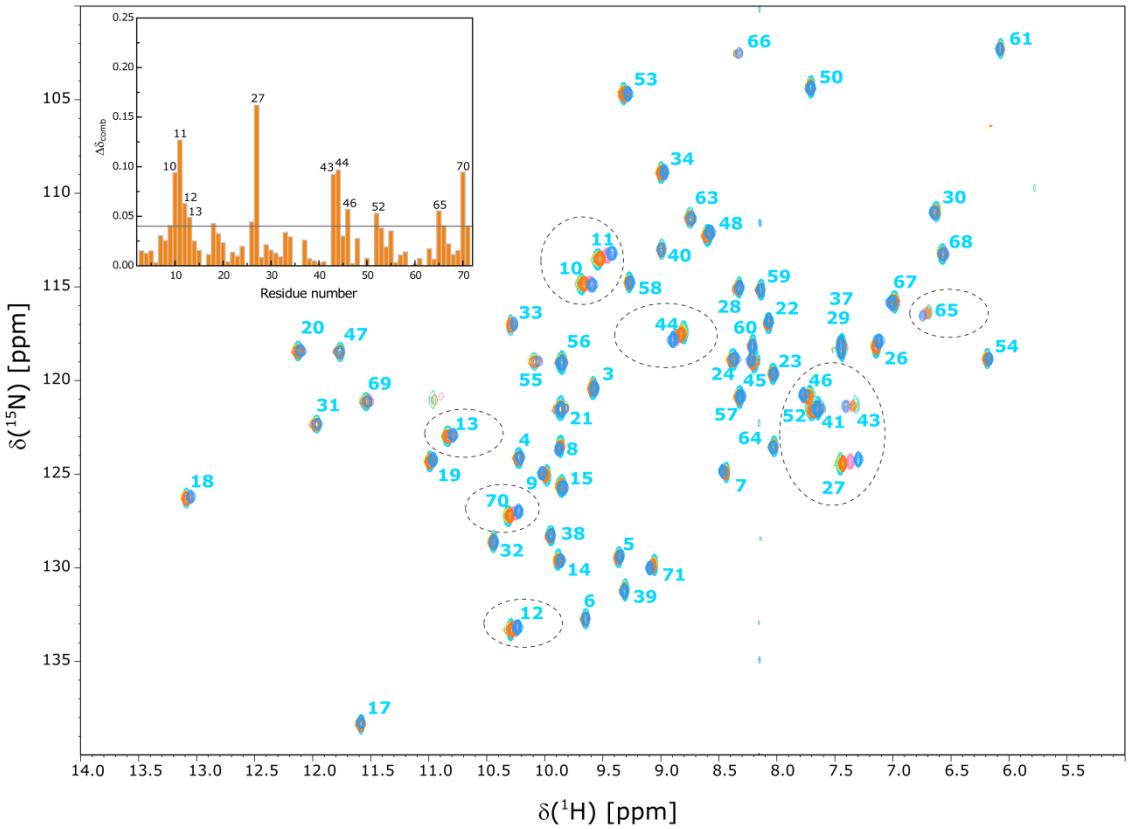

Figure 31 - ^{1}H-^{15}N HSQC spectra of ^{15}N-labeled PpcA in the presence of AQDS, in the oxidized form. Overlay of the HSQC spectra of ^{15}N-labeled protein sample in the presence of increasing amounts of AQDS in molar ratio [AQDS]/[PpcA] of 0, 1, 5, 20 and 50, corresponding to the cyan, yellow, orange, pink, and blue spectrum, respectively. The assignments of backbone amide groups are indicated in cyan. The inset shows the combined chemical shift changes determined on the basis of directly observed ^{15}N and ^{1}H chemical shifts according to the equation 4 (section 2.3.5). The cutoff value was calculated with the standard deviation to zero, σ_0^{corr}.

In the paramagnetic oxidized state of PpcA, the presence of unpaired electrons creates additional significant local magnetic fields on the heme signals and nearby residues. This effect can easily counteract or reinforce the changes observed in the affected signals. Moreover, as described in Chapter 4, small rearrangements in the orientation of the heme axial ligand ring planes can affect by several ppm units the chemical shifts of the heme substituents. Thus, in the present work, the NH backbone and side chain chemical shift perturbation of PpcA signals, in the presence of increased concentrations of AQDS, were also monitored in the diamagnetic reduced protein. In this case, the most affected signals correspond to residues Asn^{10}, Cys^{65}, Gly^{66} and His^{69} which are located near heme IV; and residue Gly^{36} that is located near heme I though at much smaller extent (Figure 32).

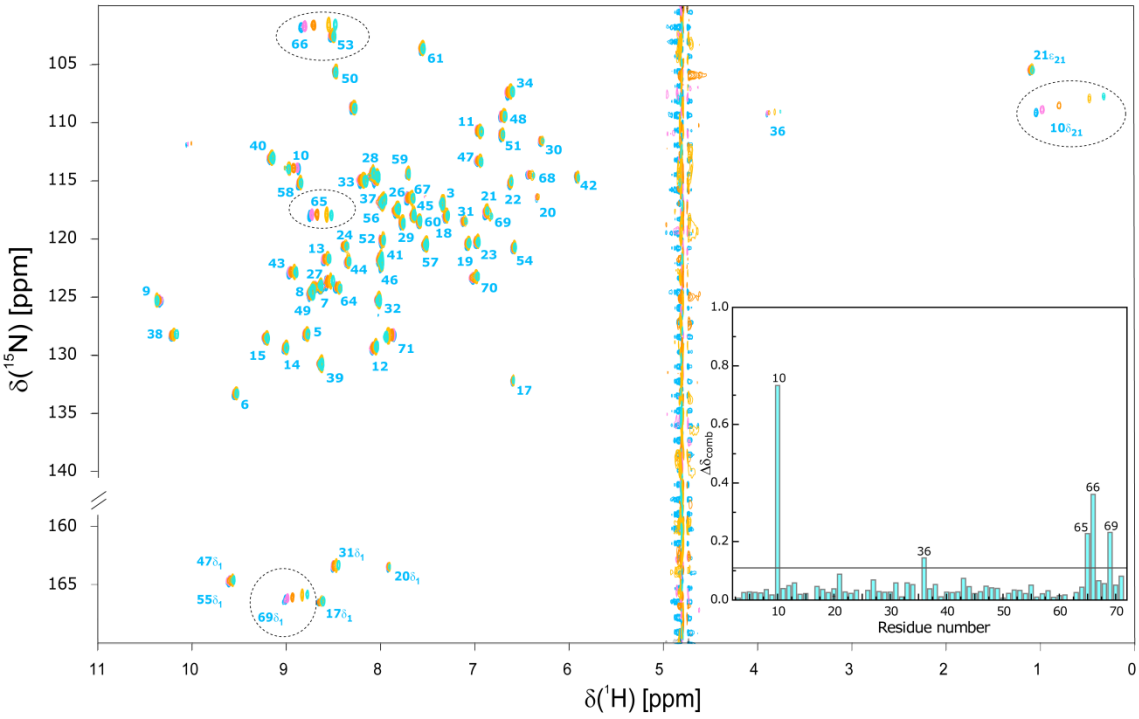

Figure 32 - ^{1}H-^{15}N HSQC spectra of ^{15}N-labeled PpcA in the presence of AQDS, in the reduced form. Overlay of the HSQC spectra of ^{15}N-labeled protein sample in the presence of increasing amounts of AQDS in molar ratio [AQDS]/[PpcA] of 0, 1, 5, 20 and 50, corresponding to the blue, pink, orange, yellow and cyan spectrum, respectively. The assignments of backbone amide groups are indicated in blue. The inset shows the combined chemical shift changes determined on the basis of directly observed ^{15}N and ^{1}H chemical shifts according to the equation 4 (section 2.3.5). The cutoff value was calculated with the standard deviation to zero, σ_0^{corr}.

An average K_D value was calculated from the titration curves determined for the residues with highest chemical shift perturbation for both redox states (Figure 33). For the experiments in the reduced state, a K_D of 8.0±1.0mM (25ºC, pH 7.1) was determined from the titration curves of the residues Asn^{10}, Cys^{65}, Gly^{66} and His^{69}, which are in the vicinity of heme IV. The studies on the oxidized form revealed that other residues are affected, namely, Asn^{10}-Val^{13}, Cys^{27}, Lys^{43}, Glu^{44}, Ala^{46}, Lys^{52}, Cys^{65} and Lys^{70}. The K_D determined was 18.3±5.7mM (25ºC, pH 7.1) calculated from the titration curves corresponding to Asn^{10}, Lys^{43}, Ala^{46}, Gly^{11}, Asp^{12}, Val^{13}, Glu^{44} and Lys^{70} residues.

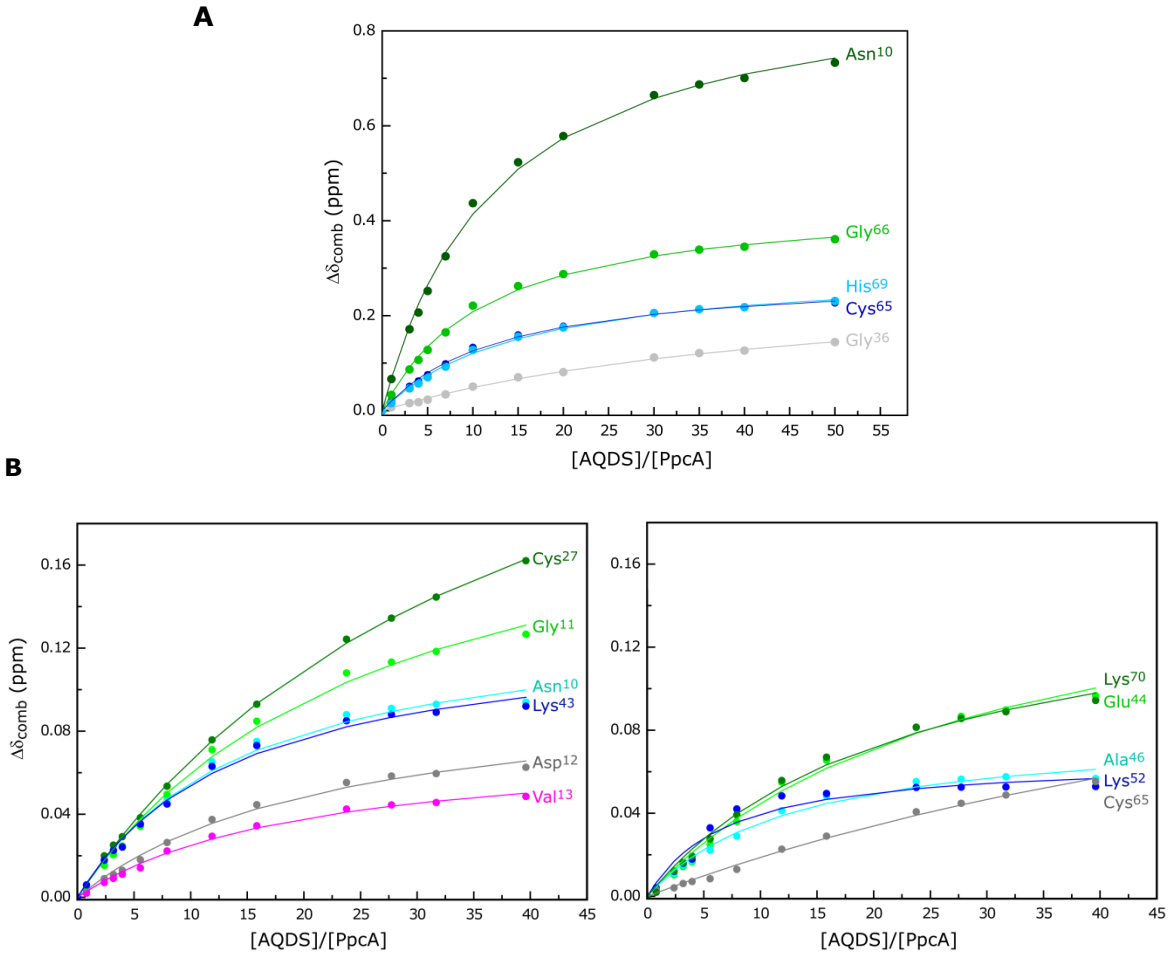

Figure 33 - Titration curves of chemical shift changes ($\Delta\delta_{comb}$) in ^{1}H-^{15}N HSQC spectra observed for representative residues of PpcA in the (A) reduced and (B) oxidized form, as a function of molar ratio [AQDS]/[PpcA]. The curves were fitted using the equations 6 and 7 (Section 2.3.4).

The interactions between AQDS and PpcA were further evaluated at the level of the heme substituent proton signals. In this case, a molar ratio of 1:5 (PpcA/AQDS) was used in order to allow observing eventual perturbations on the chemical shifts of the heme substituent proton signals without losing spectral quality. The comparison of the heme substituent proton chemical shifts in absence and presence of AQDS is indicated in Figure 34A and B for the reduced and oxidized forms, respectively. The extent of the heme substituents assignment is 93% and 78% for the reduced and oxidized forms, respectively, and includes substituents of all heme moieties. The more affected signals are the heme IV substituents, in particular the three heme moieties that contain the meso protons H5, H15 and H20 (see Figure 34A and B).

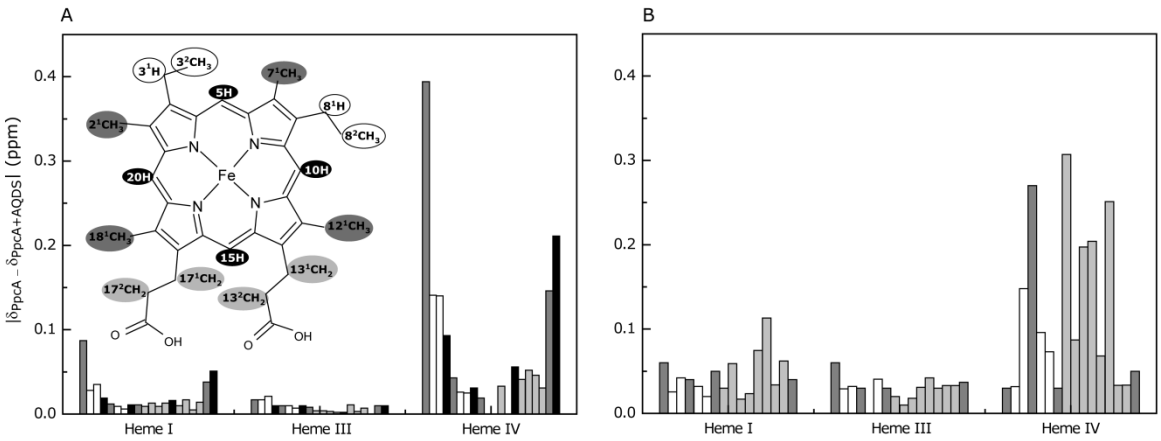

Figure 34 - ^{1}H chemical shift changes (δ_{PpcA}-$\delta_{PpcA+AQDS}$) of the PpcA heme groups in the (A) reduced and (B) oxidized form. The white, light gray, gray and back bars represent the ^{1}H chemical shift variations of thioether methines/thioether methyls, propionates αCH_2 protons, methyl groups and meso protons, respectively. In each set of bars the heme substituents are represented clockwise in the following order: 2^1CH_3, 3^1H, 3^2CH_3, 5H, 7^1CH_3, 8^1H, 8^2CH_3, 10H, 12^1CH_3, 13^1CH_2, 13^2CH_2 15H, 17^1CH_2, 17^2CH_2, 18^1CH_3, 20H (see the inset).

The interaction between PpcA and AQDS was further confirmed by monitoring the pattern of the AQDS signals in the 1D-^{1}H NMR spectra (Figure 35) and in the 2D-^{1}H-NOESY spectra (Figure 36).

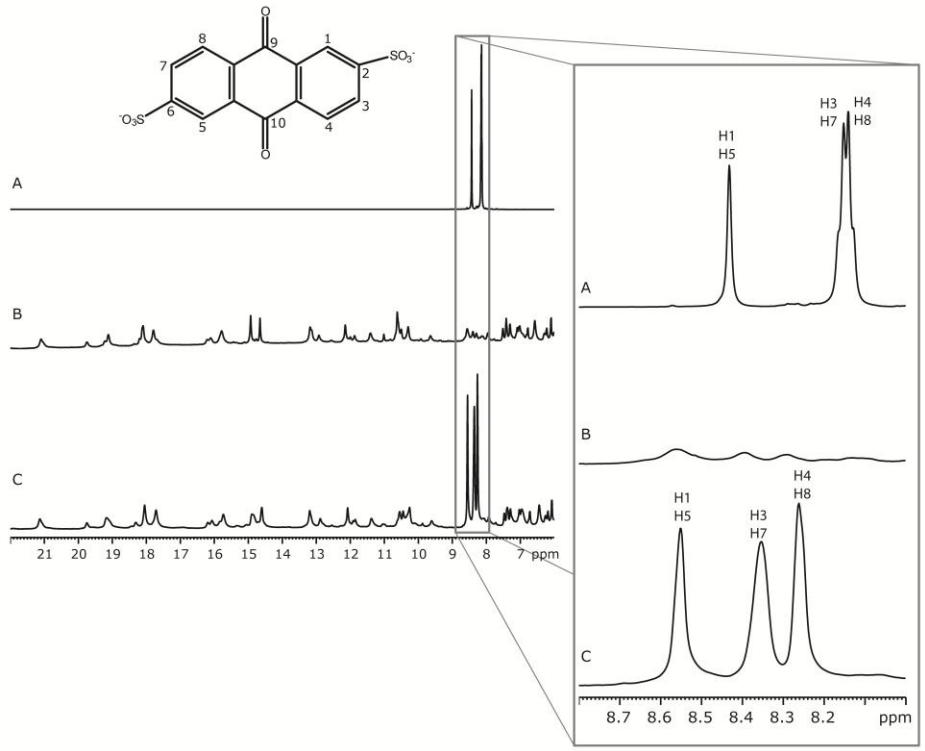

Figure 35 – 1D-^{1}H NMR spectra of (A) AQDS, (B) PpcA and (C) PpcA in the presence of AQDS in a molar ratio of 1:5 (PpcA:AQDS) in the oxidized form. The expansion shows the proton signals of AQDS. All samples were prepared in 45mM phosphate buffer pH 7.1 (I = 100mM) and all spectra were acquired at 25ºC.

In the AQDS molecule, three types of nonequivalent protons exist. The first type is the H1 and H5. These protons are more deshielded and, consequently, their signals are observed at lower magnetic field values (higher chemical shift), due to the presence of the electron-withdrawing substituent sulfonate ion, in the 1D ^{1}H NMR spectrum.

The H3/H7 protons and H4/H8 protons are the other two types of nonequivalent protons, and their signals are shifted to high field, compared to H1/H5. Amongst these two type of nonequivalent protons, the more shielded ones are H4/H8 because they are located further apart from the sulfonate ion. The assignment of these signals is indicated in Figure 35 (spectrum A). In the presence of the protein (Figure 35 – spectrum C), the proton signals of AQDS are shifted to higher chemical shift values, supporting the existence of a molecular interaction between the protein and AQDS. In addition, in 2D-^{1}H-NOESY spectra, the cross-peak between the H3/H7 and H4/H8 protons of AQDS exhibit the same sign as the diagonal (negative NOEs), a feature only observable if a small molecule like AQDS is bound to a high molecular entity (Figure 36).

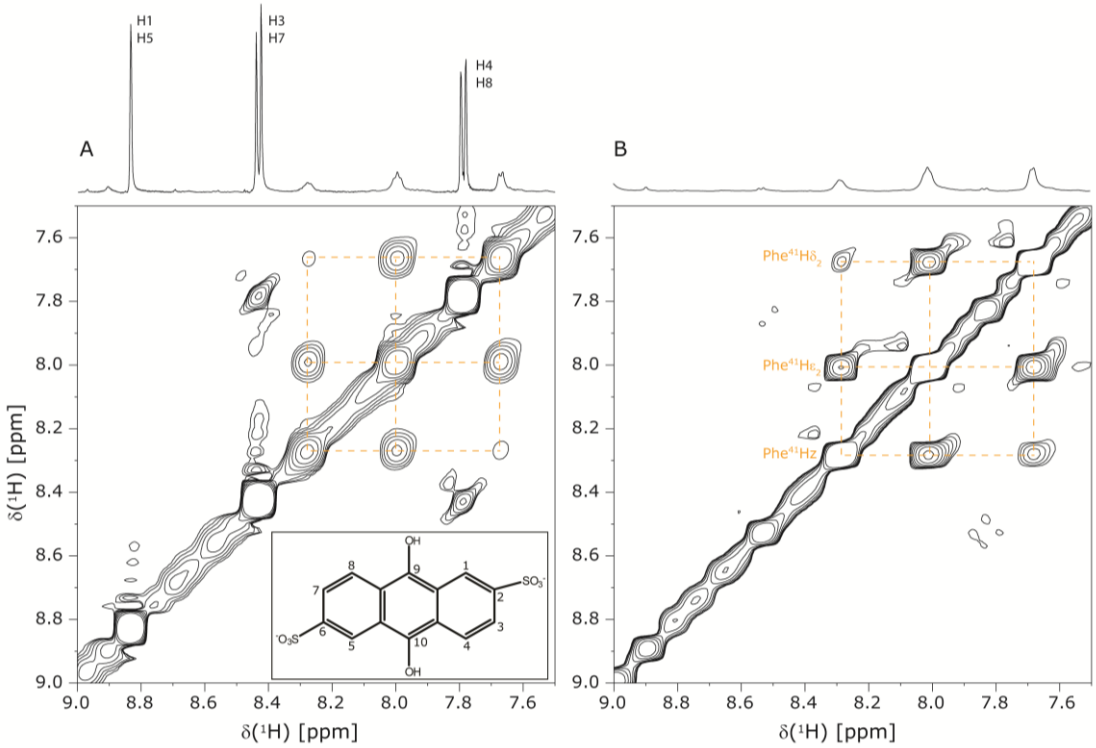

Figure 36 – 2D-^{1}H-NOESY spectra of unlabeled PpcA in the (A) presence and (B) absence of AQDS in the reduced form. The 1D spectra acquired before each 2D experiment is represented above each 2D-^{1}H-NOESY spectra. The cross-peaks between the protons of Phe^{41} ring are representing by dashed lines.

Finally, in order to evaluate the reversibility of the interaction between PpcA and AQDS, 1D-^{1}H NMR spectra obtained before and after removal of the ligand by ultrafiltration (Amicon Ultra, 3k), were acquired (Figure 37).

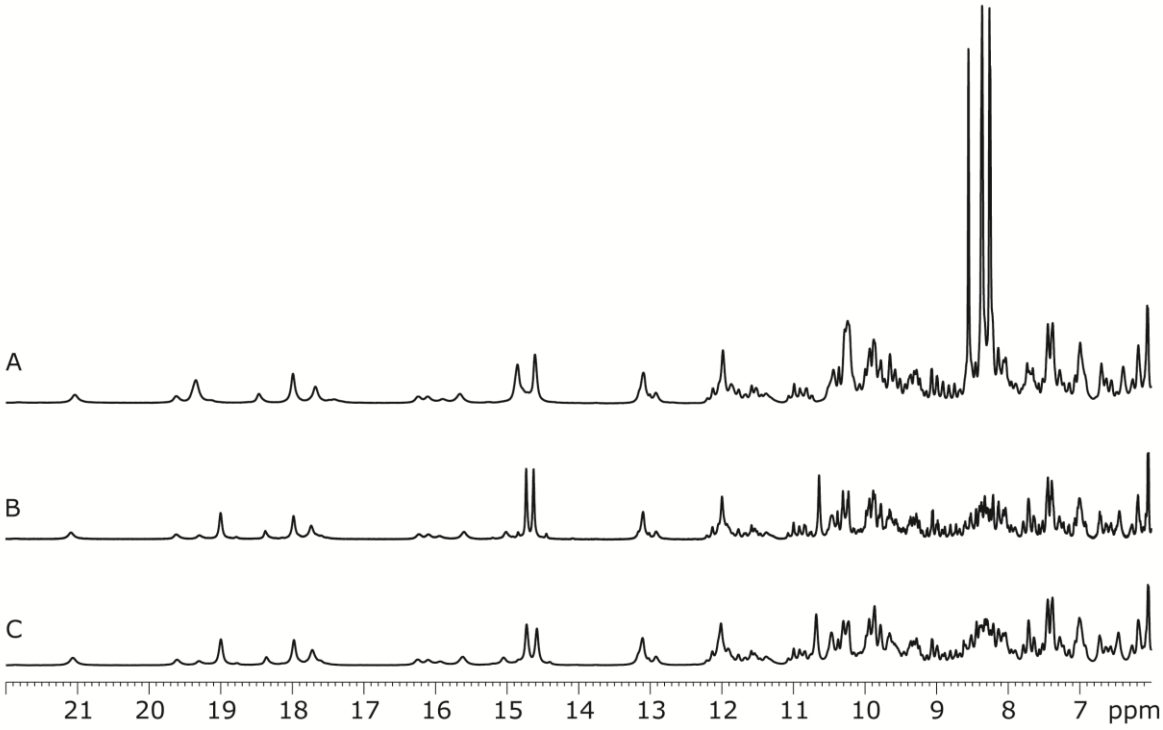

Figure 37 - 1D-^{1}H NMR spectra of low field region of (A) PpcA in the presence of AQDS in a molar ratio of 1:5 (PpcA/AQDS), PpcA (B) before and (C) after removal of the ligand by ultrafiltration. All samples were prepared in 45mM phosphate buffer pH 7.1 (I=100mM) and all spectra were acquired at 25ºC. This experiment was performed in the oxidized form.

5.2 Discussion

The results obtained from the UV-visible experiments showed that after addition of increasing amounts of oxidized AQDS to reduced PpcA, the protein remains in the reduced form (Figure 30). On the other hand, AH_2QDS can reduce PpcA, which is in agreement with the reduction potential values of these species (Figure 29). Indeed, at pH 7.0 the reduction potential of AQDS is -184mV [79], whereas that of PpcA is -117 mV *versus* SHE [24] favoring the electron transfer towards the latter one.

Concerning to the NMR experiments, the chemical shift perturbations of amide and heme substituents signals suggested that PpcA and AQDS interact with each other. This interaction was further confirmed by conferring the pattern of AQDS ^{1}H-NMR signals in presence and absence of PpcA (Figure 35 and 36). Indeed, in the presence of oxidized or reduced PpcA the pattern of the AQDS signals are quite distinct further confirming the existence of a molecular interaction between the protein and the putative redox partner. Additionally, the backbone and side chain NH signals of PpcA, demonstrated that the most affected region by the presence of AQDS is located in the vicinity of heme IV (Figure 38).

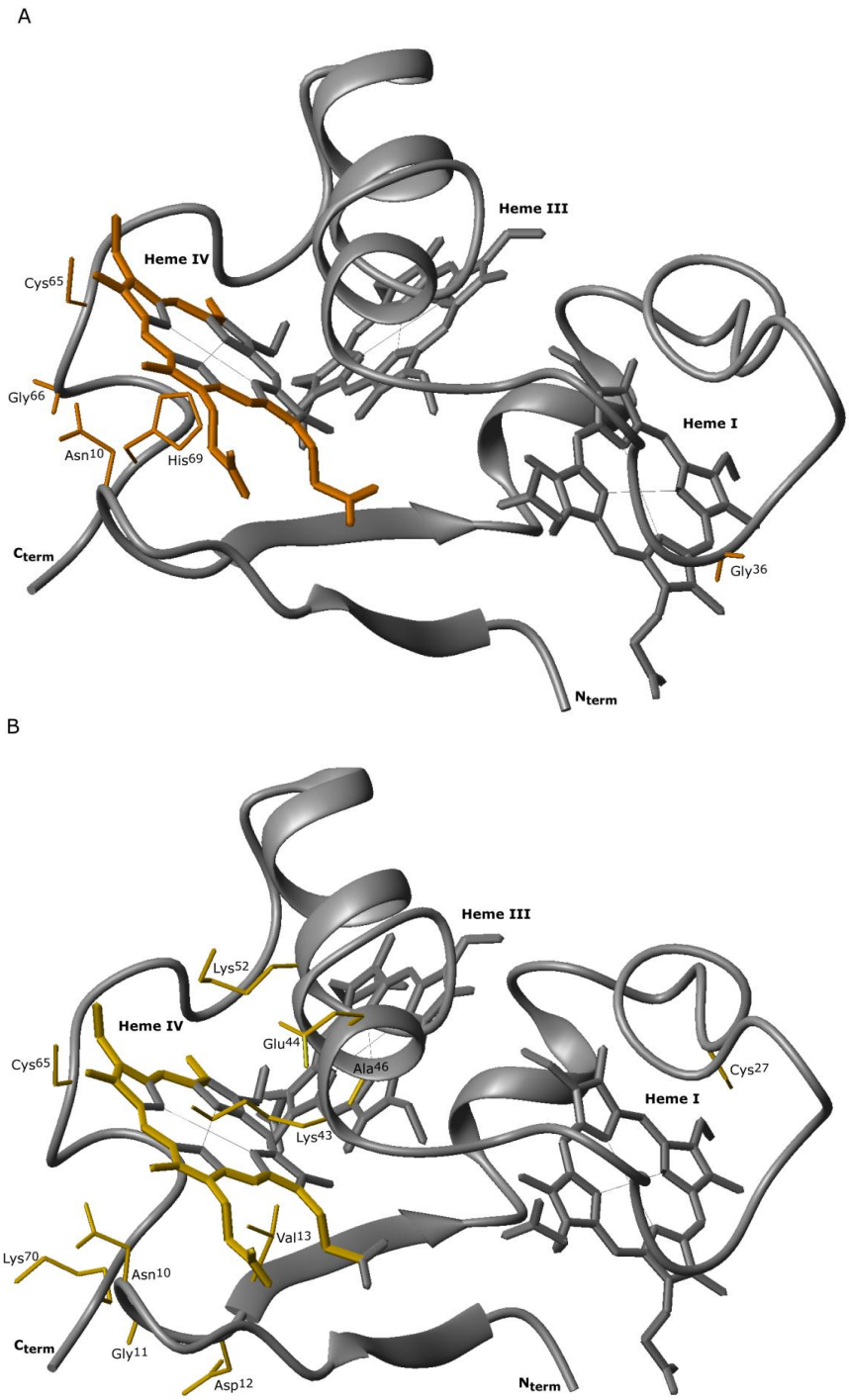

Figure 38 – PpcA region containing the most affected residues and heme substituents in the presence of ADQS in the (A) reduced and (B) oxidized forms. Figures were produced using MOLMOL [50].

As depicted in Figure 2, PpcA has a high content of lysine residues (24%) which confers to the protein a highly positive charged surface near heme IV. In addition, in the crystal structure of PpcA it was shown that lysine residues located in the vicinity of heme IV form an anion binding region where a sulfate was found. In the case of AQDS, the presence of two negatively charged sulfonate ions (see Figure 28D and E) is likely to drive AQDS toward heme IV.

The equilibrium dissociation constant (K_D) was estimated from the concentration-dependent titration in reduced and oxidized forms, for the amide signals corresponding to the residues with important chemical shift changes. The dissociation constant K_D was determined under fast exchange conditions and assuming a single binding site with 1:1 stoichiometry for both reduced and oxidized forms, accordingly to the following equilibrium: P + L ↔ PL, where P and L correspond to PpcA and redox ligand, respectively. The K_D values (in the mM range) obtained from the fitting of the ligand-induced chemical shift perturbation curves suggests a formation of a low affinity complex. The magnitude of the dissociation constant are typical of weak complex, a requisite to ensure fast dissociation rate constants and fast electron transfer between redox partners [80].

Furthermore, it is interesting to note that the redox-Bohr effect observed in PpcA was attributed to the protonation/deprotonation of heme IV propionate 13 (P_{13}^{IV} – see also Chapter 4). The protonation/deprotonation of this redox-Bohr center was proposed to drive the concerted e^-/H^+ transfer observed in PpcA [30]. The functional mechanism proposed for PpcA based on their thermodynamic properties suggested that PpcA microstate P_{14} can uptake electrons and a weakly acidic proton from the donor, originating the microstate P_{1H}. Upon protonation of the redox-Bohr center, the reduction potential of the hemes become less negative. The loss of electron reducing power is used to lower the pK_a of the proton so that when meeting the physiological downstream redox partner, microstate P_{1H} donates less reducing electrons and a more acidic proton (see Figure 7, section 1.3).

The proposed mechanism fits well with the observations obtained in the present study. Indeed, the pK_a values of AQDS (approximately 7.5 and 11 [79]) are too high to be released in the periplasm. The heme redox potential of heme IV at pH 7.1 can be determined from the PpcA thermodynamic parameters listed in Table 2 (section 1.3). The reduction potential of heme IV in such conditions is -114mV being comparable to the macroscopic value determined for PpcA (-117mV). Thus, it reasonable to assume that AQDS can donate electrons and protons to PpcA, which can couple the deenergization of electrons to the lowering of proton pK_a values to favour their release in the periplasm. This process favours the H^+ electrochemical potential gradient across the periplasmic membrane that drives ATP synthesis.

Coates *et al.*, 2002 showed that *Geobacter* organisms, among others, can convert AH_2QDS to AQDS during growth without affecting the anthraquinone concentration [76]. This indicated that AH_2QDS is not degraded as a carbon source by the organisms, being simply oxidized as energy source. Consequently, the mechanism described for AQDS-PpcA coupling would also explain how AQDS-oxidizing organisms can obtain carbon from readily degradable limited sources and simply use the reduced AQDS as an energy source.

5.3. CONCLUSIONS

Analysis of the UV-visible spectra showed that AH_2QDS can reduce PpcA in agreement with their reduction potentials values. The comparison of the NMR data obtained for PpcA, in presence and absence of AQDS, showed that the interaction between the two molecules is reversible. The analysis of the chemical shift perturbation of the backbone and side chain NH signals, as well as those of the heme substituents, showed that the ones most affected were essentially confined to the neighbourhood of heme IV. This heme group has been previously identified as the putative entry gate for electrons into PpcA [30], an hypothesis that agrees with the results obtained in this work with AH_2QDS. This suggests that AH_2QDS can transfer electrons and protons to PpcA. The electrons are then deenergised by the cytochrome and the resultant energy used to lower the pK_a of the AH_2QDS protons, allowing their release in the periplasm. Such mechanism could contribute to the proton gradient across the cytoplasmic membrane.

The molecular interaction between PpcA and AQDS probed in this work constitutes the first step toward the rationalization of the *Gs* respiratory chain.

6. Final conclusions

6. FINAL CONCLUSIONS

Extracellular electron transfer is one of the physiological hallmarks of *G. sulfurreducens.* Amongst the over 100 cytochromes detected in the *Gs* genome, a family composed by five periplasmic triheme cytochromes c_7 (PpcA-E) was identified.

This Thesis focused on the characterization of these proteins using NMR and UV-visible spectroscopies.

In Chapter 3, we demonstrated that cytochromes PpcA-E show structural diversity at the heme core, in particular at the level of the heme axial ligand geometry. The comparison of the structural data obtained in solution with the available crystal structures showed significant differences. The structure determination of low-spin cytochromes in solution requires the use of paramagnetic constraints, which include the relative orientation of the heme axial ligands. Consequently, the heme axial ligand orientations determined in this work will be used to generate paramagnetic constraints to be included in the refinement of the solution structures in the oxidized state of each *Gs* triheme cytochrome.

PpcA, a member of the *Gs* triheme cytochrome c_7 family, is highly abundant in *Gs*, being most likely the reservoir of electrons destined for outer surface. Moreover, this protein can perform e^-/H^+ energy transduction, a process that is disrupted when the residue phenylalanine 15, a residue strictly conserved in the cytochrome c_7 family, is replaced by a leucine (PpcAF15L). The work described in Chapter 4 focused on the structural characterization of this PpcA mutant together with the map of the pH-dependent conformational changes. Altogether, the results obtained allowed understanding the structural origin for e^-/H^+ energy transduction mechanism in PpcA.

The detailed structural and functional characterization of PpcA sets this cytochrome as preferential target to study molecular interaction with putative redox partners. In Chapter 5, a molecular interaction between PpcA and AQDS using UV-visible and NMR spectroscopy was pinpointed. These studies showed that AH_2QDS can reduce PpcA, in agreement with their reduction potentials values. Moreover, it was shown that AH_2QDS molecules interact reversibly with the region surrounding heme IV of PpcA. This work identifies for the first time an interaction between PpcA and a putative redox partner, constituting the first step toward the rationalization of the *Gs* respiratory chain.

7. References

7. REFERENCES

1. D R Lovley, T Ueki, T Zhang, N S Malvankar, P M Shrestha, K A Flanagan, M Aklujkar, J E Butler, L Giloteaux, A E Rotaru, D E Holmes, A E Franks, R Orellana, C Risso, and K P Nevin (2011) *Geobacter*: the microbe electric's physiology, ecology, and practical applications, *Adv Microb Physiol 59*, 1-100.
2. D R Lovley, and E J Phillips (1988) Novel mode of microbial energy metabolism: organic carbon oxidation coupled to dissimilatory reduction of iron or manganese, *Appl Environ Microbiol 54*, 1472-1480.
3. D R Bond, and D R Lovley (2003) Electricity production by *Geobacter sulfurreducens* attached to electrodes, *Appl Environ Microbiol 69*, 1548-1555.
4. K P Nevin, B C Kim, R H Glaven, J P Johnson, T L Woodard, B A Methe, R J Didonato, S F Covalla, A E Franks, A Liu, and D R Lovley (2009) Anode biofilm transcriptomics reveals outer surface components essential for high density current production in *Geobacter sulfurreducens* fuel cells, *PLoS One 4*, e5628.
5. M Izallalen, R Mahadevan, A Burgard, B Postier, R Didonato, J Sun, C H Schilling, and D R Lovley (2008) *Geobacter sulfurreducens* strain engineered for increased rates of respiration, *Metabolic Engineering 10*, 267-275.
6. M V Coppi, C Leang, S J Sandler, and D R Lovley (2001) Development of a genetic system for *Geobacter sulfurreducens*, *Appl Environ Microbiol 67*, 3180-3187.
7. B A Methe, J Webster, K Nevin, J Butler, and D R Lovley (2005) DNA microarray analysis of nitrogen fixation and Fe(III) reduction in *Geobacter sulfurreducens*, *Appl Environ Microbiol 71*, 2530-2538.
8. B A Methe, K E Nelson, J A Eisen, I T Paulsen, W Nelson, J F Heidelberg, D Wu, M Wu, N Ward, M J Beanan, R J Dodson, R Madupu, L M Brinkac, S C Daugherty, R T DeBoy, A S Durkin, M Gwinn, J F Kolonay, S A Sullivan, D H Haft, J Selengut, T M Davidsen, N Zafar, O White, B Tran, C Romero, H A Forberger, J Weidman, H Khouri, T V Feldblyum, T R Utterback, S E Van Aken, D R Lovley, and C M Fraser (2003) Genome of *Geobacter sulfurreducens*: metal reduction in subsurface environments, *Science 302*, 1967-1969.
9. J E Butler, F Kaufmann, M V Coppi, C Nunez, and D R Lovley (2004) MacA, a diheme *c*-type cytochrome involved in Fe(III) reduction by *Geobacter sulfurreducens*, *J Bacteriol 186*, 4042-4045.
10. J R Lloyd, C Leang, A L Hodges Myerson, M V Coppi, S Cuifo, B Methe, S J Sandler, and D R Lovley (2003) Biochemical and genetic characterization of PpcA, a periplasmic *c*-type cytochrome in *Geobacter sulfurreducens*, *Biochem J 369*, 153-161.
11. T Mehta, M V Coppi, S E Childers, and D R Lovley (2005) Outer membrane *c*-type cytochromes required for Fe(III) and Mn(IV) oxide reduction in *Geobacter sulfurreducens*, *Appl Environ Microbiol 71*, 8634-8641.
12. C Leang, M V Coppi, and D R Lovley (2003) OmcB, a *c*-type polyheme cytochrome, involved in Fe(III) reduction in *Geobacter sulfurreducens*, *J Bacteriol 185*, 2096-2103.
13. K P Nevin, and D R Lovley (2002) Mechanisms for accessing insoluble Fe(III) oxide during dissimilatory Fe(III) reduction by *Geothrix fermentans*, *Appl Environ Microbiol 68*, 2294-2299.
14. T S Magnuson, N Isoyama, A L Hodges-Myerson, G Davidson, M J Maroney, G G Geesey, and D R Lovley (2001) Isolation, characterization and gene sequence analysis of a membrane-associated 89 kDa Fe(III) reducing cytochrome *c* from *Geobacter sulfurreducens*, *Biochemical Journal 359*, 147-152.
15. X Qian, T Mester, L Morgado, T Arakawa, M L Sharma, K Inoue, C Joseph, C A Salgueiro, M J Maroney, and D R Lovley (2011) Biochemical characterization of purified OmcS, a *c*-type cytochrome required for insoluble Fe(III) reduction in *Geobacter sulfurreducens*, *Biochim Biophys Acta 1807*, 404-412.
16. C Leang, X Qian, T Mester, and D R Lovley (2010) Alignment of the *c*-type cytochrome OmcS along pili of *Geobacter sulfurreducens*, *Appl Environ Microbiol 76*, 4080-4084.
17. J Seidel, M Hoffmann, K E Ellis, A Seidel, T Spatzal, S Gerhardt, S J Elliott, and O Einsle (2012) MacA is a second cytochrome *c* peroxidase of *Geobacter sulfurreducens*, *Biochemistry 51*, 2747-2756.

18. Y H Ding, K K Hixson, M A Aklujkar, M S Lipton, R D Smith, D R Lovley, and T Mester (2008) Proteome of *Geobacter sulfurreducens* grown with Fe(III) oxide or Fe(III) citrate as the electron acceptor, *Biochim Biophys Acta 1784*, 1935-1941.

19. P R Pokkuluri, Y Y Londer, N E Duke, W C Long, and M Schiffer (2004) Family of cytochrome c_7-type proteins from *Geobacter sulfurreducens*: structure of one cytochrome c_7 at 1.45 A resolution, *Biochemistry 43*, 849-859.

20. S F Altschul, T L Madden, A A Schaffer, J Zhang, Z Zhang, W Miller, and D J Lipman (1997) Gapped BLAST and PSI-BLAST: a new generation of protein database search programs, *Nucleic Acids Res 25*, 3389-3402.

21. D R Lovley, E J Phillips, D J Lonergan, and P K Widman (1995) Fe(III) and S_0 reduction by *Pelobacter carbinolicus*, *Appl Environ Microbiol 61*, 2132-2138.

22. Q He, and R A Sanford (2003) Characterization of Fe(III) reduction by chlororespiring *Anaeromyxobacter dehalogenans*, *Appl Environ Microbiol 69*, 2712-2718.

23. M Czjzek, P Arnoux, R Haser, and W Shepard (2001) Structure of cytochrome c_7 from *Desulfuromonas acetoxidans* at 1.9 A resolution, *Acta Crystallogr D Biol Crystallogr 57*, 670-678.

24. L Morgado, M Bruix, V Orshonsky, Y Y Londer, N E Duke, X Yang, P R Pokkuluri, M Schiffer, and C A Salgueiro (2008) Structural insights into the modulation of the redox properties of two *Geobacter sulfurreducens* homologous triheme cytochromes, *Biochim Biophys Acta 1777*, 1157-1165.

25. P R Pokkuluri, Y Y Londer, X Yang, N E Duke, J Erickson, V Orshonsky, G Johnson, and M Schiffer (2010) Structural characterization of a family of cytochromes c_7 involved in Fe(III) respiration by *Geobacter sulfurreducens*, *Biochim Biophys Acta 1797*, 222-232.

26. G W Pettigrew, and G R Moore (1987) *Cytochromes, Biological Aspects*, Springer-Verlag.

27. L Morgado, V B Paixao, M Schiffer, P R Pokkuluri, M Bruix, and C A Salgueiro (2012) Revealing the structural origin of the redox-Bohr effect: the first solution structure of a cytochrome from *Geobacter sulfurreducens*, *Biochem J 441*, 179-187.

28. E S Shelobolina, M V Coppi, A A Korenevsky, L N DiDonato, S A Sullivan, H Konishi, H Xu, C Leang, J E Butler, B C Kim, and D R Lovley (2007) Importance of *c*-type cytochromes for U(VI) reduction by *Geobacter sulfurreducens*, *BMC Microbiol 7*, 16.

29. D L Turner, C A Salgueiro, T Catarino, J Legall, and A V Xavier (1996) NMR studies of cooperativity in the tetrahaem cytochrome c_3 from *Desulfovibrio vulgaris*, *Eur J Biochem 241*, 723-731.

30. L Morgado, M Bruix, M Pessanha, Y Y Londer, and C A Salgueiro (2010) Thermodynamic characterization of a triheme cytochrome family from *Geobacter sulfurreducens* reveals mechanistic and functional diversity, *Biophys J 99*, 293-301.

31. L Morgado, J M Dantas, M Bruix, Y Y Londer, and C A Salgueiro (2012) Fine Tuning of Redox Networks on Multiheme Cytochromes from Geobacter sulfurreducens Drives Physiological Electron/Proton Energy Transduction, *Bioinorg Chem Appl 2012*, 298739.

32. R Mahadevan, D R Bond, J E Butler, A Esteve-Nunez, M V Coppi, B O Palsson, C H Schilling, and D R Lovley (2006) Characterization of metabolism in the Fe(III)-reducing organism *Geobacter sulfurreducens* by constraint-based modeling, *Appl Environ Microbiol 72*, 1558-1568.

33. M Pessanha, L Morgado, R O Louro, Y Y Londer, P R Pokkuluri, M Schiffer, and C A Salgueiro (2006) Thermodynamic characterization of triheme cytochrome PpcA from *Geobacter sulfurreducens*: evidence for a role played in e^-/H^+ energy transduction, *Biochemistry 45*, 13910-13917.

34. Q Teng (2005) *Structural Biology: Practical NMR Applications*, Springer.

35. T D W Claridge (2009) *High-resolution NMR techniques in organic chemistry*, Elsevier, Amsterdam; Boston.

36. E Arslan, H Schulz, R Zufferey, P Kunzler, and L Thony-Meyer (1998) Overproduction of the *Bradyrhizobium japonicum c*-type cytochrome subunits of the *cbb*$_3$ oxidase in *Escherichia coli*, *Biochem Biophys Res Commun 251*, 744-747.

37. D S Wishart, C G Bigam, A Holm, R S Hodges, and B D Sykes (1995) ^{1}H, ^{13}C and ^{15}N random coil NMR chemical shifts of the common amino acids. I. Investigations of nearest-neighbor effects, *J Biomol NMR 5*, 67-81.

38. L Morgado, I H Saraiva, R O Louro, and C A Salgueiro (2010) Orientation of the axial ligands and magnetic properties of the hemes in the triheme ferricytochrome PpcA from *G. sulfurreducens* determined by paramagnetic NMR, *FEBS Lett 584*, 3442-3445.

39. D S Garrett, Y J Seok, A Peterkofsky, G M Clore, and A M Gronenborn (1997) Identification by NMR of the binding surface for the histidine-containing phosphocarrier protein HPr on the N-terminal domain of enzyme I of the *Escherichia coli* phosphotransferase system, *Biochemistry 36*, 4393-4398.

40. F H Schumann, H Riepl, T Maurer, W Gronwald, K P Neidig, and H R Kalbitzer (2007) Combined chemical shift changes and amino acid specific chemical shift mapping of protein-protein interactions, *J Biomol NMR 39*, 275-289.

41. G P Moss (1988) Nomenclature of tetrapyrroles. Recommendations 1986 IUPAC-IUB Joint Commission on Biochemical Nomenclature (JCBN), *Eur J Biochem 178*, 277-328.

42. L Morgado, V B Paixao, C A Salgueiro, and M Bruix (2011) Backbone, side chain and heme resonance assignments of the triheme cytochrome PpcA from *Geobacter sulfurreducens*, *Biomol NMR Assign 5*, 113-116.

43. R O Louro, I J Correia, L Brennan, I B Coutinho, A V Xavier, and D L Turner (1998) Electronic structure of low-spin ferric porphyrins: ^{13}C NMR studies of the influence of axial ligand orientation, *Journal of the American Chemical Society 120*, 13240-13247.

44. B M Fonseca, I H Saraiva, C M Paquete, C M Soares, I Pacheco, C A Salgueiro, and R O Louro (2009) The tetraheme cytochrome from *Shewanella oneidensis* MR-1 shows thermodynamic bias for functional specificity of the hemes, *J Biol Inorg Chem 14*, 375-385.

45. C A Salgueiro, D L Turner, and A V Xavier (1997) Use of paramagnetic NMR probes for structural analysis in cytochrome c_3 from *Desulfovibrio vulgaris*, *Eur J Biochem 244*, 721-734.

46. D L Turner, C A Salgueiro, P Schenkels, J LeGall, and A V Xavier (1995) Carbon-13 NMR studies of the influence of axial ligand orientation on haem electronic structure, *Biochim Biophys Acta 1246*, 24-28.

47. D L Turner, L Brennan, A C Messias, M L Teodoro, and A V Xavier (2000) Correlation of empirical magnetic susceptibility tensors and structure in low-spin haem proteins, *Eur Biophys J 29*, 104-112.

48. N V Shokhirev, and F A Walker (1998) The effect of axial ligand plane orientation on the contact and pseudocontact shifts of low-spin ferriheme proteins, *J Biol Inorg Chem 3*, 581-594.

49. E F Pettersen, T D Goddard, C C Huang, G S Couch, D M Greenblatt, E C Meng, and T E Ferrin (2004) UCSF Chimera-a visualization system for exploratory research and analysis, *J Comput Chem 25*, 1605-1612.

50. R Koradi, M Billeter, and K Wuthrich (1996) MOLMOL: a program for display and analysis of macromolecular structures, *J Mol Graph 14*, 51-55, 29-32.

51. R A Laskowski, J A Rullmannn, M W MacArthur, R Kaptein, and J M Thornton (1996) AQUA and PROCHECK-NMR: programs for checking the quality of protein structures solved by NMR, *J Biomol NMR 8*, 477-486.

52. A C Messias, D H Kastrau, H S Costa, J LeGall, D L Turner, H Santos, and A V Xavier (1998) Solution structure of *Desulfovibrio vulgaris* (Hildenborough) ferrocytochrome c_3: structural basis for functional cooperativity, *J Mol Biol 281*, 719-739.

53. M Assfalg, L Banci, I Bertini, M Bruschi, and P Turano (1998) 800 MHz ^{1}H NMR solution structure refinement of oxidized cytochrome c_7 from *Desulfuromonas acetoxidans*, *Eur J Biochem 256*, 261-270.

54. L Banci, I Bertini, K L Bren, H B Gray, P Sompornpisut, and P Turano (1995) Three-dimensional solution structure of the cyanide adduct of a Met80Ala variant of *Saccharomyces cerevisiae* iso-1-cytochrome *c*. Identification of ligand-residue interactions in the distal heme cavity, *Biochemistry 34*, 11385-11398.

55. L Brennan, D L Turner, A C Messias, M L Teodoro, J LeGall, H Santos, and A V Xavier (2000) Structural basis for the network of functional cooperativities in cytochrome c_3 from *Desulfovibrio gigas*: solution structures of the oxidised and reduced states, *J Mol Biol 298*, 61-82.

56. D L Turner (2000) Obtaining ligand geometries from paramagnetic shifts in low-spin haem proteins, *J Biol Inorg Chem 5*, 328-332.

57. I Bertini, C Luchinat, G Parigi, and F A Walker (1999) Heme methyl ^{1}H chemical shifts as structural parameters in some low-spin ferriheme proteins, *J Biol Inorg Chem 4*, 515-519.

58. J M Dantas, I H Saraiva, L Morgado, M A Silva, M Schiffer, C A Salgueiro, and R O Louro (2011) Orientation of the axial ligands and magnetic properties of the hemes in the cytochrome c_7 family from *Geobacter sulfurreducens* determined by paramagnetic NMR, *Dalton Trans 40*, 12713-12718.

59. L Morgado, M Bruix, Y Y Londer, P R Pokkuluri, M Schiffer, and C A Salgueiro (2007) Redox-linked conformational changes of a multiheme cytochrome from *Geobacter sulfurreducens*, *Biochem Biophys Res Commun 360*, 194-198.

60. C A Salgueiro, D L Turner, H Santos, J LeGall, and A V Xavier (1992) Assignment of the redox potentials to the four haems in *Desulfovibrio vulgaris* cytochrome c_3 by 2D-NMR, *FEBS Lett 314*, 155-158.

61. M Pessanha, Y Y Londer, W C Long, J Erickson, P R Pokkuluri, M Schiffer, and C A Salgueiro (2004) Redox characterization of *Geobacter sulfurreducens* cytochrome c_7: physiological relevance of the conserved residue F15 probed by site-specific mutagenesis, *Biochemistry 43*, 9909-9917.

62. P R Pokkuluri, N E Duke, S J Wood, M A Cotta, X L Li, P Biely, and M Schiffer (2011) Structure of the catalytic domain of glucuronoyl esterase Cip2 from *Hypocrea jecorina*, *Proteins 79*, 2588-2592.

63. J M Dantas, L Morgado, Y Y Londer, A P Fernandes, R O Louro, P R Pokkuluri, M Schiffer, and C A Salgueiro (2012) Pivotal role of the strictly conserved aromatic residue F15 in the cytochrome c_7 family, *J Biol Inorg Chem 17*, 11-24.

64. B Bjellqvist, B Basse, E Olsen, and J E Celis (1994) Reference points for comparisons of two-dimensional maps of proteins from different human cell types defined in a pH scale where isoelectric points correlate with polypeptide compositions, *Electrophoresis 15*, 529-539.

65. S Seeliger, R Cord-Ruwisch, and B Schink (1998) A periplasmic and extracellular *c*-type cytochrome of *Geobacter sulfurreducens* acts as a ferric iron reductase and as an electron carrier to other acceptors or to partner bacteria, *J Bacteriol 180*, 3686-3691.

66. D L Turner, L Brennan, S G Chamberlin, R O Louro, and A V Xavier (1998) Determination of solution structures of paramagnetic proteins by NMR, *Eur Biophys J 27*, 367-375.

67. P Guntert, W Braun, and K Wuthrich (1991) Efficient computation of three-dimensional protein structures in solution from nuclear magnetic resonance data using the program DIANA and the supporting programs CALIBA, HABAS and GLOMSA, *J Mol Biol 217*, 517-530.

68. S Sarma, R J DiGate, D B Goodin, C J Miller, and R D Guiles (1997) Effect of axial ligand plane reorientation on electronic and electrochemical properties observed in the A67V mutant of rat cytochrome b_5, *Biochemistry 36*, 5658-5668.

69. S Sarma, B Dangi, C Yan, R J DiGate, D L Banville, and R D Guiles (1997) Characterization of a site-directed mutant of cytochrome b_5 designed to alter axial imidazole ligand plane orientation, *Biochemistry 36*, 5645-5657.

70. P R Pokkuluri, Y Y Londer, X Yang, N E Duke, J Erickson, V Orshonsky, G Johnson, and M Schiffer (2010) Structural characterization of a family of cytochromes c_7 involved in Fe(III) respiration by *Geobacter sulfurreducens*, *Biochim Biophys Acta 1797*, 222-232.

71. M E Hernandez, and D K Newman (2001) Extracellular electron transfer, *Cell Mol Life Sci 58*, 1562-1571.

72. D R Lovley, J D Coates, E L Blunt-Harris, E J P Philips, and T L Woodard (1996) Humic substances as electron acceptors for microbial respiration, *Nature (Letters) 382*, 445-447.

73. D R Lovley, J L Fraga, J D Coates, and E L Blunt-Harris (1999) Humics as an electron donor for anaerobic respiration, *Environ Microbiol 1*, 89-98.

74. Z Struyk, and G Sposito (2001) Redox properties of standard humic acids, *Geoderma 102*, 329-346.

75. J D Coates, D J Ellis, E L Blunt-Harris, C V Gaw, E E Roden, and D R Lovley (1998) Recovery of humic-reducing bacteria from a diversity of environments, *Appl Environ Microbiol 64*, 1504-1509.

76. J D Coates, K A Cole, R Chakraborty, S M O'Connor, and L A Achenbach (2002) Diversity and ubiquity of bacteria capable of utilizing humic substances as electron donors for anaerobic respiration, *Appl Environ Microbiol 68*, 2445-2452.

77. J W Voordeckers, B C Kim, M Izallalen, and D R Lovley (2010) Role of *Geobacter sulfurreducens* outer surface *c*-type cytochromes in reduction of soil humic acid and anthraquinone-2,6-disulfonate, *Appl Environ Microbiol 76*, 2371-2375.

78. J B Shyu, D P Lies, and D K Newman (2002) Protective role of *tolC* in efflux of the electron shuttle anthraquinone-2,6-disulfonate, *J Bacteriol 184*, 1806-1810.

79. W M Clark (1960) *Oxidation-reduction potentials of organic systems*, Williams & Wilkins.

80. M Ubbink (2004) Complexes of photosynthetic redox proteins studied by NMR, *Photosynth Res 81*, 277-287.

8. Appendix

8. APPENDIX

A. SUPPLEMENTARY FIGURES

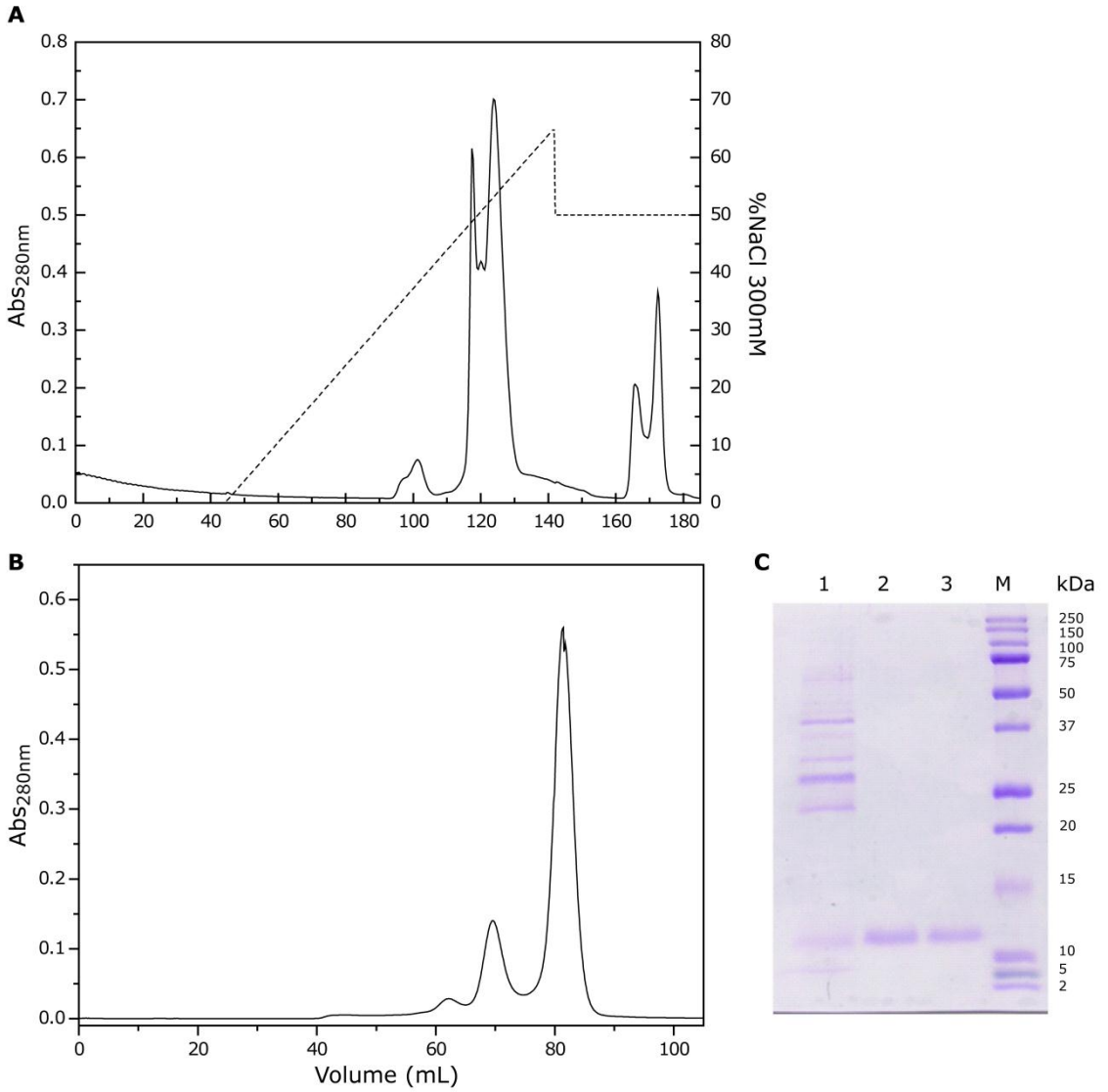

Figure A1 - Purification of unlabelled PpcAF15L. (A) Elution profile for the cation exchange column chromatography equilibrated with 10mM Tris-HCl, pH 8.5 and eluted at a flow rate of 1mL/min. Primary and second *y*-axis, report the variation of absorbance at 280 nm (solid line) and the NaCl gradient profile (dashed line), respectively. (B) Elution profile for the molecular exclusion column chromatography equilibrated with 100mM sodium phosphate buffer, pH 8. (C) Purity analysis by SDS-PAGE. Lane M: prestained protein marker; lane 1: periplasmic fraction; lane 2: after purification by cation exchange chromatography; lane 3: after purification by molecular exclusion chromatography. The MW of the protein markers are indicated on the right.

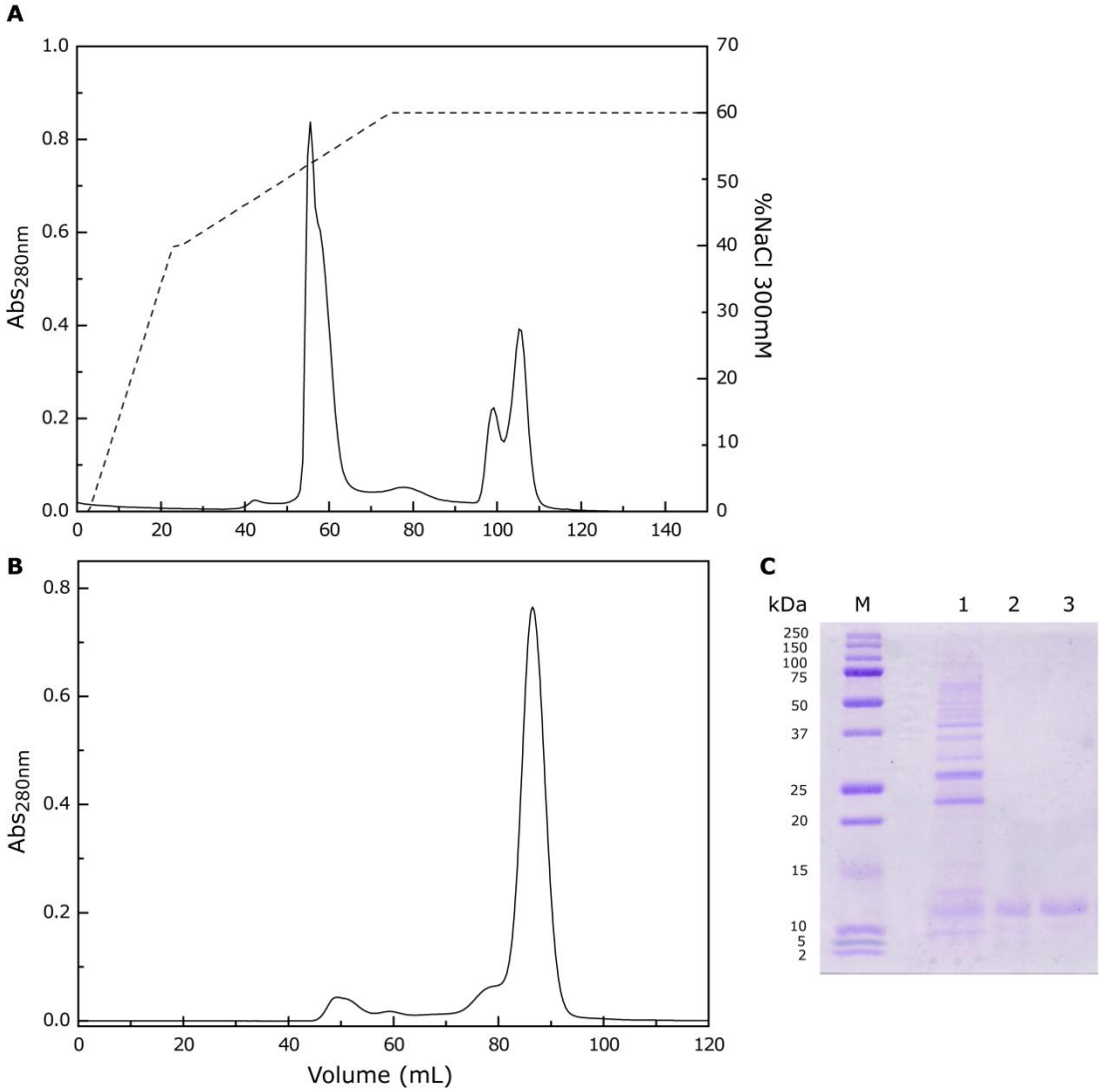

Figure A2 - Purification of unlabelled PpcA. (A) Elution profile for the cation exchange column chromatography equilibrated with 10mM Tris-HCl, pH 8.5 and eluted at a flow rate of 1mL/min. Primary and second *y*-axis, report the variation of absorbance at 280 nm (solid line) and the NaCl gradient profile (dashed line), respectively. (B) Elution profile for the molecular exclusion column chromatography equilibrated with 100mM sodium phosphate buffer, pH 8. (C) Purity analysis by SDS-PAGE. Lane M: prestained protein marker; lane 1: periplasmic fraction; lane 2: after purification by cation exchange chromatography; lane 3: after purification by molecular exclusion chromatography. The MW of the protein markers are indicated on the left.

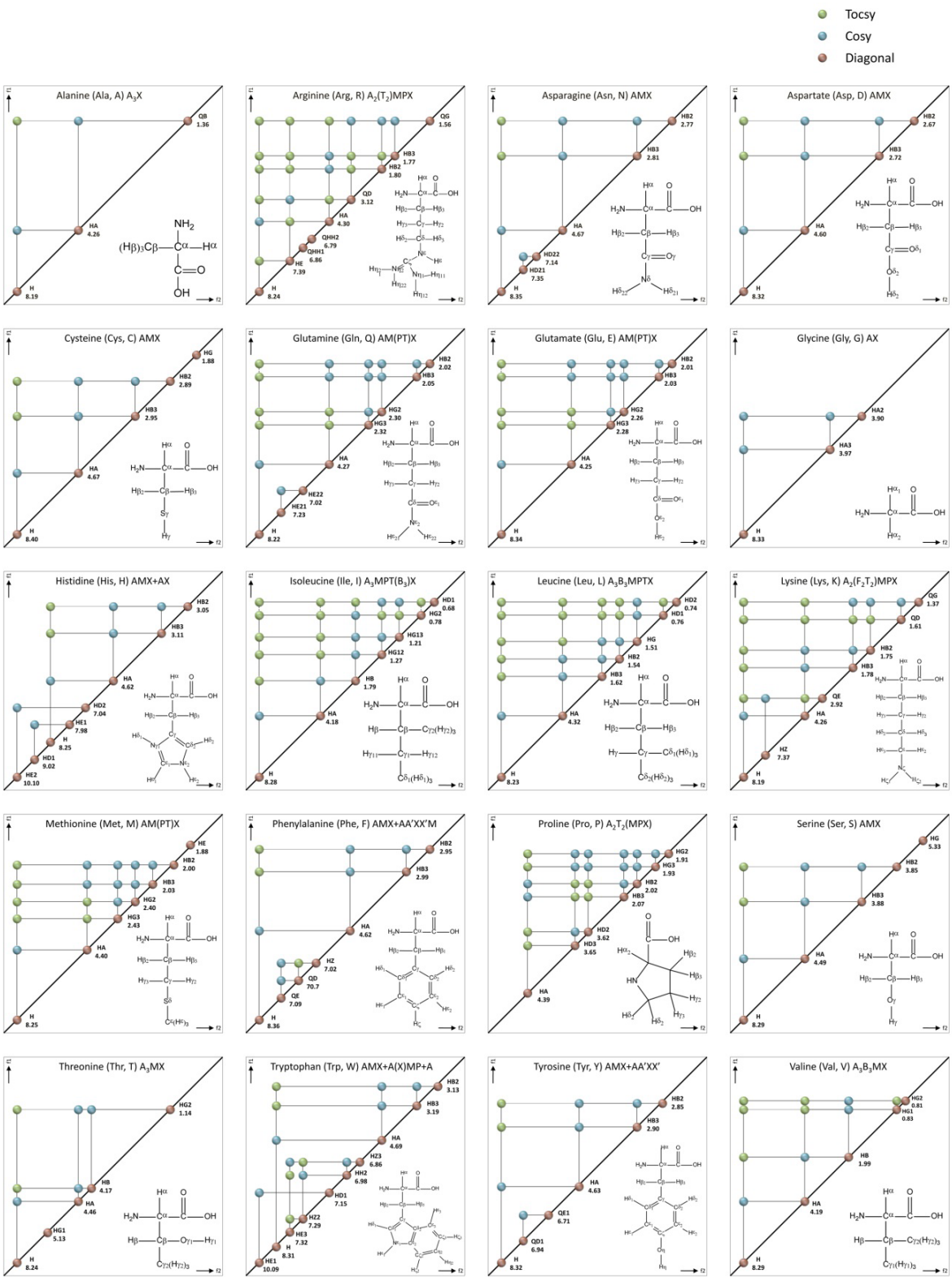

Figure A3 - 2D-^{1}H-TOCSY and 2D-^{1}H-COSY patterns of the 20 standard amino acids. The chemical shift values for the different protons are an average value calculated from the full BMRB database. The calculated statistics are derived from a total of 5129743 chemical shifts.

B. SUPPLEMENTARY TABLES

Table B1 - Chemical shifts (ppm) of the heme protons of PpcAF15L in the reduced state at pH 8 and 16ºC.

Heme substituents	Chemical shifts (ppm)		
	Heme I	**Heme III**	**Heme IV**
5H	9.49	10.63	9.03
10H	8.92	9.78	9.37
15H	9.28	9.46	9.56
20H	9.50	9.97	9.41
2^1CH_3	3.56	4.40	3.63
7^1CH_3	3.43	4.12	3.02
12^1CH_3	2.86	3.47	4.02
18^1CH_3	3.34	3.81	3.36
3^1H	6.17	7.33	6.04
8^1H	6.10	6.56	6.29
3^2CH_3	2.16	2.98	2.06
8^2CH_3	1.43	2.91	1.54

Table B2 - Chemical shifts (ppm) of the heme protons of PpcA in the reduced state at pH 8 and 16ºC [24].

Heme substituents	Chemical shift (ppm)		
	Heme I	**Heme III**	**Heme IV**
5H	9.65	10.58	9.02
10H	9.12	9.86	9.33
15H	9.26	9.45	9.51
20H	9.50	10.14	9.39
2^1CH_3	3.56	4.35	3.61
7^1CH_3	3.58	4.14	3.02
12^1CH_3	2.55	3.50	3.95
18^1CH_3	3.34	3.86	3.34
3^1H	6.30	6.91	6.04
8^1H	6.29	6.60	6.28
3^2CH_3	2.14	1.73	2.06
8^2CH_3	1.79	2.98	1.55

Table B3 - Structural assignment of the ^{1}H and ^{13}C resonances (ppm) to the PpcB-E heme α-substituents, in the oxidized form, at 16 and 25 ºC, pH 7.1. The unassigned resonances are indicated by '-'.

Protein	T (ºC)	Group	Heme I		Heme III		Heme IV	
			^{13}C	^{1}H	^{13}C	^{1}H	^{13}C	^{1}H
PpcB	16	2^1	-33.58	14.89	-26.31	13.18	-34.91	15.43
		3^1	-13.34	-0.45	-23.28	-2.41	-9.15	0.55
		7^1	-30.54	13.72	-37.27	15.91	-22.61	9.72
		8^1	-12.02	-3.89	-	-	-	-
		12^1	-45.27	17.82	-28.43	17.33	-44.29	19.58
		13^1	-17.81	1.22	-58.90	17.36	-19.44	5.13
				6.80		21.54		5.43
		17^1	-13.77	2.14	-16.86	3.96	-12.76	2.07
				-		4.28		3.14
		18^1	-40.84	17.21	-2.28	1.01	-37.01	14.15
	25	2^1	-31.96	14.55	-25.22	13.22	-33.48	15.21
		3^1	-11.22	-0.19	-21.10	-1.99	-7.83	0.79
		7^1	-29.31	13.71	-35.58	15.81	-21.49	9.63
		8^1	-10.85	-3.43	-	-	-	-
		12^1	-43.27	17.38	-27.32	17.23	-42.71	19.30
		13^1	-16.11	1.31	-55.97	16.93	-18.16	5.26
				6.66		21.32		5.57
		17^1	-12.52	2.52	-14.95	4.14	-11.65	2.30
				5.12		4.42		3.32
		18^1	-40.06	17.40	-2.25	1.59	-35.76	14.08
PpcC	16	2^1	-37.39	17.54	-24.03	11.71	-41.89	20.60
		3^1	-11.61	0.50	-21.45	-3.26	-13.41	1.79
		7^1	-22.65	10.62	-46.91	20.41	-13.14	5.69
		8^1	-9.84	-4.16	-	-	-	-
		12^1	-55.82	24.13	-21.57	11.99	-51.84	24.65
		13^1	-14.49	0.72	-	14.70	-24.43	8.85
				10.61		21.14		11.16
		17^1	-5.09	0.27	-17.81	3.37	-4.99	0.85
				3.21		5.51		2.24
		18^1	-43.58	18.63	-2.80	1.02	-29.04	10.48
	25	2^1	-35.01	16.70	-23.11	11.65	-39.98	20.12
		3^1	-8.92	0.59	-19.74	-2.89	-11.76	1.99
		7^1	-22.73	11.23	-44.94	19.94	-12.60	5.91
		8^1	-9.26	-3.67	-	-	-	-
		12^1	-52.47	22.83	-20.91	11.97	-49.62	24.11
		13^1	-12.60	0.92	-	14.45	-22.70	8.66
				9.87		20.75		11.13
		17^1	-5.30	1.11	-16.48	3.47	-4.29	1.21
				3.63		5.50		2.48
		18^1	-43.02	19.08	-2.73	1.33	-28.07	10.61

Table B3 (continued)

Protein	T (ºC)	Group	Heme I		Heme III		Heme IV	
			^{13}C	^{1}H	^{13}C	^{1}H	^{13}C	^{1}H
PpcD	16	2^1	-56.79	26.78	-21.45	10.22	-31.22	12.79
		3^1	-	-	-27.95	-2.39	-5.90	-0.60
		7^1	-2.05	3.77	-38.61	15.94	-30.85	14.64
		8^1	-34.74	-0.79	-	-	-13.63	0.07
		12^1	-54.77	21.91	-28.44	16.43	-32.70	13.32
		13^1	8.29	-2.63	-62.07	15.68	-18.73	2.33
				3.69		22.45		5.82
		17^1	5.39	0.29	-16.99	0.03	-20.76	5.19
				3.86		7.64		5.85
		18^1	-54.43	25.64	0.94	-1.20	-40.63	17.15
	25	2^1	-54.16	26.00	-20.22	10.13	-29.73	12.71
		3^1	-	-	-25.64	-2.07	-4.63	-0.31
		7^1	-1.83	3.97	-36.85	15.70	-29.24	14.37
		8^1	-32.25	-0.65	-	-	-11.72	0.36
		12^1	-52.51	21.40	-27.07	16.10	-31.44	13.37
		13^1	8.59	-2.40	-59.14	15.58	-17.32	2.70
				3.83		21.77		5.87
		17^1	5.86	0.61	-15.61	0.36	-19.13	5.32
				3.81		7.50		5.86
		18^1	-52.18	25.05	0.94	-0.78	-38.94	16.92
PpcE	16	2^1	-32.15	13.51	-27.06	13.65	-34.40	15.49
		3^1	-9.58	-0.90	-26.29	-0.46	-10.55	0.34
		7^1	-31.64	14.19	-30.91	12.47	-22.12	9.38
		8^1	-16.72	-2.87	-	-	-	-
		12^1	-38.05	14.51	-37.23	20.22	-43.17	19.06
		13^1	-10.75	-0.97	-60.31	18.16	-20.47	3.81
				5.07		19.81		6.72
		17^1	-18.08	4.09	-14.74	2.18	-14.14	2.84
				7.32		4.28		-
		18^1	-45.35	20.28	-0.83	-0.81	-36.73	14.73
	25	2^1	-30.67	13.26	-25.72	13.40	-32.79	15.15
		3^1	-7.88	-0.62	-24.14	-0.16	-9.01	0.56
		7^1	-30.35	14.07	-29.71	12.39	-21.37	9.48
		8^1	-15.25	-2.51	-	-	-	-
		12^1	-36.58	14.27	-35.94	19.86	-41.40	18.65
		13^1	-9.56	-0.77	-57.57	17.99	-19.19	3.96
				5.12		19.40		6.69
		17^1	-16.89	4.32	-13.64	2.34	-13.14	3.15
				7.36		4.37		5.04
		18^1	-43.97	20.13	-1.07	-0.26	-35.51	14.68

Table B4 - Chemical shifts (ppm) of the heme protons of PpcA in the absence and presence of AQDS (values in parenthesis) in the reduced state at pH 7.1 and 25ºC.

Heme substituents	Chemical shift (ppm)		
	Heme I	**Heme III**	**Heme IV**
2^1CH_3	3.54 (3.46)	4.33 (4.32)	3.59 (3.20)
3^1H	6.28 (6.25)	6.91 (6.89)	6.02 (5.88)
3^2CH_3	2.12 (2.08)	1.72 (1.70)	2.04 (1.90)
5H	9.63 (9.61)	10.56 (10.55)	9.00 (8.91)
7^1CH_3	3.56 (3.54)	4.13 (4.12)	3.01 (2.96)
8^1H	6.27 (6.26)	6.58 (6.57)	6.27 (6.24)
8^2CH_3	1.77 (1.77)	2.97 (2.96)	1.54 (1.51)
10H	9.11 (9.10)	9.84 (9.83)	9.32 (9.29)
12^1CH_3	2.54 (2.52)	3.49 (3.48)	3.93 (3.92)
13^1 CH_2	3.39 (3.38)	3.81 (3.80)	- (-)
	4.25 (4.23)	4.16 (4.15)	- (-)
13^2 CH_2	2.54 (2.53)	2.81 (2.80)	3.09 (3.06)
	3.10 (3.09)	2.95 (2.95)	- (-)
15H	9.25 (9.23)	9.44 (9.44)	9.44 (9.39)
17^1CH_2	3.92 (3.91)	4.14 (4.13)	4.44 (4.40)
	3.99 (3.98)	4.21 (4.21)	3.97 (3.92)
17^2CH_2	2.97 (2.96)	3.24 (3.24)	3.12 (3.08)
	3.00 (2.99)	- (-)	3.48 (3.45)
18^1CH_3	3.33 (3.29)	3.84 (3.83)	3.33 (3.18)
20H	9.48 (9.43)	10.13 (10.12)	9.37 (9.16)

Table B5 - Chemical shifts (ppm) of the heme protons of PpcA in the absence and presence of AQDS (values in parenthesis) in the oxidized state at pH 7.1 and 25ºC. The resonances not detected are indicated by '-'.

Heme substituents	**Chemical shift (ppm)**		
	Heme I	Heme III	Heme IV
2^1CH_3	17.79 (17.73)	12.15 (12.09)	14.93 (14.90)
3^1H	0.93 (0.90)	-2.54 (-2.57)	0.95 (0.92)
3^2CH_3	1.19 (1.15)	-2.21 (-2.24)	2.23 (2.09)
7^1CH_3	10.60 (10.56)	18.09 (18.06)	10.61 (10.34)
8^1H	-4.33 (-4.36)	- (-)	-0.10 (-0.19)
8^2CH_3	-4.02 (-4.04)	-0.96 (-1.00)	1.64 (1.56)
12^1CH_3	21.09 (21.14)	13.18 (13.21)	19.12 (19.15)
13^1 CH_2	2.19 (2.22)	16.21 (16.19)	4.02 (3.71)
	7.30 (7.24)	19.75 (19.76)	7.03 (6.94)
13^2 CH_2	-1.56 (-1.58)	-1.78 (-1.78)	-0.58 (-0.39)
	-0.50 (-0.52)	-1.65 (-1.68)	-0.31 (-0.12)
17^1CH_2	0.98 (0.91)	3.83 (3.79)	2.30 (2.23)
	3.01 (3.13)	5.71 (5.68)	4.06 (3.81)
17^2CH_2	-0.85(-0.88)	-2.17 (-2.21)	-0.70 (-0.73)
	-0.47 (-0.40)	-2.17 (-2.21)	-0.26 (-0.29)
18^1CH_3	15.78 (15.74)	0.79 (0.75)	14.66 (14.61)